

AD 74128

AD

**USAAMRDL TECHNICAL REPORT 72-2**

**INVESTIGATION OF THE VORTEX NOISE  
PRODUCED BY A HELICOPTER ROTOR**

**By**

**H. Kevin Johnson  
Walter M. Katz**

**February 1972**

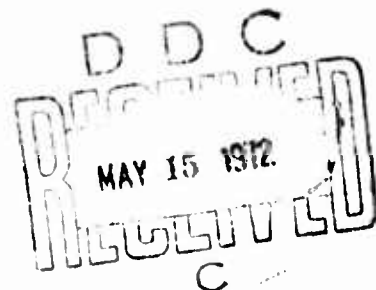
**EUSTIS DIRECTORATE  
U. S. ARMY AIR MOBILITY RESEARCH AND DEVELOPMENT LABORATORY  
FORT EUSTIS, VIRGINIA**

134

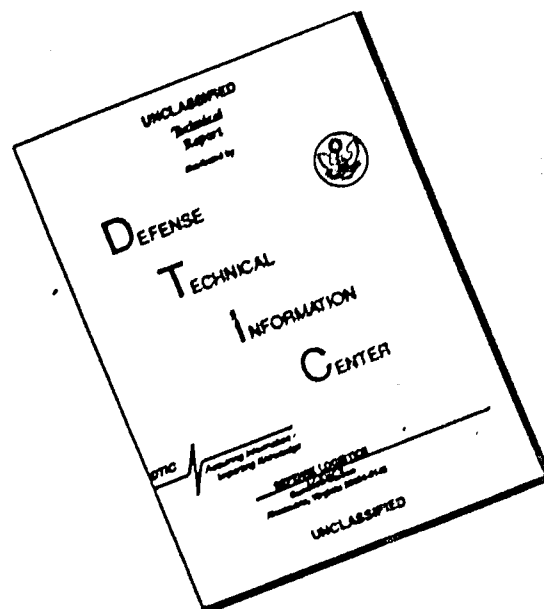
**CONTRACT DAAJ02-70-C-0023  
ROCHESTER APPLIED SCIENCE ASSOCIATES, INC.  
ROCHESTER, NEW YORK**

Reproduced by  
**NATIONAL TECHNICAL  
INFORMATION SERVICE**  
Springfield, Va 22151

**Approved for public release;  
distribution unlimited.**



# DISCLAIMER NOTICE



THIS DOCUMENT IS BEST QUALITY AVAILABLE. THE COPY FURNISHED TO DTIC CONTAINED A SIGNIFICANT NUMBER OF PAGES WHICH DO NOT REPRODUCE LEGIBLY.

### DISCLAIMERS

The findings in this report are not to be construed as an official Department of the Army position unless so designated by other authorized documents.

When Government drawings, specifications, or other data are used for any purpose other than in connection with a definitely related Government procurement operation, the United States Government thereby incurs no responsibility nor any obligation whatsoever; and the fact that the Government may have formulated, furnished, or in any way supplied the said drawings, specifications, or other data is not to be regarded by implication or otherwise as in any manner licensing the holder or any other person or corporation, or conveying any rights or permission, to manufacture, use, or sell any patented invention that may in any way be related thereto.

Trade names cited in this report do not constitute an official endorsement or approval of the use of such commercial hardware or software.

### DISPOSITION INSTRUCTIONS

Destroy this report when no longer needed. Do not return it to the originator.

ACCESSION for		
CFSTI	WHITE SECTION	<input checked="" type="checkbox"/>
DOC	BUFF SECTION	<input type="checkbox"/>
UNANNOUNCED		<input type="checkbox"/>
JUSTIFICATION		
BY		
DISTRIBUTION/AVAILABILITY CODES		
DIST.	ATL	SPECIAL
A		



Unclassified

Security Classification

DOCUMENT CONTROL DATA - R & D		
(Security classification of title, body of abstract and indexing annotation must be entered when the overall report is classified)		
1. ORIGINATING ACTIVITY (Corporate author) Rochester Applied Science Associates, Inc. 140 Allens Creek Road Rochester, New York		2a. REPORT SECURITY CLASSIFICATION Unclassified
		2b. GROUP
3. REPORT TITLE INVESTIGATION OF THE VORTEX NOISE PRODUCED BY A HELICOPTER ROTOR		
4. DESCRIPTIVE NOTES (Type of report and inclusive dates) Final Technical Report		
5. AUTHOR(S) (First name, middle initial, last name) H. Kevin Johnson Walter M. Katz		
6. REPORT DATE February 1972	7a. TOTAL NO. OF PAGES 132	7b. NO. OF REFS 18
8a. CONTRACT OR GRANT NO. DAAJ02-70-C-0023	8b. ORIGINATOR'S REPORT NUMBER(S) USAAMRDL Technical Report 72-2	
8c. PROJECT NO. Task 1F162204AA4104		
8d.	8d. OTHER REPORT NO(S) (Any other numbers that may be assigned this report) RASA REPORT 71-10	
10. DISTRIBUTION STATEMENT Approved for public release; distribution unlimited.		
11. SUPPLEMENTARY NOTES		12. SPONSORING MILITARY ACTIVITY Eustis Directorate, U. S. Army Air Mobility Research & Development Laboratory, Ft. Eustis, Virginia
13. ABSTRACT Kármán-street-type vortex shedding from a lifting surface was analyzed as a source of noise from a helicopter rotor in hover and forward flight. Experimental pressure-time histories were analyzed, and high resolution spectra were developed over a frequency range of 0 to 5000 Hz using a 0.7-Hz filter. On the basis of these spectra, the main and tail rotor rotational noise and discrete noise sources were identified and then removed from the measured pressure-time histories, leaving pressure-time histories representing only the broadband noise radiated from the rotor system. The theoretical analysis that was developed related the acoustic radiation of the vortex shedding forces on the blade to the experimental broadband pressure-time histories. This analysis was then used to solve for the oscillatory forces on the blade that would duplicate the broadband noise characteristics of measured pressure-time histories of the helicopter. The results of the investigation indicated that "vortex noise" is the major source of acoustic radiation from a helicopter rotor in hover or low-speed flight and that it is concentrated in the frequency range of 200 to 500 Hz. Because of the excellent correlation obtained between measured and predicted acoustic signatures using the mean nondimensional force constants for vortex shedding extracted from the data analysis, it is believed that the basis of a realistic method of predicting the total acoustic signature of any helicopter rotor in various flight regimes has been developed and demonstrated.		

DD FORM 1473

REPLACES DD FORM 1473, 1 JAN 64, WHICH IS OBSOLETE FOR ARMY USE.

Unclassified

Security Classification



**DEPARTMENT OF THE ARMY**  
**U. S. ARMY AIR MOBILITY RESEARCH & DEVELOPMENT LABORATORY**  
**EUSTIS DIRECTORATE**  
**FORT EUSTIS, VIRGINIA 23604**

This report has been reviewed by the Eustis Directorate, U. S. Army Air Mobility Research and Development Laboratory and is considered to be technically sound.

This program was initiated to study helicopter rotor vortex noise both analytically and experimentally. In pursuing this objective, it was necessary to make simplifying assumptions to produce a tractable problem. Some of these assumptions, particularly those related to Strouhal number, are acknowledged to represent limitations in the analysis. However, these limitations are dictated by the state of the art and should be treated as fertile areas for future research, not as errors.

Generally, this report documents the results of unique and pertinent research relative to a source of rotor noise about which little was known prior to this work. The report is published for dissemination of this data and the stimulation of ideas relative to the subject.

The program was conducted under the technical management of CPT T. D. Evans and Mr. W. E. Nettles of the Aeromechanics Division of this Directorate.

Task 1F162204AA4104  
Contract DAAJ02-70-C-0023  
USAAMRDL Technical Report 72-2  
February 1972

INVESTIGATION OF THE VORTEX NOISE  
PRODUCED BY A HELICOPTER ROTOR

Final Report

RASA Report 71-10

By

H. Kevin Johnson and Walter M. Katz

Prepared by

Rochester Applied Science Associates, Inc.  
Rochester, New York

for

EUSTIS DIRECTORATE  
U. S. ARMY AIR MOBILITY RESEARCH & DEVELOPMENT  
LABORATORY  
FORT EUSTIS, VIRGINIA

Approved for public release; distribution unlimited.
---

## ABSTRACT

Kármán-street-type vortex shedding from a lifting surface was analyzed as a source of noise from a helicopter rotor in hover and forward flight. The theoretical program that was conducted used acoustic pressure-time histories measured by NASA at the Wallops Island Test Station for a UH-1B helicopter in hover and forward flight.

The experimental pressure-time histories were analyzed and high resolution spectra were developed over a frequency range of 0 to 5000 Hz using a 0.7-Hz filter. On the basis of these spectra, the main and tail rotor rotational noise and discrete noise sources were identified and then removed from the measured pressure-time histories, leaving pressure-time histories representing only the broadband noise radiated from the rotor system. This broadband noise was then semiempirically related to the noise induced by Kármán-vortex street shedding on the rotor blade.

The theoretical analysis that was developed related the acoustic radiation of the vortex shedding forces on the blade to the pressure-time histories measured by the microphones located in the far field. This analysis was then used to solve for the oscillatory forces on the blade that would duplicate the broadband noise characteristics of measured pressure-time histories of the helicopter in various flight regimes.

The results of the investigation indicated that "vortex noise" is the major source of acoustic radiation from a helicopter rotor in hover or low-speed flight and that it is concentrated in the frequency range of 200 to 500 Hz. Because of the excellent correlation obtained between measured and predicted acoustic signatures using the averaged nondimensional force constants for vortex shedding extracted from the data analysis, it is believed that the basis of a realistic method of predicting the total acoustic signature of any helicopter rotor in various flight regimes has been developed and demonstrated.

## FOREWORD

This program was conducted by Rochester Applied Science Associates, Inc., under Contract DAAJ02-70-C-0023, Task 1F162204AA4104, and was carried out under the technical cognizance of CPT Timothy D. Evans and Mr. William E. Nettles, Eustis Directorate, U. S. Army Air Mobility Research and Development Laboratory, Fort Eustis, Virginia.

The principal investigator at RASA was Dr. H. Kevin Johnson; Dr. Walter M. Katz was responsible for the numerical analysis; Mr. Lawrence R. Sutton was involved with several phases of the program. Boeing-Vertol generated the spectra with a Ubiquitous Spectrum Analyzer.

## TABLE OF CONTENTS

	<u>Page</u>
ABSTRACT . . . . .	iii
FOREWORD . . . . .	v
LIST OF ILLUSTRATIONS . . . . .	viii
LIST OF SYMBOLS . . . . .	xiv
INTRODUCTION . . . . .	1
ANALYSIS OF EXPERIMENTAL DATA . . . . .	4
Test Program . . . . .	4
Data Analysis . . . . .	6
FILTER BANDWIDTH ANALYSIS . . . . .	12
General Discussion . . . . .	12
Analytical Representation of Bandpass Filter Characteristics . . . . .	13
Application of Filter Characteristics to Data . . . . .	14
Description of Analysis Conducted . . . . .	15
Results of the Theoretical Analysis . . . . .	16
EVALUATION OF VORTEX GENERATED NOISE . . . . .	20
General Discussion . . . . .	20
Hover Analysis . . . . .	30
GENERAL COMMENTS AND SPECIFIC CONCLUSIONS . . . . .	44
Conclusions . . . . .	47
LITERATURE CITED . . . . .	112
DISTRIBUTION . . . . .	114

<u>Figure</u>	<u>LIST OF ILLUSTRATIONS</u>	<u>Page</u>
1	Noise Spectrum by Ubiquitous Analyzer for UH-1B Helicopter in 100-ft Hover; Recorded at 200 ft to the Right . . . . .	48
2	Noise Spectrum by B & K Constant-Percent Analyzer for UH-1B Helicopter in 100-ft Hover; Recorded at 200 ft to the Right. . .	49
3	Noise Spectrum by Ubiquitous Analyzer for UH-1B Helicopter in 100-ft Hover; Recorded at 700 ft to the Right. . . . .	50
4	Relative Positions of Microphones at Wallops Island Air Station . . . . .	51
5	Tip-Path Plane Coordinates . . . . .	52
6	Oscillograph Recording of Pressure-Time History for UH-1B in 100-ft Hover; Recorded at 200 ft to the Right. . . . .	53
7	Oscillograph Recording of Pressure-Time History for UH-1B Approaching at 115 Knots Level Flight; Recorded at 200 ft to the Right . . . . .	54
8	Oscillograph Recording of Pressure-Time History for UH-1B Over Ground Zero at 115 Knots Level Flight; Recorded at 200 ft to the Right . . . . .	55
9	Noise Spectrum by Ubiquitous Analyzer for UH-1B Approaching at 115 Knots Level Flight; Recorded at 200 ft to the Right . . . . .	56
10	Noise Spectrum by Ubiquitous Analyzer for UH-1B Over Ground Zero at 115 Knots Level Flight; Recorded at 200 ft to the Right. .	57
11	Noise Spectrum by Ubiquitous Analyzer for UH-1B Moving Away at 115 Knots Level Flight; Recorded at 200 ft to the Right. .	58
12	Oscillograph Recording of Pressure-Time History for UH-1B Approaching at 115 Knots Level Flight; Recorded at 200 ft to the Right . . . . .	59

<u>Figure</u>		<u>Page</u>
13	Oscillograph Recording of Pressure-Time History for UH-1B Approaching at 115 Knots Level Flight; Recorded at 200 ft to the Right . . . . .	60
14	Oscillograph Recording of Pressure-Time History for UH-1B in 100-ft Hover; Recorded at 700 ft to the Right . . . . .	61
15	Oscillograph Recording of Pressure-Time History for UH-1B in 100-ft Hover; Recorded at 700 ft to the Left . . . . .	62
16	Change in Character of Tail Rotor Noise During 115-Knot Level Flight Approach . . .	63
17	RASA Electronically Digitized Noise Spectrum for UH-1B in Hover; Recorded at 200 ft to the Right; Data Taken 26 Seconds Into Record . . . . .	64
18	RASA Electronically Digitized Spectrum for UH-1B in 100-ft Hover; Recorded at 700 ft to the Right; Data Taken 26 Seconds Into Record . . . . .	65
19	Comparison of Oscillograph and Manually Digitized Pressure-Time Histories for UH-1B in 100 ft Hover; Recorded at 200 ft to the Right . . . . .	66
20	Comparison of Oscillograph and Electronically Digitized Pressure-Time Histories for UH-1B in 115-Knot Flyby; Recorded at 200 ft to the Right . . . . .	67
21	Filter Characteristics for Ubiquitous Analyzer . . . . .	68
22	Analytically Determined Noise Spectrum at Position 4 for UH-1B in Hover; Filter Bandwidth Is Unfiltered . . . . .	69
23	Analytically Determined Noise Spectrum at Position 4 for UH-1B in Hover; Filter Bandwidth Is Unfiltered . . . . .	70

<u>Figure</u>		<u>Page</u>
24	Analytically Determined Noise Spectrum at Position 4 for UH-1B in Hover; Filter Bandwidth Is Unfiltered . . . . .	71
25	Analytically Determined Noise Spectrum at Position 4 for UH-1B in Hover; Filter Bandwidth Is Unfiltered . . . . .	72
26	Analytically Determined Noise Spectrum at Position 4 for UH-1B in Hover; Length of Record Is Ten Blade Passages . . . . .	73
27	Analytically Determined Noise Spectrum at Position 4 for UH-1B in Hover; Length of Record Is Ten Blade Passages . . . . .	74
28	Analytically Determined Noise Spectrum at Position 4 for UH-1B in Hover; Length of Record Is Ten Blade Passages . . . . .	75
29	Analytically Determined Noise Spectrum at Position 4 for UH-1B in Hover; Length of Record Is Ten Blade Passages . . . . .	76
30	Analytically Determined Noise Spectrum at Position 4 for UH-1B in Hover; Length of Record Is Ten Blade Passages . . . . .	77
31	RASA Electronically Digitized Noise Spectrum at Position 4 for UH-1B in Hover . . . . .	78
32	Retarded Time Diagram for Hover Showing Locations of Blade Radial and Azimuthal Stations . . . . .	79
33	Projected Airfoil Dimension as a Function of Angle of Attack . . . . .	80
34	RASA Electronically Digitized Pressure-Time History at Position 4 for UH-1B in Hover . . . . .	81
35	RASA Electronically Digitized Noise Spectrum at Position 4 for UH-1B in Hover . . . . .	82

<u>Figure</u>		<u>Page</u>
36	RASA Electronically Digitized Noise Spectrum at Position 4 for UH-1B in Hover (Vortex Noise Removed) . . . . .	83
37	RASA Electronically Digitized Spectrum of Vortex Noise for UH-1B in Hover . . . . .	84
38	RASA Electronically Digitized Pressure-Time History of Rotational and Gear-Clash Noise for UH-1B in Hover . . . . .	85
39	RASA Electronically Digitized Pressure-Time History of Vortex Noise for UH-1B in Hover . . . . .	86
40	RASA Electronically Digitized Noise Spectrum at Position 4 for UH-1B in Hover (Vortex Noise Removed) . . . . .	87
41	RASA Electronically Digitized Noise Spectrum of Vortex Noise at Position 4 for UH-1B in Hover . . . . .	88
42	RASA Electronically Digitized Pressure-Time History of Vortex Noise at Position 4 for UH-1B in Hover . . . . .	89
43	RASA Electronically Digitized Pressure-Time History of Total Recorded Signal at Position 4 for UH-1B in Hover . . . . .	90
44	RASA Electronically Digitized Noise Spectrum of Rotational, Gear-Clash, and High Frequency Broadband Noise at Position 4 for UH-1B in Hover . . . . .	91
45	RASA Electronically Digitized Noise Spectrum of "Vortex" Noise at Position 4 for UH-1B in Hover . . . . .	92
46	RASA Electronically Digitized Pressure-Time History of Rotational and Discrete Noise at Position 4 for UH-1B in Hover . . . . .	93
47	RASA Electronically Digitized Pressure-Time History of Vortex Noise at Position 4 for UH-1B in Hover . . . . .	94

<u>Figure</u>		<u>Page</u>
48	RASA Electronically Digitized Pressure-Time History of Total Recorded Signal at Position 6 for UH-1B in Hover . . . . .	95
49	RASA Electronically Digitized Noise Spectrum of Rotational, Gear-Clash, and High Frequency Broadband Noise at Position 6 for UH-1B in Hover . . . . .	96
50	RASA Electronically Digitized Noise Spectrum of "Vortex" Noise at Position 6 for UH-1B in Hover . . . . .	97
51	RASA Electronically Digitized Pressure-Time History of Rotational and Gear-Clash Noise at Position 6 for UH-1B in Hover . . . . .	98
52	RASA Electronically Digitized Pressure-Time History of "Vortex" Noise at Position 6 for UH-1B in Hover . . . . .	99
53	Distribution of the Magnitude of Oscillatory Lift Over Ten Radial Stations for Four Cases . . . . .	100
54	Magnitudes of the Oscillatory Lift Forces as a Function of Radial Position for Each of the Four Cases . . . . .	101
55	Predicted Vortex Pressure-Time History at Position 4 for UH-1B in Hover . . . . .	102
56	Noise Spectrum of Predicted Vortex Pressure-Time History at Position 4 for UH-1B in Hover . . . . .	103
57	Predicted Vortex Pressure-Time History at Position 4 for UH-1B in Hover . . . . .	104
58	Noise Spectrum of Predicted Vortex Pressure-Time History at Position 4 for UH-1B in Hover . . . . .	105
59	Predicted Vortex Pressure-Time History at Position 4 for UH-1B in Hover . . . . .	106
60	Noise Spectrum of Predicted Vortex Pressure-Time History at Position 4 for UH-1B in Hover . . . . .	107

<u>Figure</u>		<u>Page</u>
61	Predicted Vortex Pressure-Time History at Position 6 for UH-1B in Hover . . . . .	108
62	Noise Spectrum of Predicted Vortex Pressure-Time History at Position 6 for UH-1B in Hover . . . . .	109
63	Period of Rotational Noise as a Function of Time at 115 Knots . . . . .	110
64	Retarded-Time Diagram of UH-1B at 115 Knots (Observer 200 ft to the Right of the Helicopter) . . . . .	111

## LIST OF SYMBOLS

$(A_D)_i$	drag geometric coefficient of $\sin (\omega_i \tau_i + \psi_i)$ for the $i^{\text{th}}$ radial station
$A_k$	Fourier coefficients of pressure-time history
$(A_L)_i$	lift geometric coefficient of $\sin (\omega_i \tau_i + \psi_i)$ for the $i^{\text{th}}$ radial station
$a_n$	polynomial coefficient describing filter attenuation curve
$(B_D)_i$	drag geometric coefficient of $\cos (\omega_i \tau_i + \psi_i)$ for the $i^{\text{th}}$ radial station
$B_k$	Fourier coefficients of pressure-time history
$(B_L)_i$	lift geometric coefficient of $\cos (\omega_i \tau_i + \psi_i)$ for the $i^{\text{th}}$ radial station
BW	bandwidth of filter
BWP	bandwidth of a constant percentage filter
b	0,1
$C_i$	chord of airfoil at the $i^{\text{th}}$ radial station (ft)
$C_{l\alpha}$	slope of section lift versus angle of attack = 5.73 for NACA 0012
c	speed of sound = 1100 (ft/sec)
$(D_v)_{ij}(t)$	oscillatory drag at the $i^{\text{th}}$ radial and $j^{\text{th}}$ azimuthal due to vortex shedding (lb)
d	projected dimension of airfoil perpendicular to flow velocity (ft)
$\underline{d}$	distance of source from microphone (ft)
e	distance from flapping hinge to axis of rotation (ft)

$\hat{e}_x, \hat{e}_y, \hat{e}_z$	unit vector along local coordinates $x, y, z$
$\vec{F}_{ij}$	the total force on the $i^{\text{th}}$ radial and $j^{\text{th}}$ azimuthal station due to the lift and drag oscillatory forces (lb)
$\dot{\vec{F}}_{ij} = \frac{d}{dt} (\vec{F}_{ij})$	(lb/sec)
$f$	frequency, either cancelled or reinforced
$\vec{f}_{Di}$	unit vector is the direction of drag
$\dot{\vec{f}}_{Di} = \frac{d}{dt} (\vec{f}_d)_i$	(sec <sup>-1</sup> )
$f_L$	frequency (Doppler shifted) heard by listener
$\vec{f}_{Li}$	unit vector in the direction of lift
$\dot{\vec{f}}_{Li} = \frac{d}{dt} (\vec{f}_L)_i$	(sec <sup>-1</sup> )
$f_s$	frequency of sound source
$h$	distance between rows of vortices after they become parallel
$\underline{h}$	height of source
$i$	non-negative integer denoting radial station location
$j$	non-negative integer denoting azimuthal station location
$K_i$	contribution of the oscillatory lift and drag from the $i^{\text{th}}$ radial station to the measured pressure (lb/ft <sup>2</sup> )
$(K_c)_i$	total coefficient of $\cos(\omega_i \tau_i + \psi_i)$ for both lift and drag (lb/ft <sup>2</sup> )
$(K_s)_i$	total coefficient of $\sin(\omega_i \tau_i + \psi_i)$ for both lift and drag (lb/ft )

$(K_{Dv})_{ij}$	nondimensional magnitude of the oscillatory drag due to vortex shedding at station $i,j$
$(K_{Lv})_{ij}$	nondimensional magnitude of the oscillatory lift due to vortex shedding at station $i,j$
$(L_v)_{ij}(t)$	oscillatory lift at the $i^{\text{th}}$ radial and $j^{\text{th}}$ azimuthal station due to vortex shedding (lb)
$l$	height of microphone (ft)
$\vec{M}_{ij}$	velocity of the $i^{\text{th}}$ radial and $j^{\text{th}}$ azimuthal station divided by $c$
$\dot{\vec{M}}_{ij} = \frac{d}{dt} \vec{M}_{ij}$	( $\text{sec}^{-1}$ )
$M_{Rij}$	component of $\vec{M}_{ij}$ pointing in the direction of the observer
$\dot{M}_{Rij} = \frac{d}{dt} M_{Rij}$	( $\text{sec}^{-1}$ )
$N$	total number of frequencies $\omega_k$ , obtained from a digitized record
$N_b$	number of blades (=2)
$n$	non-negative integer
$P(t)$	the acoustic pressure measured at time $t$
$P(\vec{X}_0, t)$	the acoustic pressure measured at the time $t$ and at the observer location $\vec{X}_0$ (lb/ft <sup>2</sup> )
$P_f$	percentage factor of filter attenuation curve
$R_{ij}$	distance between observer and the $i^{\text{th}}$ radial and $j^{\text{th}}$ azimuthal station (ft)
$r_i$	radial position of the $i^{\text{th}}$ station from the axis of rotation (ft)
$r_T$	main rotor tip radius = 22 ft

SPL	sound pressure level (db relation to 0.0002 dyne/cm <sup>2</sup> )
$S_t$	Strouhal number
$S'_t$	Roshko's "universal Strouhal number" = 0.17
t	time (sec)
$t'$	retarded time (sec)
$t'_k$	$k^{\text{th}}$ iterated value of the retarded time (sec)
U	total flow velocity (ft/sec)
$U_b$	flow velocity just outside the boundary layer at the separation point (ft/sec)
$U_{ij}$	total flow velocity at station i,j (ft/sec)
$(U_p)_{ij}$	flow velocity parallel to the blade element direction of motion (ft/sec)
$(U_T)_{ij}$	flow velocity transverse to the blade element direction of motion (ft/sec)
$\dot{U}_{ij} = \frac{d}{dt} U_{ij}$	(ft/sec <sup>2</sup> )
$(\vec{V}_D)_{ij}$	flow velocity due to the dynamic response of the blade (ft/sec)
$\vec{V}_H$	velocity of the helicopter (ft/sec)
$(V_I)_i$	inflow velocity at the $i^{\text{th}}$ radial station (ft/sec)
$\vec{V}_{ij}$	velocity of the $i^{\text{th}}$ radial and $j^{\text{th}}$ azimuthal station (ft/sec)
$V_s$	velocity of sound source toward listener (ft/sec)
$\vec{V}_{ij}$	velocity of the $i^{\text{th}}$ radial and $j^{\text{th}}$ azimuthal station in the local coordinate system (ft/sec)
$\vec{X}_H$	location of helicopter in the ground coordinate system (ft)

$\vec{x}_{ij}$	location of the radial and azimuthal station in the ground coordinate system (ft)
$\vec{x}_0$	location of the observer in the ground coordinate system (ft)
$\vec{x}_{ij}$	location of the radial and azimuthal station in the local coordinate system (ft)
$X, Y, Z$	Cartesian coordinates in the ground system
$x, y, z$	local Cartesian coordinate system on helicopter
$\alpha$	angle of attack (rad)
$\alpha_i$	angle of attack at $i^{\text{th}}$ radial station (rad)
$\alpha_T$	rotor angle of attack (positive for forward tilt of tip-path plane) (rad)
$\beta_0$	coning angle relative to tip-path plane (rad)
$\beta_{Ti}$	twist angle of blade at the $i^{\text{th}}$ radial station (rad)
$\Delta$	additional distance traveled by a reflected wave
$\Delta FB$	$\omega - \omega_c / BW$
$\Delta r_i$	spanwise length of station $i$ (ft)
$\theta_0$	value of collective angle (rad)
$\Lambda, \Lambda_d, \Lambda_U$	constants associated with Strouhal-type vortex shedding
$\pi$	$PI = 3.1415927 \dots$
$\rho$	density of air = $0.002378 \text{ (lb-sec}^2/\text{ft}^4)$
$\tau_i$	retarded time of the $i^{\text{th}}$ station (sec)
$T$	time delay of reflected wave
$\phi_{ij}$	angle between total flow and the tip-path plane at the $i^{\text{th}}$ radial and $j^{\text{th}}$ azimuthal station (rad)
$\dot{\phi}_{ij} = \frac{d}{dt} \phi$	(rad/sec <sup>-1</sup> )

$\psi_{ij}$	phase of vortex shedding at the $i^{\text{th}}$ radial station and the $j^{\text{th}}$ azimuthal station
$\psi_j$	blade azimuthal angle, measured from negative x-axis in direction of rotation around tip-path plane to the $j^{\text{th}}$ azimuthal station
$\Omega$	rotational speed of rotor (rad/sec)
$\omega$	vortex shedding frequency (Hz)
$\omega_c$	center frequency of filter
$\omega'_i$	frequency of Strouhal shedding from the $i^{\text{th}}$ radial station which is seen by the observer (rad/sec)
$\omega_{ij}$	frequency of vortex shedding at the $i^{\text{th}}$ radial station and $j^{\text{th}}$ azimuthal station (rad/sec)

## INTRODUCTION

The primary contributor to the external sound of modern gas-turbine powered helicopters is the aerodynamically induced noise from the rotor system. Noise measurements have shown that the acoustic pressure-time history at an observer's location is due almost entirely to the noise output of main and tail rotor systems. This means that the helicopter's detectability, and to a large extent its effectiveness as a weapons system, is determined by the noise signature of its rotor system. In addition, because of the strong emphasis today in noise pollution control, there has been interest in rotor noise with regard to commercial helicopter operations. For these reasons, aerodynamically induced sound from rotor systems has been extensively investigated, particularly in the last 5 years. (See References 1, 2, 3, 4, and 5.)

Rotor noise consists of two basic types of sound signatures: one is repetitive in frequency; the other is broadband or nonrepetitive. The repetitive noise is typically called "rotational" noise in which the frequencies are integral multiples of the rotor-blade passage frequency. The broadband or nonrepetitive noise can be generally classified as "vortex" noise. In addition, there are other helicopter noise classifications such as "blade slap", and sources such as engine and transmission noise. These other noises and sources are not treated explicitly in this report. (See Reference 5 for a discussion of rotor noise sources.)

A standard method by which to reduce acoustic data for analysis is to generate plots of the noise spectra. These represent the acoustic energy distribution as a function of frequency. It is well-known that spectra generated from the same data by different sound-analyzing devices can vary significantly. This is partly due to the fact that the spectra are dependent upon the length of record sampled and the effective filter bandwidth of the device. In addition, the length of record selected establishes a lower bound on the bandwidth resolution that can be obtained. This bound is independent of the bandwidth of the analyzing device.

An example of the variation in spectra generated from the same data is shown in Figures 1 and 2. Shown are spectra developed using a Ubiquitous Analyzer (bandwidth = 2 Hz; length of record = 0.5 sec) and a Bruel & Kjaer Analyzer with constant percentage bandwidth (bandwidth = 6%). One section of this report will explore these differences. It is believed that a study of the effects of filter bandwidth and the length of record on the noise spectra is important for proper analysis of helicopter noise by this means.

Rotational noise is typically regarded as dominant for rotor systems (see Lawson, Reference 5). For this reason, many investigators have concentrated in this area of acoustic research. Results have shown that whereas rotational noise is dominant in most cases for frequencies below 100 Hz, above 100 Hz, rotational noise may dominate, but in most cases broadband noise will mask out the rotational noise. It has been found, however, that the dominant noise is dependent upon the location of the noise source relative to the observer. For example, refer to Figures 1 and 3. These spectra were created from the same data source and illustrate the change in contribution of the various sources of noise to the acoustic signature with change in observer orientation and distance. The noise data were taken for a UH-1B helicopter hovering at 100 feet altitude. Figure 3 shows that rotational noise is dominant. This is the spectrum developed from data received at a position 700 feet to the right side of the helicopter. In contrast, Figure 1 shows broadband noise to be dominant. This data was taken at a position 200 feet to the right of the same helicopter.

Since in general, broadband noise will be nonperiodic with respect to blade passage frequency, such noise is often classified as nonrotational. The broadband noise that is associated with helicopter rotor blades can be related to vortex shedding that occurs along the blade. For the purposes of this study, this definition will be accepted and used in the ensuing analysis. Since vortex-generated noise is believed to occur in the frequency range closer to that of maximum human ear sensitivity, the subjective loudness of such noise can be greater than that of low frequency rotor rotational noise, even though the latter may be of higher absolute magnitude.

Little is known about vortex street shedding from lifting surfaces. Vortex shedding noise from rotating cylindrical bodies was first measured by Stowell and Deming (6). Later Yudin (7) and Blokhintsev (8) developed theories predicting such noise. Hubbard (9) has reported overall noise levels due to all sources on propeller blades, and has given an estimate of noise due to vortex shedding. He found for propellers that the rotational and vortex components can be of the same order of magnitude. He noted that the vortex component has a higher frequency content than the rotational component and increases in intensity with increasing tip speed. Schlegel, et al (3) have made further refinements in Hubbard's vortex noise magnitude formula. Krzywoblocki (10) has measured the vortex shedding frequency for airfoils at low Reynolds numbers; however, the data for angles of attack below stall had wide scatter. Roshko (11) measured the frequency of shedding from circular cylinders in high Reynolds number flow, but not for airfoil-type sections.

To summarize the experimental work to date, measurements have been made of the frequency of vortex shedding, but not within the range of flow conditions encountered by helicopter rotor blades. To date, no measurements of the oscillatory lift and drag forces due to vortex shedding have been made within any range of flow conditions. It is therefore necessary that the basic characteristics of vortex shedding from airfoils be documented in order to develop a better understanding of their effects on rotor noise. Empirical or semiempirical constants will therefore have to be used to investigate the relative importance of vortex shedding on the noise characteristics of helicopter rotors until suitable measurements are obtained.

Sadler and Loewy (2) have determined, by semiempirical means, overall constants for the lift and drag forces associated with discrete vortex shedding. In this case the constants were assumed to be independent of Mach number, angle of attack, blade radius, and azimuth. However, these force constants may not be entirely independent of the aforementioned parameters.

The program reported on herein was set up so that the lift and drag force constants might be developed from experimental data. For the mathematical model, the helicopter rotor blade was represented acoustically by a series of dipoles whose strength and frequency varied radially in the case of hover, or both radially and azimuthally in the case of forward flight. If the local angle of attack and Mach number are known at a blade element, then based upon Strouhal number, the frequency of vortex shedding could be precalculated. Since there is a known relationship between dipole strength at a given point in space and acoustic pressure at another point, it was possible in this program to use experimental pressure-time histories measured at a fixed observer's location to determine the vortex constants that produced the nonharmonic (broadband) characteristics of the measured signature.

Therefore, the twofold purpose of the program discussed herein was to: (1) use measured noise pressure-time histories in conjunction with theoretical analyses to determine the effect of bandpass filter characteristics of plots of sound pressure level versus frequency; and (2) determine the characteristics of the vortex shedding forces on a helicopter rotor blade in hover and forward flight.

## ANALYSIS OF EXPERIMENTAL DATA

### TEST PROGRAM

The data used in the analysis were generated during controlled acoustic tests of a UH-1B helicopter conducted during November 1969 at Wallops Island, Virginia (12). While these data have been discussed by Evans and Nettles (12), the pertinent aspects of these tests will be reviewed here.

Prior to development of this program, suitably well-controlled acoustic data for helicopters did not exist. It was therefore recommended that the Army conduct these tests with special reference to certain requirements regarding documentation of test conditions and flight parameters.

The noise tests were conducted by the Army at the Wallops Island Air Station with cooperation of the Dynamic Loads Division of the NASA/Langley Research Center. The test area consisted of an array of microphones in the form of a cross. This is shown in Figure 4. As shown, the positive X-axis is in the direction of flight and microphones 1, 2, and 3 are at  $X = 200, 500,$  and  $700$  feet; microphones 7, 8, and 9 are at  $X = -200, -500,$  and  $-700$  feet; microphones 4, 5, and 6 are to the right of the flight path at  $Y = -200, -500,$  and  $-700$  feet; microphones 10, 11, and 12 are to the left of the flight path at  $Y = 200, 500,$  and  $700$  feet; and microphone 13 is at  $X = Y = 0$ . A local coordinate system centered at the main rotor hub moves with the helicopter and is shown in Figure 5. A variety of test conditions were covered during the test program, including low, medium and high-speed forward flight and two hover flight conditions (6 feet and 100 feet); see Table I.

Measured noise signatures were recorded on a seven-channel 1/2-inch tape along with proper calibration information. The system response was flat from 20 to 5000 Hz. Noise signatures were also graphically recorded on an oscillograph. The helicopter position was determined using radar and graphical display with time codes in order to relate to the acoustic signal. However, this means of positioning did not meet the requirements of the analysis to determine the characteristics of vortex shedding, as will be discussed later. Instead, the measured acoustic data by itself could be used to obtain the more accurate positioning of the aircraft as required by the analysis procedures.

Other shortcomings of the test data for purposes of the program are as follows: helicopter rotor rotational speed was not monitored accurately, which meant that small shifts in rotor rpm had to be estimated from analysis of the data. Fuel consumption had

**TABLE I. FLIGHT CONDITIONS FOR WHICH NOISE SIGNATURES  
WERE RECORDED AT WALLOPS ISLAND**

<b>Test Number</b>	<b>Flight Velocity (kn)</b>	<b>Altitude (ft)</b>	<b>Remarks</b>
1	54	100	-
2	54	100	-
3	83	100	-
4	83	100	-
5	115	100	Lost Radar Lock-On
6	115	100	-
7	115	100	-
8	0	100	OGE Hover
9	0	100	OGE Hover
10	0	6	IGE Hover
11	0	6	IGE Hover
12	0	6	IGE Hover
13	0	6	IGE Hover

not been monitored, so it was not possible to determine the exact aircraft weight at a given instant of time. Since rotor thrust, which in turn was related to blade element angle of attack, could not be precisely determined, these values instead had to be estimated for the analysis.

Perhaps the most desired feature not provided in the data was that the UH-1B rotor system had not been instrumented so that blade azimuthal position could be determined relative to the recorded acoustic signal. This limitation in the data was overcome during the analysis phase of the program by making use of the measured rotational noise signal. The rotor system was set at several assumed positions in retarded time, and the rotational noise signature at an observer's location was calculated for each of these positions. By comparing phasing of the computed noise signatures with that measured, it was then possible to estimate true rotor blade position in retarded time.

## DATA ANALYSIS

### General Data Characteristics

Selected oscillograph records from the data taken at Wallops Island are shown in Figures 6 through 8. Presented are time histories of the pressure recorded at a given microphone location. The scales shown were established from the recorded calibration signal. A nontrivial problem in reducing the acoustic data is that of determining polarity or the direction of positive pressure. This was found by analytical means by relating a moving dipole to the measured pressure-time histories. Since the figures in this report are plotted as they were recorded, positive pressure (where positive denotes a compressive sense) is the reverse of that indicated on the plots.

Figure 6 shows the pressure-time history recorded at position 4 with the helicopter in the 100-ft hover configuration over the data cross. The large peaks that are sinusoidal in nature occur at the blade passage frequency and are associated with rotational noise. The high frequency noise superimposed on the rotational noise is assumed to be broadband or "vortex" noise. This noise is not periodic with blade passage frequency. The tail rotor rotational noise signature is largely suppressed in this trace because the plane of the tail rotor is nearly perpendicular to a line drawn from the recording microphone at position 4 to the tail rotor.

As expected, the forward flight data differ from those taken for hover, even at the same microphone position. The effect of distance and directivity is shown by comparing Figure 7, taken early in the flyby record, with Figure 8, taken when the helicopter was near ground zero of the data cross. In the first

figure, where the helicopter is at a distance, the tail rotor noise peaks are clearly evident and occur at about five times the frequency of the main rotor peak. (The ratio of tail-to-main rotor rotational speed is 5.108 to 1.) In Figure 8, where the helicopter is near the observer, tail rotor rotational noise does not show as clearly. The difference is due to the change in directivity in that when the helicopter is far away and approaching the observer, the observer is essentially in the plane of both rotors. Conversely, when the helicopter is near the microphones, the plane of the tail rotor is approximately perpendicular to a line drawn from position 4 to the tail rotor. Also, the broadband or vortex noise is not evident when the helicopter is very far away but becomes increasingly important as the helicopter approaches the microphones. (See Figures 7 and 8.) This effect is also apparent in the spectra shown in Figures 9, 10, and 11, which represent spectra for one flyby taken respectively with helicopter position 3000 ft from ground zero (approaching), at ground zero, and at 1500 ft from ground zero (moving away).

### Doppler Effect

The Doppler effect can be seen from the forward flight oscillograph traces. The change in frequency that occurs during the flyby is observed by comparing the distances on the plots (times) between tail rotor peaks. See Figures 12 and 13. The shorter distances or times are shown in Figure 12 and correspond to a higher frequency than those shown in Figure 13. The Doppler shift depends on the helicopter's velocity, direction of flight and its instantaneous position with respect to the observer. For example, assume that an observer is located at ground zero and the helicopter is approaching the observer head-on. The apparent frequency of a pure-tone sound source on the helicopter would be increased by a constant amount during the approach; then there would be a steep drop in frequency as the helicopter passed ground zero. As the helicopter moved away from the observer, the apparent frequency would be decreased by a constant amount. For the measured data, the observer (microphone) is off to one side of the flight path. Because of this, when the helicopter is in the distance the time interval between tail rotor peaks remains relatively constant, corresponding somewhat to the helicopter approaching the observer head-on case. On the other hand, as the helicopter gets nearer the observer, there is now a gradual drop in frequency from the initial increased value, rather than the steep drop as in the head-on case. This was evident from the records where it was noted that as the helicopter approached nearer, the time between tail rotor peaks increased, corresponding to a decrease in frequency with respect to the initial increased value.

The sound from the blade in an advancing position relative to an observer dominates the noise generated from the blade in all other azimuth positions. This fact makes it easier to understand certain aspects of the data that were used herein. For example, the pressures recorded from hover at microphones 6 and 12, 700 ft to the right and left of the flight path respectively, are not the same. See Figures 14 and 15. This difference is due in part to asymmetry associated with the helicopter. For example, in Figure 14, taken to the right of the helicopter, a portion of the tail rotor disk is shielded from observers to the right by the tail pylon. Observers to the left (Figure 15) are not so shielded. The net effect of this shielding is to make the pressure-time histories differ as received by observers on either side of the flight path. Other asymmetries noted in the data were caused by the helicopter not holding position and orientation. Since no time code was recorded during the hovers, the record from one microphone position could not be correlated to that of another microphone position. Also, the advancing blade as seen from position 6 passes near the wake of the tail rotor and across the tail boom, while the advancing blade as seen from position 12 passes over the nose of the helicopter through relatively undisturbed air. This effect is significant because the sound of the advancing blade dominates the noise from the blade in all other positions relative to an observer. Finally, asymmetries caused by the wind blowing across the flight path in varying direction and magnitude can distort the sound signature. For these tests, wind speed varied from 2 to 9 knots with a mean velocity of about 5 knots, and the direction changed from east to south with a mean of about 150°. In the case of the hover data, there were no records available to indicate the precise position of the helicopter.

The change in the character of the tail rotor noise with time during an approach is shown in Figure 16. Observe the splitting of the tail rotor pulses as the aircraft approaches ground zero. This splitting of the pulse has been a subject of controversy, but can be properly explained as a ground reflection effect. The earlier time that is shown in the record corresponds to the helicopter being further away. For a fixed microphone height, increasing the distance between a noise source and the observer will decrease the time delay between the original and ground reflected signal. As the helicopter approaches the observer, the reflected signal of the tail rotor becomes more and more retarded from the original signal, until two distinct signals result. This means that the earlier pulse signals shown in these records actually represent a superposition of the original and reflected signals.

### Ground Reflection Effect

The importance of ground reflection in the data is revealed by comparing spectra for different microphone-helicopter orientations; see Figures 17 and 18, which represent extended spectra at positions 4 and 6. The general characteristic of each spectrum in the broadband region reveals a series of maxima and minima separated throughout the record by equal frequency intervals. However, this frequency interval is not the same for both recording positions. The frequency interval between successive maxima or minima on the records is seen to change as the orientation between source and observer changes. For a given microphone height above the ground, the microphone receives one signal directly from the sound source and another that is reflected from the ground and then received. The frequency interval referred to between successive peaks or valleys on the SPL records is related to this time separation between original and reflected signal. Thus, the frequency spectrum received by an observer is distorted from that of the source; some frequencies will be amplified by reflection while others are suppressed.

As noted, the acoustic signature at a microphone (from a point source) is a linear combination of the directly incident sound wave and the reflected sound wave. Assuming specular reflection, the reflected sound wave is proportional to the initial acoustic signature delayed by the time needed for the sound wave to propagate the longer distance.

For a source of altitude  $h$ , a distance  $d$  from a microphone located a height  $l$  off the ground, the additional distance  $\Delta$  traveled by the reflected wave is

$$\Delta = \sqrt{(h+l)^2 + d^2} - \sqrt{(h-l)^2 + d^2} \quad (1)$$

When  $l$  is small compared to  $h$  and  $d$ ,  $\Delta$  is well approximated by the expression

$$\Delta = \frac{2lh}{\sqrt{h^2 + d^2}} \quad (2)$$

The time delay of the reflected wave is therefore

$$\tau = \frac{2lh}{c\sqrt{h^2 + d^2}} \quad (3)$$

where  $c$  is the speed of sound.

For a given distance and microphone height, when the frequency at the microphone of the reflected sound wave is shifted by 180° or multiple thereof from that of the direct sound wave, the sound waves will interfere and cancel. This accounts for the minima in the SPL plots shown. In contrast, if the phase shift between direct and reflected waves is 360° or multiple thereof, then the incoming sound signal at the microphone will be reinforced due to direct addition of the two signals. This is the explanation for the maxima on the SPL plots.

The frequencies which correspond to a 180° phase shift are

$$f = c \frac{\sqrt{h^2 + d^2}}{2dh} (n + 1/2) \quad (4)$$

where n is a non-negative integer. These frequencies cancel. For the frequencies

$$f = d \frac{\sqrt{h^2 + d^2}}{2dh} n \quad (5)$$

the direct and reflected waves are in phase and add.

This effect is dramatically demonstrated in the spectra of the helicopter in a 100 ft hover, as shown in Figures 17 and 18 for positions 4 and 6, respectively. (These positions are 200 and 700 feet to the side. Both microphones are 5.5 feet high.)

The reflected signal time lag at position 6 is less than that of position 4 because the increase in distance travelled by a reflected wave received at position 6 is less than the increase in distance travelled by a reflected wave received at position 4. That is, the increase in distance travelled by a reflected wave at position 6 is 1.48 ft, while the increase in distance travelled by a reflected wave at position 4 is 4.65 ft. Therefore, the time lag for a sound wave at position 6 is  $1.34 \times 10^{-3}$  sec (745 Hz), while the time lag for position 4 is  $4.22 \times 10^{-3}$  sec (237 Hz). The maxima or reinforced frequencies would therefore correspond to integral multiples of this frequency, and the minima or cancelled frequencies would correspond to  $(n + 1/2)f$ . The first minimum frequency at position 6 is 373 Hz, and the first and second minima at position 4 are 118 Hz and 356 Hz, respectively (see Figures 17, 18). These frequencies are consistent with the predicted minima (372.5 Hz for position 6 and 118.5 Hz and 355.5 Hz for position 4).

The first minima of positions 4 and 10, which are equidistant from the data cross, did not occur at the same frequency. This

indicated that the helicopter was not in precise position. In fact, calculations showed that the helicopter was only 179 ft from position 4 and 95 ft high, not at 200 ft and 100 ft high. With these distances substituted into the previous calculations, the calculated maxima and minima checked closely.

### Digitization

In order to perform computer analysis of the acoustic data, the pressure-time history had to be converted into digital form to be compatible with computer input format. This process, called digitization, was first performed manually on oscillograph records which had been made directly from the original FM recordings. The hover oscillograph trace was digitized graphically with an 800 Hz calibration signal as a reference. The hover record digitized in this manner was used for the filter bandwidth analysis phase of the contract. Figure 19 compares the manually digitized data with the oscillograph record.

However, while the frequency content of the manually digitized data was adequate for the filter analysis, it was inadequate for carrying out the vortex shedding analysis. The original FM recordings were then redigitized using a high-resolution electronic conversion technique specially developed by RASA for carrying out this work. By coupling a computer with special circuitry, a 1.45-second record could be digitized at an 11.3 KHz rate providing approximately 16000 data points. The resulting frequency response of the digitized data extended from about 0.7 Hz to 5650 Hz, which exceeded the range of the recording system of 20 Hz to 5000 Hz. The signal-to-noise ratio of the developed system was excellent, at better than 45 db.

To demonstrate the accuracy of this digitization, the digitized data were plotted and compared with the corresponding oscillograph records; see Figure 20. The digitized data are in excellent agreement with the oscillograph trace. In fact, if differences do exist, the electronically digitized results should be considered the more reliable for two reasons. First, the conversion was done directly off the FM carrier of the recorded signal. This technique bypasses the FM demodulator unit, which in itself introduces some distortion to the output. In addition, the electronically digitized data bypasses the frequency response of the oscillograph galvanometers, which were flat to only about 3 KC.

## FILTER BANDWIDTH ANALYSIS

### GENERAL DISCUSSION

Spectra generated from the same pressure-time history by different spectrum analyzers can vary significantly (see Figures 1 and 2). These are spectra created from the same data--the pressure-time history for a UH-1B helicopter in a 100-ft hover recorded at a distance of 200 feet. Figure 1 shows the noise spectrum generated by a Ubiquitous Analyzer with an effective filter bandwidth of 2 Hz, whereas Figure 2 presents the spectrum resulting from a Bruel & Kjaer Analyzer, which had a constant percentage bandwidth filter of 6%. For a constant percentage bandwidth filter, the bandwidth of the filter increases with frequency, which means that the high frequency end of the spectrum is effectively smeared out due to the large bandwidth. This characteristic is well illustrated in Figure 2 where no discrete peaks occur in the high frequency range, in contrast to Figure 1 where discrete peaks are observed in the high frequency range.

In addition to the effects of filter bandwidth, other parameters influence the resulting spectrum. Perhaps the most important of these is the length of record over which the spectrum is developed. Since spectra created from digital information are in effect plots of the resulting Fourier coefficients, these spectra will depend on the time interval over which the data is sampled. In fact, for a Fourier analysis in which no filter characteristics are prescribed, the effective bandwidth of the resulting spectrum is the reciprocal of the length of record. This means that a 1-second record would result in a spectrum plot limited to a 1 Hz filter; a 10-second record would yield a spectrum with effectively a 0.1 Hz filter, etc. The reciprocal value of the record length provides a lower bound on the resolution that can be obtained in the spectrum. That is, no matter how narrow the filter bandwidth, no more information can be determined from a given record than for a filter of bandwidth equal to the reciprocal of the length of record. This means that in general the resolution will be somewhat less than this optimum amount when a filter is used to develop a spectrum.

Since the electronic equipment by which the spectra are obtained is not standard, there has frequently been controversy over interpretation of SPL's obtained from similar acoustic pressure-time histories. In addition, there has been considerable discussion as to what filter bandwidth, record, length, etc., should be used to obtain fully descriptive and accurate plots of SPL versus frequency for a given sound-pressure history. To clarify these questions, an investigation was carried out

to determine the effects of these parameters. The results of this investigation will be discussed in the following paragraphs.

#### ANALYTICAL REPRESENTATION OF BANDPASS FILTER CHARACTERISTICS

The characteristics of a bandpass filter are usually represented by attenuation curves (in db) which show the attenuation levels of signals of given frequencies relative to the center frequency of the filter. A representative attenuation curve, that of the Federal Scientific Ubiquitous Analyzer used for this program, is presented in Figure 21. In order to apply the attenuation effects of a filter to a frequency spectrum, it is necessary to consider the attenuation levels in terms of their related percentage factors, i.e., percentage of signal amplitude transmitted through filter. The conversion of attenuation values to percentage values can be achieved by the expression

$$\text{percentage factor (in decimal notation)} = 10^{-\frac{(\text{attenuation})}{20}}$$

To obtain the percentage factors in a functional form, the attenuation curve can be approximated by a power series representation and substituted in the previous expression to result in

$$P_f = 10^{-\left[\sum_{n=0}^{\infty} a_n (\Delta FB)^{bn}\right]/20} \quad (6)$$

in which  $P_f$  is the percentage factor,  $a_n$  are the polynomial coefficients that define the filter curve,  $\Delta FB$  is a function of the difference between the center frequency and the frequency of concern, and  $b$  is an integer value of 1 if the filter curve is not symmetric about the center frequency and 2 if the curve is symmetric. A curve results which has values ranging from near zero at the outer analytical cutoff limits of the filter to one at the center frequency point. For a constant bandwidth-type filter, the term  $\Delta FB$  may be defined as

$$\Delta FB \equiv (\omega - \omega_c)/BW \quad (7)$$

in which  $\omega$  is the frequency of interest,  $\omega_c$  is the center frequency of the filter, and  $BW$  is the filter's bandwidth.

To carry out the analysis, a set of representative filter characteristics had to be selected. Since experimental data were available from the Ubiquitous Analyzer by which analytical results could be compared, the filter characteristics of that instrument (see Figure 21) were selected for modelling. The Ubiquitous filter is symmetric, and hence  $b = 2$  in Equation (6). The following values of  $a_n$  provided a good fit to the filter characteristics of the Ubiquitous Analyzer:

$$\begin{aligned} a_0 &= 0.0 \\ a_1 &= 9.07221 \\ a_2 &= 4.48306 \\ a_3 &= -3.28649 \\ a_4 &= 0.818003 \\ a_5 &= -0.0904785 \\ a_6 &= 0.0037009 \end{aligned}$$

#### APPLICATION OF FILTER CHARACTERISTICS TO DATA

To explore effects of filter bandwidth and record length, a typical pressure-time history recorded for the UH-1B in hover was digitized. The digitization was carried out prior to RASA's development of an electronic digitization technique, and consequently was performed manually. Each second of record was subdivided into 1600 intervals and pressure values were scaled directly from the oscillograph records. Therefore, the maximum frequency content for the digitized records was 800 Hz.

Digitized pressure-time histories were Fourier analyzed for each case in the form

$$P(t) = \sum_{k=1}^N (\Lambda_k \cos \omega_k t + B_k \sin \omega_k t) \quad (8)$$

where  $\Lambda_k$  and  $B_k$  are the Fourier coefficients for each frequency  $\omega_k$  and  $N$  is the number of frequencies  $\omega_k$  which can be obtained from a given record and depends on the number of digitized points of pressure versus time. Note that  $2N$  input points would be required to obtain  $N$  sets of  $\Lambda_k$  and  $B_k$ .

The bandpass filter spectra were obtained by application of the desired bandpass filter curve to the Fourier coefficient information at the desired frequencies. For this analysis, the Ubiquitous filter characteristics with different bandwidths

were applied. To avoid unnecessary numerical work for small contributions from frequencies sufficiently distant from the center frequency,  $\omega_c$ , an upper and lower cutoff frequency was assumed such that only frequencies in the range

$$- 2.5 BW + \omega_c \leq \omega_k \leq 2.5 BW + \omega_c \quad (9)$$

were considered to contribute for a constant bandpass filter.

For each frequency point of the calculated spectrum, the resulting pressure was obtained by summing contributions of all frequencies that passed through a set of specified filter characteristics. In the case of a constant bandwidth filter, set at the center frequency,  $\omega_c$ , the pressure due to the applicable frequencies,  $\omega_k$ , near the center frequency was found from

$$P(\omega_c, BW) = \left\{ \frac{1}{2} \left[ \sum_{\omega_k} P_f(\omega_k, \omega_c, BW) A_k \right]^2 + \frac{1}{2} \left[ \sum_{\omega_k} P_f(\omega_k, \omega_c, BW) B_k \right]^2 \right\}^{1/2} \quad (10)$$

where

$$P_f(\omega_k, \omega_c, BW) = 10^{-\left[ \left[ \sum_{n=0}^6 a_n \left( (\omega_k - \omega_c) / BW \right)^{2n} \right] / 20 \right]}$$

$\sum_{\omega_k}$  is used to specify summation of the effects of all  $\omega_k$  which are in range defined by Equation (9). The SPL for frequency,  $\omega_c$ , is obtained by

$$SPL(\omega_c, BW) = 20 \log_{10} \left\{ P(\omega_c, BW) / .0002 \right\} = 20 \log_{10} \left\{ P(\omega_c, BW) / 2 \right\} + 80 \text{db} \quad (11)$$

For calculating spectra for the case of a constant-percentage-type bandpass filter, the above expressions should be modified by replacing the term BW with BWP, where BWP is the bandwidth defined such that it is a constant percentage of the center frequency,  $\omega_c$ .

#### DESCRIPTION OF ANALYSIS CONDUCTED

Filter characteristics of the Ubiquitous Analyzer were modelled analytically with provision to treat different constant

bandwidth values as well as constant-percentage-type filters. This meant that while a variety of widths of filter would be applied, each would have the general characteristics of the Ubiquitous filter as shown in Figure 21.

Variations in effective bandwidth were studied in the following manner. A given record was selected. Chosen was the hover condition with the UH-1B at 100 ft altitude with the pressure-time history as recorded at position 4, 200 feet from the helicopter. Four variations in length of record were selected: one blade passage interval (.0926 second); two blade passage intervals (.1852 second); five blade passage intervals (.463 second); and ten blade passage intervals (.926 second). The selected procedure was to take each of the four lengths of record and develop analytical SPL plots for each record for the following conditions: (1) unfiltered; (2) 1 Hz bandwidth Ubiquitous-type filter; (3) 2 Hz bandwidth Ubiquitous-type filter; (4) 5 Hz bandwidth Ubiquitous-type filter; (5) 10 Hz bandwidth Ubiquitous-type filter; and (6) a constant-percentage (1%) Ubiquitous-type filter.

#### RESULTS OF THE THEORETICAL ANALYSIS

Representative spectra of the four record lengths analyzed and the six simulated analog filter widths are shown in Figures 22 through 30. The effect of varying the length of record is shown in Figures 22, 23, 24, and 25. Presented are spectra for one, two, five, and ten blade passages in which the spectra were obtained from the basic Fourier analyses without applying specified filter characteristics. This means that for each of these records, the effective filter bandwidth may be considered to be the reciprocal of the record length. Hence, Figure 22 represents a spectrum developed with a 10.8 Hz filter; Figure 23 represents that for a 5.4 Hz filter; Figure 24, a 2.2 Hz filter; and Figure 25, a 1.1 Hz filter. Observe the increase in resolution as record length increases corresponding to a decrease in filter bandwidth. For example, the ten blade passage record shown in Figure 25 demonstrates the discrete nature of the main and tail rotor rotational noise. Here, the bandwidth is sufficiently small to separate the first harmonic of tail rotational noise (55 Hz) with the fifth harmonic of main rotational noise (54 Hz). As record length decreases, the bandwidth increases commensurately. The spectra in Figure 24 with a record length of  $\sim .5$  sec and a bandwidth of 2.2 Hz can no longer resolve the 1 Hz separation between the first tail rotor harmonic with the fifth rotor harmonic. When the record length is  $\sim .1$  sec, the bandwidth is 10.8 Hz (see Figure 22). In this case the main rotor rotational harmonics are no longer resolved. The values of the spectrum at these harmonics are equal to the peak values of the discrete harmonic peaks in the 1-sec record shown in Figure 25. These magnitudes remain accurate because

the length of record for the spectrum in Figure 22 was chosen to be exactly one blade passage.

Introducing a simulated filter of different bandwidths into the Fourier analysis of a given length of record has the same general effect as changing the length of record. An increase in filter bandwidth corresponds to a shortening of length of record. This is shown in Figures 26, 27, 28, and 29. Shown are the spectra from a ten-blade-passage length of record (.926 second) that have been developed with 10 Hz, 5 Hz, 2 Hz and 1 Hz bandwidth filters respectively. Observe the similarity between these spectra and those of Figures 22, 23, 24, and 25 in which record length was varied. For example, compare the plot of the one-blade-passage spectrum (Fourier analysis without filter) shown in Figure 22 to that of the 10 Hz simulated filter results of Figure 26. The general features of these plots are the same. The spectrum in Figure 26 appears smoother than the spectrum in Figure 22 because the spectrum in Figure 26 had points calculated at closer frequency intervals. The structure of the two plots is about the same. Similar comparisons can be made between Figures 23, 24, and 25 and Figures 27, 28, and 29 respectively.

Figure 30 illustrates the type of spectrum obtained with a constant-percentage (1%) bandpass filter. Here, the width of the filter is a fixed percentage of the center frequency. In other words, for a 100 Hz signal the bandwidth would be 1 Hz, whereas for a 1000 Hz signal it would be 10 Hz. Figure 30 shows that excellent resolution is obtained for the low frequency end of the spectrum (below 200 Hz) and that this resolution deteriorates in the higher frequency region. In the neighborhood of 100 Hz Figure 30 exhibits the same quality of resolution obtained throughout Figure 29 where a 1-Hz filter was applied. Similarly, Figure 30 in the neighborhood of 200 Hz can be compared with Figure 28 in which a 2-Hz filter was applied, etc.

Using the RASA electronic digitization technique previously discussed, coupled with the Fast Fourier Transform, spectra of significantly better quality can be obtained; see Figure 31. The spectrum shown in Figure 31 is from a 15-second portion of the hover record; the bandwidth is .07 Hz and the frequency range is 0 to 280 Hz. The main and tail rotational noise harmonics appear to be truly discrete. The fifth harmonic of main rotor noise and the first harmonic of tail rotor noise are clearly separated. In this record, the noise spectrum above 100 Hz is dominated by broadband rather than discrete noise. This spectrum also shows a discrete peak at 72 Hz which could not be identified with main or tail rotor rotational noise, nor with known gear clash frequencies of the UH-1B as provided RASA by Bell. Interestingly, this peak was also noted in the Ubiquitous and hand-digitized spectra where

it appeared, but not as dramatically as shown by Figure 31 from the RASA digitized record. An interesting feature provided by the high resolution with RASA's digitizing and spectral analysis procedure was the appearance of asymmetry between the two main rotor blades in the spectrum. This is revealed in Figure 31 by the narrow peaks 10 db above background, at the odd harmonics of main rotor rotational speed (half harmonics of the blade passage frequency) which are 5.4, 16.2, 27 and 37.8 Hz.

Effects of filter bandwidth and record length were also considered for records taken of helicopters in forward flight. Here, the problem is complicated due to continual Doppler shift of the frequencies and change of position of the helicopter with time. For a sound source of frequency  $f_s$  moving toward an observer at velocity  $V_s$ , the apparent frequency at a listener is given by

$$f_L = \frac{f_s}{1 - V_s/c} \quad (12)$$

As an indication of the magnitude of this effect consider a helicopter approaching a listener at a velocity of 100 fps. In that case

$$f_L = \frac{f_s}{1 - 100/1100} \approx 1.1 f_s \quad (13)$$

In other words, a signal at 100 Hz would be shifted to 110 Hz, that at 1000 Hz shifted to 1100 Hz, etc.

This constant shift is complicated when the observer is off to one side of the flight path. In this case, the frequency of the sound source as received by an observer will be continually changing with time. In regard to a spectrum that might be generated over a record length where this occurs, this means that rather than narrow discrete peaks occurring, the peaks would instead be smeared and broadened. Depending upon the amount of Doppler shift, it would become increasingly difficult or impossible to differentiate discrete rotational and gear-clash noise sources.

Another problem in analyzing forward flight records is due to the change in orientation of the helicopter with time with respect to a fixed observer. It will be shown in the next section that the primary contribution to rotational noise from the rotor occurs over a very narrow azimuth interval of the rotor. This narrow azimuth interval is where the relative Mach number of the blade is the greatest with respect to an observer. If, as in the case of forward flight, the helicopter is changing orientation with respect to the observer, then the azimuth position of the blade with respect to its maximum contribution

to the noise signature is also changing. At each of these positions, it will have a different angle of attack and velocity distribution.

In summary, forward flight spectra are seen to involve a trade-off. To minimize Doppler frequency shift and changes in the helicopter's position, as short a record length as possible should be analyzed. However, as record length is reduced, the effective filter bandwidth increases. This means that if too short a forward flight record is taken, discrete noise sources such as the main and tail rotor rotational noise peaks cannot be distinguished. On the other hand, if record length is increased, Doppler shift and position effects may similarly make it difficult to distinguish discrete frequency sources. These problem areas noted for forward flight become more acute if in addition, broadband filters are used in the analysis. For forward flight, as with hover, the narrower the filter, the better the resolution to be obtained from a given record.

## EVALUATION OF VORTEX GENERATED NOISE

### GENERAL DISCUSSION

Since the shedding of Kármán-type vortices off an airfoil causes variation of lift and drag on the airfoil surfaces, the resulting oscillatory force on the airfoil will create noise. A variety of empirical techniques exist for estimating the magnitude of noise caused by shed vortices from rotating wings. (See References 2, 3 and 9.) The analysis carried out under this program determined the magnitude of these oscillatory forces from the measured pressure-time history of the recorded sound.

The RASA electronically digitized pressure-time histories were separated into broadband and discrete components using spectral analysis techniques. The broadband pressure-time history was then used in a computer program which determined the oscillatory force on the airfoil that created the measured signal. Because of the importance of the value of the Strouhal number used in the calculations and because the Strouhal number has not been accurately measured, particularly for airfoil sections, the fitting technique used to determine the oscillatory forces was also used to determine the "best" Strouhal number.

The data used in this program were only sufficient to determine the contribution of each airfoil section to the pressure-time history. The data were not sufficient to evaluate the relative contribution of both lift and drag. Since it has been estimated that the oscillatory drag forces are very small compared to the oscillatory lift forces as regards the acoustic signal, the contribution from each station was assumed to result only from the oscillatory lift.

### The Vortex Shedding Model

The vortex street phenomenon requires a separated wake caused by the viscous effects in the boundary layer. While airfoil design minimized this separation effect, it did not eliminate it. On a physical basis, the wake formed from a separated boundary layer will be influenced by the wake width at the separation point and the flow conditions. The Strouhal number which correlates the frequency of shedding for various bodies has been defined as

$$S_t = \frac{\omega d}{U} \quad (14)$$

where  $S_t$  = Strouhal number

$\omega$  = vortex street shedding frequency (Hz)

$U$  = flow velocity (ft/sec)

$d$  = projected dimension of the body perpendicular to the flow velocity (ft)

For cylinders, the Strouhal number changes with Reynolds number and is not known for airfoils or cylinders at large Reynolds number. The Strouhal number defined above is not a universal constant, but is dependent on body geometry as well as Reynolds number. For this reason, Roshko (13) defined a "universal Strouhal number",  $S'_t$ , which is not a function of body geometry:

$$S'_t = \frac{\omega h}{U_b} \quad (15)$$

where  $S'_t$  = Roshko's "universal Strouhal number", with numerical value of about 0.17

$\omega$  = vortex shedding frequency (Hz)

$U_b$  = velocity just outside the boundary layer at the separation point, and

$h$  = distance between rows of vortices after the vortex street is formed.

For thin streamlined bodies,  $U_b = U$ ; data from NACA 65(216)-222 airfoil at angles of attack of  $8.1^\circ$  and  $10.1^\circ$  where separation occurred near the maximum thickness indicates that  $U_b = 1.14U$  (see Reference 14). Therefore,  $U_b$  may be considered bounded by  $U$  and  $(1.14)U$  for the present analysis.

The wake thickness  $h$  varies as the projected dimension of the body  $d$  perpendicular to the local resultant velocity. Reference 3 used  $h = d$  while Reference 10 used  $h = (1.54)d$ . Therefore, Equations (14) and (15) may be rewritten as

$$S_t = S'_t \frac{\Lambda_U}{\Lambda_d} = S'_t \Lambda \quad (16)$$

where  $\Lambda_U$ ,  $\Lambda_d$ , and  $\Lambda$  are constants with values defined by

$$\begin{aligned} 1.00 &\leq \Lambda_U \leq 1.14 \\ 1.00 &\leq \Lambda_d \leq 1.54 \\ 0.65 &\leq \Lambda \leq 1.14 \end{aligned}$$

Since  $S'_t = 0.17$ , the Strouhal number for airfoils can be considered to vary as follows:

$$0.11 \leq S_t \leq 0.2 \quad (17)$$

This range is only approximate, but will be used as a guide until tests can determine the existence of Strouhal-type shedding from airfoils and the proper range and dependencies of the Strouhal number on the controlling parameters.

In the present analysis, the Strouhal number for airfoil vortex shedding will be allowed to vary within the range  $0.1 \leq S_t \leq 0.3$ , which exceeds the limits defined by Equation (17). The Strouhal number will be considered constant, however, along the blade for each calculation; that is, the Strouhal number will not be allowed to vary with blade velocity and/or angle of attack. It is anticipated that the Strouhal number is dependent on these parameters, but in lieu of this knowledge, the approach used is believed to be reasonable. Thus, the vortex street shedding frequency is assumed to be

$$\omega = \frac{S_t U}{d} \quad (18)$$

where  $\omega$  = vortex shedding frequency (Hz)

$U$  = resultant velocity (ft/sec)

$d$  = projected dimension of the body perpendicular to the resultant velocity (ft)

$S_t$  = Strouhal number:  $0.1 \leq S_t \leq 0.3$

Effects of vortex shedding on the two-dimensional lift and drag forces acting on the airfoil can be investigated by considering the circulation around the appropriate airfoil section. Assuming regular shedding of vortices of alternating sign, an oscillatory circulation may be considered to be superimposed upon the steady circulation. The corresponding lift and drag forces acting on the airfoil section will then oscillate about a mean value of lift and drag. The oscillatory lift and drag due to vortex shedding can therefore be formulated as

$$\begin{aligned} (L_v)_{ij}(t) &= (K_{Lv})_{ij} \left\{ \left[ \frac{1}{2} \rho U_{ij}^2 \right] C_i \Delta r_i \right\} \sin (\omega_{ij} t + \psi_{ij}) \\ (D_v)_{ij}(t) &= (K_{Dv})_{ij} \left\{ \left[ \frac{1}{2} \rho U_{ij}^2 \right] C_i \Delta r_i \right\} \sin (\omega_{ij} t + \psi_{ij}) \end{aligned} \quad (19)$$

where  $(L_v)_{ij}(t)$  = oscillatory lift at the  $i^{\text{th}}$  radial station and the  $j^{\text{th}}$  azimuthal station due to vortex shedding (1b)

$(D_v)_{ij}(t)$  = oscillatory drag at the  $i^{\text{th}}$  radial station and the  $j^{\text{th}}$  azimuthal station due to vortex shedding (1b)

$(K_{Lv})_{ij}$  = nondimensional force constant associated with oscillatory lift at the  $i^{th}$  radial station and the  $j^{th}$  azimuthal station

$(K_{Dv})_{ij}$  = nondimensional force constant associated with oscillatory drag at the  $i^{th}$  radial station and the  $j^{th}$  azimuthal station

$\rho$  = density of air at the test conditions  
 $= 0.002378 \frac{\text{lb-sec}^2}{\text{ft}^4}$

$U_{ij}$  = relative velocity with respect to the  $i^{th}$  radial station and  $j^{th}$  azimuthal station of the airfoil (ft/sec)

$C_i$  = chord length of the  $i^{th}$  radial station (ft)

$\Delta r_i$  = station width of the  $i^{th}$  radial station (ft)

$\omega_{ij}$  = frequency of vortex shedding at the  $i^{th}$  radial station and  $j^{th}$  azimuthal station (rad/sec)

$\psi_{ij}$  = phase of the vortex forces at the  $i^{th}$  radial station and the  $j^{th}$  azimuthal station (rad)

The Cartesian coordinate system is coincident with the array of microphones at which data was recorded. A right-handed coordinate system is used in which the positive X-axis is in the direction of flight, the positive Y-axis is to the left of the flight path, the Z-axis is positive upward, and the origin of coordinates is at the intersection of the microphone arrays (see Figure 4). A local coordinate system (x,y,z) with origin at the helicopter main rotor hub moves with the helicopter; see Figure 5. The positive x-axis, however, remains in the direction of horizontal flight with the z-axis positive upward.

Tip-path coordinates are used to locate a blade element in the x,y,z coordinate system. For simplicity, the hub is assumed to be parallel to the tip-path plane. Rigid blade coning is accounted for in locating a blade element, but the analysis neglects lead-lag motion and flexible blade bending in both flapwise and chordwise directions. A blade element is therefore located in x,y,z coordinates as shown in Figure 5 in which

$$\left. \begin{aligned}
x_{ij} &= -e \cos \alpha_T \cos \psi_j - (r_i - e) \cos \beta_0 \cos \alpha_T \cos \psi_j \\
&\quad + (r_i - e) \sin \beta_0 \sin \alpha_T \\
y_{ij} &= -e \sin \psi_j - (r_i - e) \cos \beta_0 \sin \psi_j \\
z_{ij} &= e \sin \alpha_T \cos \psi_j + (r_i - e) \cos \beta_0 \sin \alpha_T \cos \psi_j \\
&\quad + (r_i - e) \sin \beta_0 \cos \alpha_T
\end{aligned} \right\} \quad (20)$$

where  $r_i$  = radial distance of the  $i^{\text{th}}$  blade element from the axis of rotation (ft)  
 $\alpha_T$  = rotor angle of attack (positive for forward tilt of tip plane) (rad)  
 $\beta_0$  = coning angle relative to tip-path plane (rad)  
 $e$  = distance from flapping hinge to axis of rotation (ft)  
 $\psi_j$  = blade azimuth angle, measured from negative x-axis in direction of rotation around tip-path plane to the  $j^{\text{th}}$  azimuthal station

The location of any source point at time  $t$  is

$$\vec{X}_{ij}(t) = \vec{X}_H(t) + \vec{x}_{ij}(t) \quad (21)$$

where  $\vec{X}_H(t)$  is the hub location at time  $t$ .

The noise sources treated are those generated from helicopter rotors. It is assumed that helicopter rotor noise is produced by variable forces on the rotor blades, not fluid mass displacement by the blades nor flow turbulence. It is therefore reasonable to use dipoles to represent these blade forces (References 5 and 16). The pressure received at an observer's location from an array of moving dipoles can be cast in the following form (see Reference 5):

$$\begin{aligned}
 P(\vec{X}_0, t) = & \sum_{i,j} \left[ \frac{1}{4\pi c R_{ij}^2 (1 - M_{R_{ij}})^2} \left\{ \vec{F}_{ij} \cdot \vec{V}_{ij} \right. \right. \\
 & \left. \left. - (\vec{X}_0 - \vec{X}_{ij}) \cdot \left[ \dot{\vec{F}}_{ij} + \frac{\vec{F}_{ij}}{(1 - M_{R_{ij}})} \left( \dot{M}_{R_{ij}} + \frac{c}{R_{ij}} (1 - M_{R_{ij}}^2) \right) \right] \right\} \right]_{t'}
 \end{aligned}
 \tag{22}$$

where  $i$  = radial location of the blade element dipole  
 $j$  = azimuthal position of blade element dipole  
 $\sum$  = sum over all blade elements

$[ ]_{t'}$  = evaluation of those quantities inside the brackets are at a "retarded time"  $t'$  corresponding to a real time  $t$

$c$  = speed of sound (ft/sec)

$\vec{X}_0$  = location of the observer (ft)

$$R_{ij} = [(\vec{X}_0 - \vec{X}_{ij}) \cdot (\vec{X}_0 - \vec{X}_{ij})]^{1/2}$$

$$M_{R_{ij}} = \frac{(\vec{X}_0 - \vec{X}_{ij}) \cdot \dot{\vec{X}}_{ij}}{R_{ij}}$$

$$\dot{M}_{R_{ij}} = \frac{(\vec{X}_0 - \vec{X}_{ij}) \cdot \ddot{\vec{X}}_{ij}}{R_{ij}}$$

$$\dot{\vec{M}}_{ij} = \frac{\vec{V}_{ij}}{c}$$

$\vec{F}_{ij}$  = force on the blade at blade element (lb)

$\vec{V}_{ij} = \vec{V}_H + \vec{v}_{ij}$  (ft/sec)

$\vec{V}_H$  = velocity of the rotor hub (ft/sec)

$\vec{v}_{ij}$  = velocity of blade element i,j (ft/sec)

$$\dot{\vec{F}}_{ij} = \frac{d}{dt} (\vec{F}_{ij})$$

$$\dot{\vec{M}}_{ij} = \frac{d}{dt} (\vec{M}_{ij})$$

The quantities in Equation (22) inside the brackets should be evaluated at a retarded time prior to  $t$  since the signal was actually emitted at an earlier time due to the finite speed of sound. That is, a signal received at an observer's location that was emitted from a source at time  $t'$  required time  $\Delta t = R/c$  to reach an observer (where  $R$  is the distance from source to observer,  $c$  is the speed of sound);  $t' + \Delta t = t$ , the real time at which the signal is received by the observer.

If  $\hat{e}_x$ ,  $\hat{e}_y$ , and  $\hat{e}_z$  are unit vectors along the x, y, and z-axis as well as the X, Y, and Z-axis, then the velocity of blade element i,j is

$$\vec{v}_{ij} = (\vec{\Omega} \times \vec{x}_{ij}) - (\vec{V}_D)_{ij} \quad (23)$$

where  $\vec{x}_{ij} = x_{ij} \hat{e}_x + y_{ij} \hat{e}_y + z_{ij} \hat{e}_z$

$$\vec{\Omega} = \Omega [(\sin \alpha_T) \hat{e}_x + (\cos \alpha_T) \hat{e}_z]$$

$(\vec{V}_D)_{ij}$  = flow velocity due to dynamic response of the blade

$\Omega$  = rotor rotational speed

Similarly,

$$c\dot{\vec{M}}_{ij} = \dot{\vec{v}}_{ij} = \dot{\vec{v}}_{ij} = \vec{\Omega} \times (\vec{\Omega} \times \vec{x}_{ij}) - (\dot{\vec{V}}_D)_{ij} \quad (24)$$

since the helicopter is assumed to be in steady rectilinear flight with constant rotor RPM.

The inflow angle at blade element i,j is defined by

$$\phi_{ij} = \tan^{-1} \frac{(U_p)_{ij}}{(U_T)_{ij}} \quad (25)$$

where  $(U_T)_{ij} = \Omega r_i + V_H \cos \alpha_T \sin \psi_j$  = component of resultant flow velocity perpendicular to blade span axis and axis of rotation

$(U_p)_{ij} = (V_I)_{ij} \cos \beta_0 + V_H \sin \alpha_T \cos \beta_0 + V_H \cos \alpha_T \sin \psi_j \sin \beta_0$  = component of resultant flow velocity perpendicular to blade span axis and  $U_T$

$(V_I)_{ij}$  = induced inflow velocity at rotor blade element  $i, j$

Following the usual convention, lift is taken perpendicular to the resultant velocity  $U_{ij}$  and drag is taken parallel to the resultant velocity. Therefore, the blade element force components are defined by

$$\begin{aligned}\vec{F}_{ij} \cdot \hat{e}_x &= (F_{ij})_x = [(L_v)_{ij} \cos \phi_{ij} - (D_v)_{ij} \sin \phi_{ij}] (\cos \beta_0 \sin \alpha_T \\ &\quad + \sin \beta_0 \cos \alpha_T \cos \psi_j) \\ &\quad - [(L_v)_{ij} \sin \phi_{ij} + (D_v)_{ij} \cos \phi_{ij}] (\cos \alpha_T \sin \psi_j) \\ \vec{F}_{ij} \cdot \hat{e}_y &= (F_{ij})_y = [(L_v)_{ij} \cos \phi_{ij} - (D_v)_{ij} \sin \phi_{ij}] (\sin \beta_0 \sin \psi_j) \\ &\quad + [(L_v)_{ij} \sin \phi_{ij} + (D_v)_{ij} \cos \phi_{ij}] (\cos \psi_j) \\ \vec{F}_{ij} \cdot \hat{e}_z &= (F_{ij})_z = [(L_v)_{ij} \cos \phi_{ij} - (D_v)_{ij} \sin \phi_{ij}] (\cos \beta_0 \cos \alpha_T \\ &\quad - \sin \beta_0 \sin \alpha_T \cos \psi_j) \\ &\quad + [(L_v)_{ij} \sin \phi_{ij} + (D_v)_{ij} \cos \phi_{ij}] (\sin \alpha_T \sin \psi_j)\end{aligned}\quad (26)$$

Taking the derivatives with respect to time, Equation (26) becomes

$$\begin{aligned}
(\dot{F}_{ij})_x = & [(\dot{L}_v)_{ij} \cos \phi_{ij} - (\dot{D}_v)_{ij} \sin \phi_{ij}] (\cos \beta_0 \sin \alpha_T \\
& + \sin \beta_0 \cos \alpha_T \cos \psi_j) \\
& - [(\dot{L}_v)_{ij} \sin \phi_{ij} + (\dot{D}_v)_{ij} \cos \phi_{ij}] (\cos \alpha_T \sin \psi_j) \\
& + [- (L_v)_{ij} \sin \phi_{ij} - (D_v)_{ij} \cos \phi_{ij}] (\dot{\phi}_{ij}) (\cos \beta_0 \sin \alpha_T \\
& + \sin \beta_0 \cos \alpha_T \cos \psi_j) \\
& - [(L_v)_{ij} \cos \phi_{ij} - (D_v)_{ij} \sin \phi_{ij}] (\dot{\phi}_{ij}) (\cos \alpha_T \sin \psi_j) \\
& + [(L_v)_{ij} \cos \phi_{ij} - (D_v)_{ij} \sin \phi_{ij}] (-\Omega \sin \beta_0 \cos \alpha_T \sin \psi_j) \\
& - [(L_v)_{ij} \sin \phi_{ij} + (D_v)_{ij} \cos \phi_{ij}] (\Omega \cos \alpha_T \cos \psi_j) \\
(\dot{F}_{ij})_y = & [(\dot{L}_v)_{ij} \cos \phi_{ij} - (\dot{D}_v)_{ij} \sin \phi_{ij}] (\sin \beta_0 \sin \psi_j) \\
& + [(\dot{L}_v)_{ij} \sin \phi_{ij} + (\dot{D}_v)_{ij} \cos \phi_{ij}] (\cos \psi_j) \\
& + [- (L_v)_{ij} \sin \phi_{ij} - (D_v)_{ij} \cos \phi_{ij}] (\dot{\phi}_{ij}) (\sin \beta_0 \sin \psi_j) \\
& + [(L_v)_{ij} \cos \phi_{ij} - (D_v)_{ij} \sin \phi_{ij}] (\dot{\phi}_{ij}) (\cos \psi_j) \\
& + [(L_v)_{ij} \cos \phi_{ij} - (D_v)_{ij} \sin \phi_{ij}] (\Omega \sin \beta_0 \cos \psi_j) \\
& + [(L_v)_{ij} \sin \phi_{ij} + (D_v)_{ij} \cos \phi_{ij}] (-\Omega \sin \psi_j) \\
(\dot{F}_{ij})_z = & [(\dot{L}_v)_{ij} \cos \phi_{ij} - (\dot{D}_v)_{ij} \sin \phi_{ij}] (\cos \beta_0 \cos \alpha_T \\
& - \sin \beta_0 \sin \alpha_T \cos \psi_j) \\
& + [(\dot{L}_v)_{ij} \sin \phi_{ij} + (\dot{D}_v)_{ij} \cos \phi_{ij}] (\sin \alpha_T \sin \psi_j) \\
& + [- (L_v)_{ij} \sin \phi_{ij} - (D_v)_{ij} \cos \phi_{ij}] (\dot{\phi}_{ij}) (\cos \beta_0 \cos \alpha_T \\
& - \sin \beta_0 \sin \alpha_T \cos \psi_j) \\
& + [(L_v)_{ij} \cos \phi_{ij} - (D_v)_{ij} \sin \phi_{ij}] (\dot{\phi}_{ij}) (\sin \alpha_T \sin \psi_j) \\
& + [(L_v)_{ij} \cos \phi_{ij} - (D_v)_{ij} \sin \phi_{ij}] (\Omega \sin \beta_0 \sin \alpha_T \sin \psi_j) \\
& + [(L_v)_{ij} \sin \phi_{ij} + (D_v)_{ij} \cos \phi_{ij}] (\Omega \sin \alpha_T \cos \psi_j) \quad (27)
\end{aligned}$$

where  $(L_v)_{ij}$  and  $(D_v)_{ij}$  are defined by Equation (19).

With terms comprising Equation (22) formulated, the pressure at an observer's location may be specified once the appropriate sources have been located in retarded time. The acoustic signature of the rotor is assumed to emanate from a series of dipoles located at blade stations. The sound reaching a microphone at some instant in time,  $t$ , originates from each of these stations at some earlier time,  $t'$ . The time that the sound originated from each station (retarded time) is a function of the position of each station, and its motion and is, in general, different for each station.

To determine the retarded time of each station for a time,  $t$ , the following techniques were used. The position of a station on the blade is known as a function of time. Let  $\vec{X}_{ij}(t)$  describe the motion of this station. Let  $\vec{X}_0$  be the position of the microphone. Then a sound wave originating from this station at some retarded time  $t'$  arrives at the microphone at time  $t$ . The time lapse of the sound from inception to reception is  $t-t'$ . This delay corresponds to the time required for the sound wave (traveling at the speed of sound  $c$ ) to travel the distance

$$R = |\vec{X}_0 - \vec{X}_{ij}(t')|.$$

That is, 
$$|\vec{X}_0 - \vec{X}_{ij}(t')| = c(t - t') \quad (28)$$

Equation (28) is, in general, transcendental and is solved using an iterative technique. An initial estimate is made for  $t'$ . This estimate  $t'_0$  is used in the left side of Equation (28) which is solved for the first iterative value,  $t'_1$ .

$$t'_1 = t - |\vec{X}_0 - \vec{X}_{ij}(t'_0)|/c \quad (29)$$

This new value  $t'_1$  is then used in the right side of Equation (29), giving a second iterative value  $t'_2$  and so on until the solution converges. The retarded time calculation, therefore, locates the sources in space-time that contribute to the pressure at time  $t$ . The retarded time calculation procedure has been programmed for computer use. The program developed locates for an observer's location at time  $t$ , the contributing retarded time position of each radial blade station. The results of a typical retarded time calculation are shown in graphical form in Figure 32. The rotor disk has been broken up into 40 azimuthal sections and 10 radial sections, and the azimuthal spacing in retarded time is not equal as it would be in true time. The difference in the spacing between the advancing blade (observer on the negative y-axis) and the retreating blade is very obvious in this graphical presentation.

## HOVER ANALYSIS

For this analysis, the UH-1B helicopter was in the hover configuration 100 ft over the microphone data cross with helicopter orientation along the flight path. The data received were recorded at microphone 4, which was 200 ft to the right of the flight path.

### Determination of Angles of Attack, Resultant Velocities, Shedding Frequencies

The Strouhal shedding frequency of the UH-1B airfoil (NACA 0012) was assumed to be proportional to the flow velocity and inversely proportional to the separation thickness of the flow. This flow separation has been assumed to be equal to the projected dimension,  $d$ , of the airfoil perpendicular to the resultant velocity  $U$  (see Equations (14) through (18)). The dependence of the projected dimension as a function of angle of attack for the NACA 0012 blade is shown in Figure 33. For use in computer programs, this curve was fit in the three regions indicated in Figure 33. The functional relationships used in each of the three regions are:

<u>Region</u>	<u><math>\alpha</math> Range</u>	<u>Projected <math>d_i</math></u>
I	$0^\circ - 7.5^\circ$	$(1 + 0.00623\alpha_i^2)(0.12 C_i)$
II	$7.5^\circ - 20^\circ$	$(0.4 + 0.125\alpha_i)(.12C_i)$
III	$20^\circ - 90^\circ$	$C_i \sin(\alpha_i)$ (30)

where  $\alpha_i$  is the angle of attack in radians

$C_i$  is the chord length

For the hover cases analyzed, the blade element velocities and angles of attack were calculated using the formulations of Reference 15. The wind velocity was small and negligible compared with the blade velocity and therefore was assumed to be zero. The inflow velocity perpendicular to the blade-element direction of motion ( $V_I$ ) was

$$(V_I)_i = \left[ \frac{N_b C_i \Omega C_{\ell \alpha}}{16\pi} \right] \left\{ -1 + \left[ 1 + \frac{2\Omega r_i (\theta_0 + \beta T_i)}{\left[ \frac{N_b C_i \Omega C_{\ell \alpha}}{16\pi} \right]} \right]^{1/2} \right\} \quad (31)$$

where  $N_b$  = number of blades = 2

$C_i$  = chord of  $i^{\text{th}}$  station = 1.75 ft

$\Omega$  = main rotor rotational speed = 33.929 rad/sec

$C_{l\alpha}$  = slope of the curve of section lift coefficient  
against angle of attack = 5.73 for an NACA 0012

$\theta_0$  = blade collective pitch angle = 0.236 rad

$B_{Ti}$  = blade twist =  $-0.175 r_i/r_T$

$r_T$  = main rotor tip radius = 22 ft

The angle of attack at the  $i^{\text{th}}$  radial station for hover is defined by

$$\alpha_i = \theta_0 + B_{Ti} - \phi_i \quad (32)$$

The flow velocity components transverse and parallel to the blade-element direction of motion are respectively (see Equation (25))

$$(U_T)_i = \Omega r_i \quad \text{and}$$

$$(U_P)_i = (V_I)_i \cos \beta_0 \quad (33)$$

where the coning angle  $\beta_0 = 0.044$  radians and the rotor angle of attack  $\alpha_T = 0$  for hover.

The inflow angle  $\phi_i$  is then

$$\phi_i = \tan^{-1} \left( \frac{(V_I)_i}{\Omega r_i} \cos \beta_0 \right) \quad (34)$$

and the magnitude of the total resultant flow velocity is

$$U_i = [\Omega^2 r_i^2 + (V_I)_i^2 \cos^2 \beta_0]^{1/2} \quad (35)$$

Because the helicopter is in hover all of these quantities are assumed to have no azimuthal variations.

## Numerical Technique

Measured pressures can now be related to the oscillatory force constants. The objective is to solve for the unknown oscillatory force constants in terms of the measured pressure-time history. For the hover configuration, the values of the oscillatory forces are assumed constant about the rotor disk, since angle of attack and velocity are similarly assumed to be constant. The geometric parameters, however, change considerably with respect to an observer, so it is desirable to segment the time for each blade passage into smaller time intervals. If the time intervals are small enough, the geometric parameters are essentially constant during the interval.

If the geometric parameters can be assumed constant in a small interval of time, then the predictive equations can be linearized. When possible, such a linearization of a set of equations greatly reduces the numerical difficulties of their solution. The time interval chosen constrains the frequency range and number of oscillatory stations per blade much in the same way that length of record is related to bandwidth. The largest time interval that was felt to be consistent with maintaining constant geometric parameters within that interval was 1/200 sec. For example, if the time for one blade passage is divided into 20 equal time intervals (the blade passage frequency is 10.8 Hz), each time interval is approximately 1/200 sec. Thus, phenomena which change with frequency less than 200 Hz cannot be considered. This cutoff is a judicious compromise between frequency range and blade element station size. That is, if a smaller time interval were chosen, the area swept by the blade (the station size) would be smaller but the lower frequency cutoff would increase. Conversely, if a larger time interval were chosen the lower frequency cutoff would decrease, but the area swept by the blade would increase and tend to invalidate this discrete element analysis.

The Strouhal frequency formulation is such that the shedding frequency increases with radius. Because of the Doppler effect, the observed frequencies are increased further on the advancing blade while decreased on the retreating blade. This is coupled to the Mach number effect in Equation (22) which increases the pressure amplitude of the advancing blade stations through the terms  $1/(1-M_R)$  and decreases the pressure amplitude of the retreating blade stations ( $M_R$  is negative for a retreating blade, positive for an advancing blade).

The larger frequency spread on the advancing blade allows a larger number of blade elements with observer frequency separations above  $\sim 200$  Hz. On the retreating blade the Doppler effect works in reverse and decreases the observed frequencies. The net result is that for the observer frequencies above 500 Hz, the section of the airfoil from midspan to the tip of the advancing UH-1B blade contributes, while below 500 Hz the inboard half of the advancing blade and the whole retreating blade contribute.

### Solution Technique

In order to solve for the magnitude of the oscillatory forces on the helicopter blade several assumptions have been made:

1. The oscillatory forces on an airfoil occur at the frequencies associated with Strouhal shedding.
2. The Strouhal number is assumed to be independent of Reynolds number.
3. The oscillatory forces are sinusoidal and have components only in the lift and drag direction.
4. The oscillatory forces on the blade can be represented by oscillatory dipoles acting at the center of ten spanwise stations.
5. For each small increment of time ( $\sim 0.005$  second), the aerodynamic and geometric parameters at each of the ten spanwise regions remain essentially constant.
6. In the time intervals when one blade advances toward the observer while the opposite blade retreats, the noise at the observer for frequencies above 500 Hz is assumed to originate from the advancing blade above.

Using these assumptions, the pressure-time history at an observer for a blade in the advancing region is

$$\begin{aligned}
 P(t) = \sum_{i=1}^{10} \left\{ (K_{Lv})_i [(A_L)_i \sin(\omega_i \tau_i + \psi_i) + (B_L)_i \cos(\omega_i \tau_i + \psi_i)] \right. \\
 \left. + (K_{Dv})_i [(A_D)_i \sin(\omega_i \tau_i + \psi_i) + (B_D)_i \cos(\omega_i \tau_i + \psi_i)] \right\}
 \end{aligned}
 \tag{36}$$

where  $(K_{Lv})_i$  is the magnitude of the oscillatory lift coefficient at the  $i^{\text{th}}$  spanwise station

$(K_{Dv})_i$  is the magnitude of the oscillatory drag coefficient at the  $i^{\text{th}}$  spanwise station

$\tau_i$  is the retarded time for station  $i$

$\omega_i$  is the Strouhal shedding frequency of the  $i^{\text{th}}$  spanwise station

$\psi_i$  is the phase of the shedding

$(A_L)_i$ ,  $(B_L)_i$ ,  $(A_D)_i$  and  $(B_D)_i$  are the geometric coefficients predicted by the moving, oscillatory dipole theory

where

$$(A_L)_i = \frac{C_i \Delta r_i \left(\frac{1}{2} \rho U_i^2\right)}{4\pi c R_i^2 (1-M_{R_i})^2} \left[ \vec{f}_{Li} \cdot \vec{v}_i - (\vec{x}_0 - \vec{x}_i) \cdot \left( \frac{\vec{f}_{Li}}{(1-M_{R_i})} \right) \left( \dot{M}_{R_i} + \frac{c}{R_i} (1 - M_i^2) \right) - (\vec{x}_0 - \vec{x}_i) \cdot \left( \dot{\vec{f}}_{Li} \right) \right]$$

$$(B_L)_i = \frac{\omega_i C_i \Delta r_i \left(\frac{1}{2} \rho U_i^2\right)}{4\pi c R_i^2 (1-M_{R_i})^2} \left[ - (\vec{x}_0 - \vec{x}_i) \cdot \vec{f}_{Li} \right]$$

$$(A_D)_i = \frac{C_i \Delta r_i \left(\frac{1}{2} \rho U_i^2\right)}{4\pi c R_i^2 (1-M_{R_i})^2} \left[ \vec{f}_{Di} \cdot \vec{v}_i - (\vec{x}_0 - \vec{x}_i) \cdot \left( \frac{\vec{f}_{Di}}{(1-M_{R_i})} \right) \left( \dot{M}_{R_i} + \frac{c}{R_i} (1 - M_i^2) \right) - (\vec{x}_0 - \vec{x}_i) \cdot \left( \dot{\vec{f}}_{Di} \right) \right]$$

$$(B_D)_i = \frac{\omega_i C_i \Delta r_i \left(\frac{1}{2} \rho U_i^2\right)}{4\pi c R_i^2 (1-M_{R_i})^2} \left[ - (\hat{x}_0 - \hat{x}_i) \cdot \hat{f}_{Di} \right]$$

$$\hat{f}_L = \begin{pmatrix} -\sin \psi \sin \phi + \cos \psi \sin \beta \cos \phi \\ \cos \psi \sin \phi + \sin \psi \sin \beta \cos \phi \\ \cos \beta \cos \phi \end{pmatrix}$$

$$\hat{f}_D = \begin{pmatrix} -\sin \psi \cos \phi - \cos \psi \sin \beta \sin \phi \\ \cos \psi \cos \phi - \sin \psi \sin \beta \sin \phi \\ -\cos \beta \sin \phi \end{pmatrix}$$

$$\dot{\hat{f}}_L = \Omega \begin{pmatrix} -\cos \psi \sin \phi - \sin \psi \sin \beta \cos \phi \\ -\sin \psi \sin \phi + \cos \psi \sin \beta \cos \phi \\ 0 \end{pmatrix}$$

$$\dot{\hat{f}}_D = \Omega \begin{pmatrix} -\cos \psi \cos \phi + \sin \psi \sin \beta \sin \phi \\ -\sin \psi \cos \phi - \cos \psi \sin \beta \sin \phi \\ 0 \end{pmatrix} \quad (37)$$

This equation can be further simplified to

$$P(t) = \sum_{i=1}^{10} \left[ (K_S)_i \sin (\omega_i \tau_i + \psi_i) + (K_C)_i \cos (\omega_i \tau_i + \psi_i) \right] \quad (38)$$

$$\text{where } (K_S)_i = (K_L)_i (A_L)_i + (K_D)_i (A_D)_i$$

$$(K_C)_i = (K_L)_i (B_L)_i + (K_D)_i (B_D)_i$$

The assumption that the aerodynamic and geometric parameters remain constant in a 0.005-second time slice is now applied. The term  $\omega_i \tau_i$  is replaced by  $\omega' t$ , where  $\omega'_i$  is the Doppler shifted

frequency at the observer's location. Equation (38) then becomes for each blade

$$P(t) = \sum_{i=1}^{10} (K_S)_i \sin(\omega_i' t + \psi_i) + (K_C)_i \cos(\omega_i' t + \psi_i) \quad (39)$$

The exact time interval chosen to solve for the oscillatory forces was 0.0046 second. The rate at which the data was electronically digitized was 11.3 kHz. Therefore, there are 52 measured values of the recorded pressure in each 0.0046-second time interval. Linearizing Equation (39) by removing the arbitrary phase gives

$$P(t_i) = \sum_{i=1}^{10} \left[ (K'_S)_i \sin(\omega_i' t_i) + (K'_C)_i \cos(\omega_i' t_i) \right] \quad (40)$$

$$i = 1, \dots, 52$$

where  $\sqrt{(K'_S)_i^2 + (K'_C)_i^2} = \sqrt{(K_S)_i^2 + (K_C)_i^2} = K_i$

and  $K_i$  is the total magnitude of the oscillatory force constants. Since there are 20 unknowns in Equation (40), ten  $(K_S)_i$  and ten  $(K_C)_i$ , and 52 equations, the problem is overdetermined. The solution was determined using the standard least squares techniques for a set of linear equations.

#### Obtaining Experimental Main Rotor Vortex Noise

The acoustical pressure-time history recorded at the microphone position is assumed to be a linear superposition of many sources of noise. Among these sources are:

1. Engine noise
2. Engine exhaust noise
3. Main and tail rotor gearbox noise
4. Tail rotor rotational noise
5. Main rotor rotational noise
6. Main rotor vortex noise
7. Tail rotor vortex noise

Since the analyses that were performed herein are associated with only main rotor vortex noise, item (6), all the other sources of noise in the measured pressure-time histories had to be removed in order to obtain the desired pressure-time history.

In the model developed in this contract, the noise associated with rotor blade vortex shedding is assumed to be generated at discrete frequencies defined by a Strouhal formulation. These shedding frequencies are determined by the airfoil's chord, thickness, angle of attack and velocity. Shedding frequencies, while in part determined by rotor rotational speed, are not integral harmonics of the rotor rotational frequency. In addition, since the blade is moving and continually changing direction, the Doppler shift on these frequencies also continually changes. This differs from items 1, 2, 3, 4, and 5 of the listed sources of noise which are observed at discrete frequencies. This is clearly illustrated by Figure 17, the spectrum of measured helicopter rotor noise for the hover flight condition. The rotor rotational noise appears at discrete multiples of the blade passage frequency (10.8 Hz), and the tail rotational noise occurs at multiples of its blade passage frequency (55.1 Hz). The peaks at 1922 Hz and 2133 Hz are identified with the tail-rotor gear clash frequencies of the 42-degree and 90-degree (second harmonic) gears. The frequencies are slightly shifted from the ones given in Table II because of the inability of the helicopter to hold an exactly constant RPM. No other engine or transmission noise is observed in this data (see Table II). This is believed to be due to the generally higher frequency content of these sources of noise and the large distance of the microphone from the helicopter.

Figure 17 shows that the rotational and discrete noise peaks are sufficiently narrow that they can be removed without significantly changing the content of the underlying broadband noise. Once the discrete noise peaks are identified, their corresponding Fourier coefficients, as determined from the fast Fourier transform of the digitized data, are set equal to zero. The broadband pressure-time history is then generated by using the inverse Fourier transform.

In order to correlate the measured pressure-time history with the theory, the azimuthal blade position must be known. The Wallops Island test did not record this important information. The azimuthal location of the rotor was determined by matching the measured rotational noise signature with a theoretically predicted rotational noise pressure-time history.

#### Results of the Theoretical Analysis

Four hover cases were analyzed. Three of these cases were from position 4 (200 feet to the right of the helicopter) and one from position 6 (700 feet to the right of the helicopter). The radial stations selected were:

$$r_i = 7, 9, 11, 13, 15, 17, 18.5, 19.5, 20.5 \text{ and } 21.5 \text{ ft}$$

**TABLE II. GEAR MESH FREQUENCIES OF UH-1B DRIVE TRAIN  
FOR ENGINE OUTPUT SHAFT SPEED OF 6600 RPM**

Transmission Group	RPM	Number of Teeth	Gear Mesh Frequency (Hz)
<b>Main Transmission:</b>			
Input Drive Shaft Pinion	6600	29	3190
1st Stage Planetary Pinions	3843	31	1986
2nd Stage Planetary Pinions	1245	31	643
Center Shaft Bevel (Lower)	3090	55	2833
Tail Rotor Output Shaft Gear	4140	27	1863
Generator Quill	-	-	4510
<b>Tail Rotor Transmission:</b>			
42-Degree Gearbox Bevel	4300	27	1935
90-Degree Gearbox Bevel	4300	15	1075
<b><u>Engine Group</u></b>			
<b>Gearbox:</b>			
1st Stage Pinions	-	-	6150
2nd Stage Pinions	-	-	3590
<b>Accessory Drive Gearbox:</b>			
Accessory Drive Pinion	-	-	10595
Accessory Drive Gear	-	-	4162
Oil/Air Separator Shaft Gear	-	-	2973
Oil Pump Drive Shaft Gear	-	-	2973
Tachometer Drive Shaft Gear	-	-	2727
Fuel Control Drive Shaft Gear	-	-	2973
<b>NOTE: All blade passage frequencies of the power turbine, gas producer, axial compressors and centrifugal compressor are above 10000 Hertz.</b>			

for  $i=1$  to 10 respectively. The electronically digitized records are  $\sim 1.5$  seconds long. Therefore, 15 blade passages were analyzed for each of the cases.

The set of equations solved had more equations (52) than unknowns (20). By using the least-squares method, the resulting deviation is a measure of the quality of the solution. Since the Strouhal number is not accurately known for airfoils at these Reynolds numbers, a search was performed to determine the Strouhal number which gave the most satisfactory solutions. The optional Strouhal number was determined to be  $0.235 \pm .02$ , which is within the range for which results have been obtained by previous investigations.

One of the recordings obtained 200 ft to the right was used to evaluate the method of removing discrete rotational noise sources. The portion of the recording used was 35 seconds into the recorded signal. The total recorded pressure-time history for this portion of the recording is shown in Figure 34, and the spectrum analysis of the signal is presented in Figure 35. In the first of the four cases (to be referred to as Case A), for all noise below 140 Hz, the tail rotor peaks at 165 Hz and 220 Hz, and all noise above 1860 Hz was removed. The spectra of the noise removed are shown in Figure 36, and the remaining spectrum that is assumed to be associated with vortex noise is shown in Figure 37. The pressure-time history corresponding to the discrete noise (the main and tail rotor rotational noise and the tail rotor transmission noise) spikes at 1930 Hz and 2140 Hz is shown in Figure 38. The pressure-time history of the remaining "vortex" noise for Case A is shown in Figure 39. Comparison of the "vortex noise" pressure-time history (Figure 39) and the discrete noise pressure-time history (Figure 38) with the pressure-time history of the total measured signal indicates that the majority of the high frequency content is associated with "vortex noise" and not with discrete noise such as main and tail rotor rotational noise. While it is evident in the pressure-time history of the total noise signal, the increase in the level and amount of high frequency noise at each blade passage is very obvious and undisputable.

In Case B, all noise above 2820 Hz was removed (instead of above 1860 Hz as in Case A), together with the gear clash spikes at around 1930 Hz and 2140 Hz. The spectra for the removed noise and the remaining noise, as well as the pressure-time history of the remaining noise, are shown in Figures 40, 41 and 42 respectively. Comparing the pressure-time histories presented in Figures 39 and 42 indicates that the higher cutoff frequency did not notably change the character of the pressure-time history of the vortex noise.

In order to determine how much the results were dependent on when the data were analyzed, another portion of the data taken 200 feet to the right and 26 seconds into the recording was analyzed. This condition is referred to as Case C. The electronically digitized pressure-time history and spectrum for this case are shown in Figures 43 and 17 respectively. The rotational and discrete noise was removed by setting the following coefficients of the Fourier representation of the digitized record equal to zero: <140 Hz, 165 Hz, 220 Hz, 1930 Hz, 2140 Hz, and >2820 Hz. Figure 44 presents the spectrum of the noise that was removed, and Figure 45 presents the spectrum of the vortex noise that was analyzed for this case. The pressure-time history of the rotational noise is shown in Figure 46 and of the vortex noise in Figure 47.

The fourth case that was analyzed (Case D) was data measured 700 feet to the right of the helicopter. A portion of the recording 26 seconds into the record was analyzed. The pressure-time history and spectrum of this data are shown in Figures 28 and 18 respectively. In this position, the gear clash frequencies occur at 1930 Hz and 1990 Hz. The peak at 1990 Hz corresponds to the gear clash frequency of the first-stage planetary pinion (see Table II). The frequency components removed were <140 Hz, 165 Hz, 220 Hz, 276 Hz, 330 Hz, 385 Hz, 1930 Hz, 1990 Hz, and >2820 Hz. The spectra and pressure-time histories for the noise removed and remaining are presented in Figures 49, 50, 51, and 52. The pressure-time history of the rotational noise is considerably different than that at the 300 ft position; and the pressure-time history of the vortex noise, while having the same general characteristics of those at 200 ft, has some different features. The analyses that were carried out used 15 blade passages of digitized data. Because of the inability to separate the lift and drag components and because the drag contribution is insignificant compared to the lift distribution, the  $(K_D)_i$ 's were assumed zero in all of the analyses that were conducted. Therefore, only  $(K_L)_i$ 's were calculated for the 15 blade passages in each case. For each radial station, the distribution of these 15  $(K_L)_i$  values multiplied by that station's dynamic pressure is shown in Figure 53. The  $(K_L)_i (1/2\rho U_i^2)$  for the ten radial stations for each of the four cases are tabulated in Table III and plotted in Figure 54. Although there is some scatter in each of the distributions, the mean results are remarkably similar for all four cases. The comparison of Case A and Case B shows that the results are fairly insensitive to variations in the high frequency cutoff in the data, although the magnitudes of station 10 for Case A are somewhat suppressed from Case B. Going to a

TABLE III. MAGNITUDES OF THE OSCILLATORY LIFT FORCES AS A FUNCTION OF RADIAL POSITION FOR EACH OF THE FOUR CASES								
Station Radius	Angle of Attack	Mach Number	Shedding Frequency	Oscillatory Pressure (lb/ft <sup>2</sup> )				
(ft)	(deg)		(Hz)	Case A	Case B	Case C	Case D	
7.0	5.9	0.22	217	20.20	19.30	30.50	30.60	
9.0	5.6	0.28	284	20.00	20.00	20.00	23.10	
11.0	5.2	0.34	354	8.25	8.95	13.90	18.50	
13.0	4.7	0.40	431	4.80	4.45	4.45	11.30	
15.0	4.2	0.46	512	2.10	2.10	2.10	2.05	
17.0	3.6	0.52	594	1.30	1.05	1.05	1.87	
18.5	3.1	0.57	658	1.20	0.98	1.60	1.56	
19.5	2.8	0.60	702	0.83	0.91	0.87	2.55	
20.5	2.5	0.63	745	0.41	0.50	0.60	1.06	
21.5	2.2	0.66	787	0.20	0.55	0.40	0.83	

different position of the record also does not significantly alter the distributions (see distributions for Case C). Some of the distributions for position 6 (Case D), however, do differ from the first three cases. This is due, in part, to the differences in ground reflection. The magnitudes of the oscillatory pressures are  $\sim 1$  to  $2 \text{ lb/ft}^2$  for the tip  $1/3$  of the blade (14-22 ft). On the inboard stations (6-14 ft), the magnitude of the oscillatory pressure ranges from 4 to  $30 \text{ lb/ft}^2$ . These higher values associated with the inboard stations are due in part to the fact that the retreating blade's range of Doppler-shifted shedding frequencies is the same as the frequency range associated with the inboard stations of the advancing blade. Therefore, the calculated amplitudes for inboard stations of the advancing blade contain the noise energy of the retreating blade. For each of the four cases that were analyzed, the calculated oscillatory forces were used in a theoretical program to determine if the essential noise characteristics had been retained. For each of the cases, therefore, a pressure-time history and a corresponding spectral analysis were predicted for comparison with the experimental data. The predicted pressure-time history and the corresponding spectrum for Case A are shown in Figures 55 and 56 respectively. When these predicted results are compared with the measured results in Figures 39 and 37, it is seen that the calculated oscillatory forces have retained all of the essential characteristics of the measured pressure-time history. Similar comparisons can be made for Cases B, C and D. For example, Figures 57 and 58 should be compared with Figures 42 and 41 for Case B; Figures 59 and 60 should be compared with Figures 47 and 45 for Case C; and Figures 61 and 62 should be compared with Figures 52 and 50 for Case D.

### Forward Flight Analysis

Calculations similar to those carried out for hover were conducted for a high-speed forward flight case ( $\mu=0.28$ ). The helicopter was at 100-ft altitude and flew over the data cross in the X-direction (see Figure 4) at 208 ft/sec. This problem is considerably more difficult than hover for the following reasons:

1. The helicopter's position at any instant of time was measured only to within 45 ft (Reference 12).
2. The Doppler effect makes it more difficult to separate the discrete rotational and gearbox noise.
3. The rotor wake and blade loads are not as easily or accurately calculated.

4. There is an azimuthal variation in the aerodynamic parameters such as angle of attack, inflow velocity and flow velocity.

To improve on the uncertainty of the helicopter's position, the period of rotational noise as a function of time was matched to a predicted Doppler shift dependence. For these calculations the helicopter was assumed to be in straight and level flight with altitude and velocity constant as given by the radar measurements. The rotor RPM was assumed to be 324. Figure 63 shows the period of each blade passage as a function of time. As expected, the period is small where the helicopter is far away and approaching, and gradually increases until it is large and relatively more constant when the helicopter is far away and receding. These limiting frequencies (at  $\pm 2$  sec) from the measured data correspond exactly to the Doppler shifts expected for this flight configuration. The curve superimposed on the data is the predicted period time history. From this plot the time in the record corresponding to the helicopter crossing at ground zero can be determined with an error of only one blade passage or 20 ft, which is considerably better than the measured data.

The portion of the record electronically digitized for the forward flight case was chosen so that the helicopter was near the data cross. For this helicopter position, as in the hover case, the advancing blade dominates the retreating blade noise, and the Doppler shift on the advancing blade oscillating dipsles enables the accurate separation of the noise from the advancing and retreating blades. The advancing blade location means the blade is advancing toward the observer, and for microphone position 4, this corresponds approximately to  $\psi=0^\circ$ . The aerodynamic environment of the blade for this case is similar to that of hover, since the flow caused by the helicopter forward velocity is only along the blade. When the blade is at  $\psi=90^\circ$ , some frequency separation is expected, since the flow, and hence the shedding frequency, is higher on that blade than on the blade at  $\psi=270^\circ$ .

Figure 64 shows the retarded time diagram for the two-bladed UH-1B in forward flight. The values of the wake inflow velocity were calculated using a deformed wake analysis developed by RASA and presented in Reference 17. The rotational noise was removed using a technique similar to that used in hover. However, because of the broadening of the periodic noise spikes caused by Doppler effects, the periodic noise was removed by zeroing out the Fourier coefficients below 280 Hz and above 1860 Hz.

For the time intervals when the blade was advancing toward the observer's location, the results of the analyses were in complete agreement with the hover data; therefore, the hover results also apply for this forward flight case.

## GENERAL COMMENTS AND SPECIFIC CONCLUSIONS

The technique of electronically digitizing and analyzing measured sound pressure-time histories to create high resolution spectra, such as shown in Figure 17, has permitted the detailed analysis of various rotor sources. For example, the fine frequency resolution that can be obtained by these techniques allows separation of the individual peaks associated with main rotor and tail rotor rotational noise and discrete sources such as oil pumps, gearboxes, etc., from the broadband noise. Since these types of noise sources can now be adequately separated, the characteristics of the various noise sources can be studied independently. The study stressed the analysis of the broadband noise rather than the rotational noise, although the rotational and discrete noise sources were separated from the total noise signature and studied as regards the characteristics of their pressure-time history. Figures 38, 46, and 51, for example, show the pressure-time histories of the rotational and discrete noise sources for the various cases that were studied. While the general characteristics of these noise sources are the same, there are noticeable differences. For example, comparing the signatures shown in Figures 38 and 46 which were recorded at different times but at the same location during a hover flight condition, it can be seen that in one case the tail rotor signature was more pronounced than in the other case. It is believed that this is due to the fact that the helicopter was not holding a constant heading at all times. Comparing Figures 46 and 51, it can be seen that for a given time, the effect of microphone location can change the character of the pressure-time history: at 700 feet from the aircraft the tail rotor signature was very pronounced, whereas at 200 feet it is hardly distinguishable.

It is apparent from this brief analysis that considerable care must be utilized in evaluating the relative importance of various sources of helicopter noise based on a given recording, since many geometric and environmental parameters must be properly considered in the evaluation. For any future studies of the type conducted herein, controlled tests in the hover condition should be undertaken so that the effects of blade loading, Mach number, etc., can be adequately recorded and documented.

The vortex pressure-time histories (Figures 39, 42, 47, and 52) that were generated from the total experimental pressure-time histories by removing the rotational and other discrete noise have the same general characteristics. The signals are essentially random, with a modulation in amplitude occurring every blade passage. The high amplitude region has higher frequency than the low amplitude regions. This feature is consistent

with the Doppler effect discussed previously, i.e., the advancing blade towards the observer raises the frequency and magnitude of any oscillatory pressure amplitudes recorded at an observer's location. Each blade passage, however, is distinctly different in its structure. In order to evaluate the effect of this difference on the sound signature of vortex noise, each blade passage of the digitized vortex signal was converted to an analog signal and then repeated so that a 5-second analog record of each particular blade passage could be constructed on tape. When a series of each of these 5-second records was played on a tape recorder, each blade passage sounded distinctly different. Qualitatively, this difference from blade passage to blade passage may be described as a modulated signal of varying frequency or "tone". That is, when listening to a series of blade passage recordings, a different frequency content may be discerned in each of the blade passages.

The vortex shedding model allowed a finite frequency range to be "fit" to the experimental pressure-time history. The relative magnitudes of each of the radial station's oscillatory forces reflected the frequency content of the signal received at the observer for that blade passage. Thus, since the signal varies from blade passage to blade passage, both in frequency and magnitude, the oscillatory pressures calculated at the helicopter blade had a corresponding variation. Since each blade passage is different, each calculation performed results in a slightly different radial array of oscillatory forces. This effect is shown in the histograms (see Figure 53), which illustrate how these oscillatory pressures varied at each radial station over the 15 blade passages for each of the four cases that were analyzed. Histograms plot the frequency of occurrences of a given event. In this case, the histograms record the frequency of occurrence of the calculated oscillatory lift forces in a given range. Figure 53 shows that the scatter of results increases as the radial station decreases, which relates to the gradual degeneracy of the solution technique as the frequency of shedding on the blade decreases. The amount of scatter of a station corresponds to the variability of the amplitude appropriate to that station contained in the experimental record. Thus, for Case C, the amplitude appropriate to station 2 was changing significantly from blade passage to blade passage while the amplitude appropriate to station 6 changed little from blade passage to blade passage.

The mean values for each of these distributions were determined. The mean values are listed in Table III and plotted in Figure 54. The shedding frequencies appropriate to the helicopter rotor reference system are listed, as well as the Mach number and angle of attack.

The advancing blade has its shedding frequencies raised and spread apart, while the retreating blade has its shedding frequencies lowered and pushed together. The Doppler shifted frequencies on the advancing blade range from about 275 Hz at 7 ft radius to 2100 Hz at 21.5 ft radius. The exact amount of the shift depends on the observer's location relative to the velocity of that blade station. The Doppler-shifted frequencies on the retreating blade range from 180 Hz at 7 ft radius to about 500 Hz at 21.5 ft radius. Hence, the outboard section of the advancing blade is associated with high-frequency noise; and the inboard section of the advancing blade, together with the retreating blade, is associated with low-frequency noise. For the observer, the radial stations at 7 ft and 9 ft on the advancing blade are in the same frequency range as the retreating blade because of the Doppler effect; hence, these stations also reflect the noise energy of the retreating blade. This contribution partially leads to higher values of oscillatory pressure calculated at these radial stations. The noise energy of the entire retreating blade has been lumped into these two stations.

As shown in Figure 54, the decreasing oscillatory pressure magnitudes at larger blade radius reflect the gradual fall-off with frequency of the noise energy shown in the spectra (see Figure 17 for example). The spectra generated in this analysis compare well with the findings of Cox and Lynn, Reference 18, in that the major source of audible vortex noise is concentrated in the frequency range of 200 Hz to 500 Hz. The maxima and minima in these spectra caused by ground reflection also affect the calculated oscillatory pressures, as the model does not include this reflection effect.

The mean oscillatory pressures have been used to create a pressure-time history at an observer's station. These created pressure-time histories and these spectra compare very well with the experimental pressure-time histories and spectra, see Figures 55, 56, 39 and 37 for example. Audio tapes created from the calculated pressure-time history sound like the experimental tapes except for the amplitude variation from blade passage to blade passage eliminated by using the mean values.

Since the essential characteristics of the experimental acoustic signal can be duplicated with these mean oscillatory forces in a rotating blade frame of reference, it is possible with proper parameterization of the force constants to effectively simulate the noise produced by helicopter rotors for a variety of operating conditions. Because of the advanced data analysis procedures that have been developed, the rotational and broadband vortex noise can be separated and studied independently. It is therefore possible to parameterize the vortex noise and the rotational noise as functions of the rotor geometric and

operating conditions such as number of blades, rotational speed, thrust, chord, and twist. The parameterization of the vortex noise and rotational noise can be carried out by analyzing various rotor data from whirl tower tests, as was done in this program for a hovering helicopter. Once the parameterization has been accomplished for a number of different rotor systems, it should be possible to predict the acoustic signature of any rotor system given only the geometric and operating conditions of the helicopter.

## CONCLUSIONS

The analyses carried out in this investigation showed that random or "vortex" noise is a major source of noise from a helicopter, particularly in the hover condition. For the cases analyzed, main rotor rotational noise was not significant above 100 Hz, and the major audible sources of vortex noise were concentrated in the frequency range of 200 to 500 Hz. In their respective frequency ranges, the main rotor rotational noise was about 30 db above the threshold of hearing while the vortex noise was about 45 db above a normal background noise. The effect on an acoustic spectrum of the filter bandwidth and the time length of data was that as the time period decreased or the filter bandwidth increased, the resolution of the spectrum decreased.

The following specific conclusions were drawn:

1. Ground reflection effects can significantly distort the radiated acoustic pressure-time history.
2. The broadband noise created by a helicopter rotor can be represented by Kármán-street vortex induced noise.
3. The "vortex" noise theory fit the data best for a Strouhal number of 0.235.
4. The basis of a technique by which the acoustic signature of any rotor system can be predicted in hover or forward flight has been developed and demonstrated.
5. A new technique has been developed whereby significantly improved high resolution acoustic spectra can be generated.
6. While acoustic spectra of helicopter flybys can be generated, the information that can be obtained from such spectra is marginal because of the effects of Doppler shift and changing propagation distance.

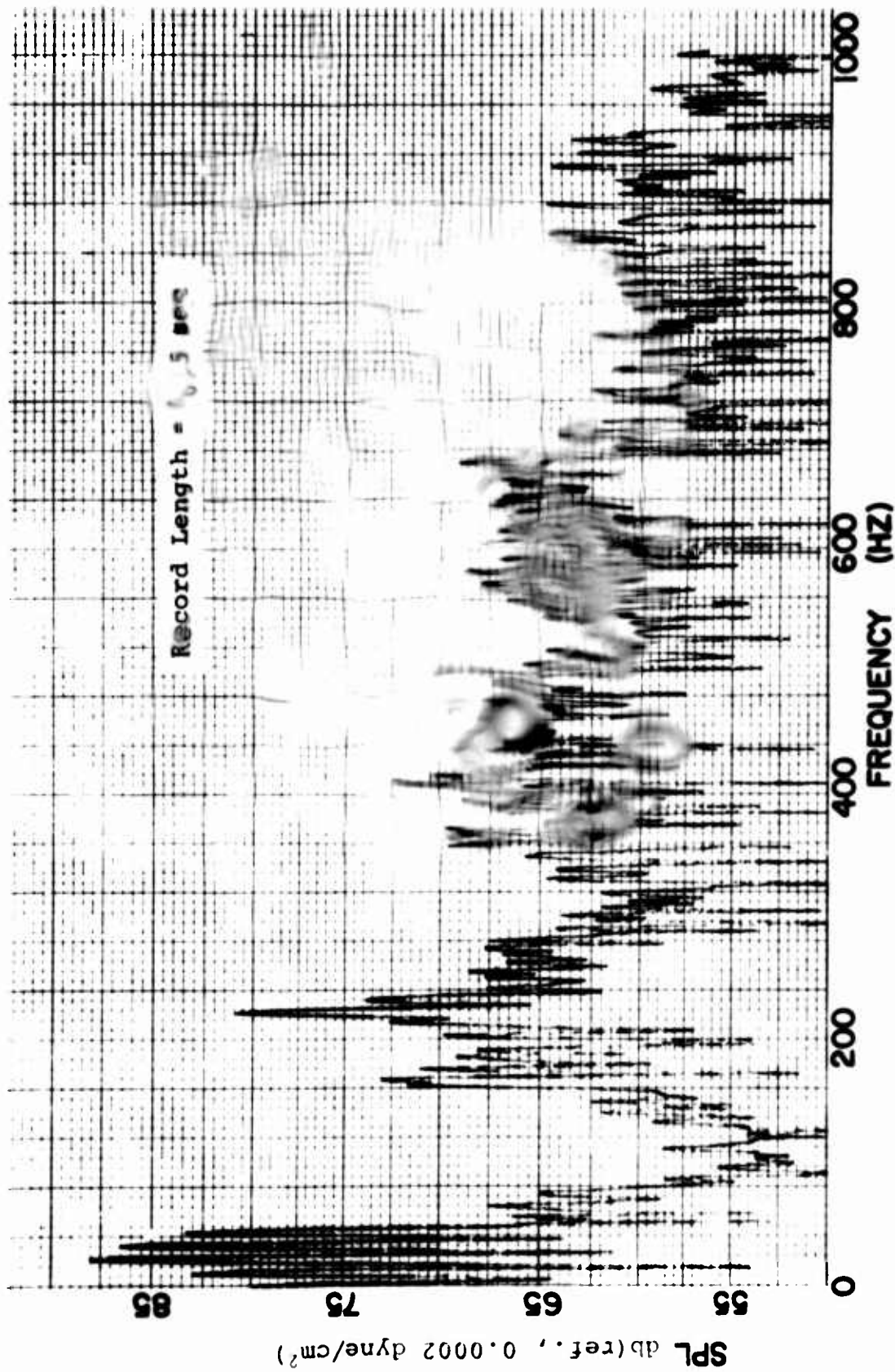


Figure 1. Noise Spectrum by Ubiquitous Analyzer for UH-1B Helicopter in 100-ft Hover; Recorded at 200 ft to the Right.

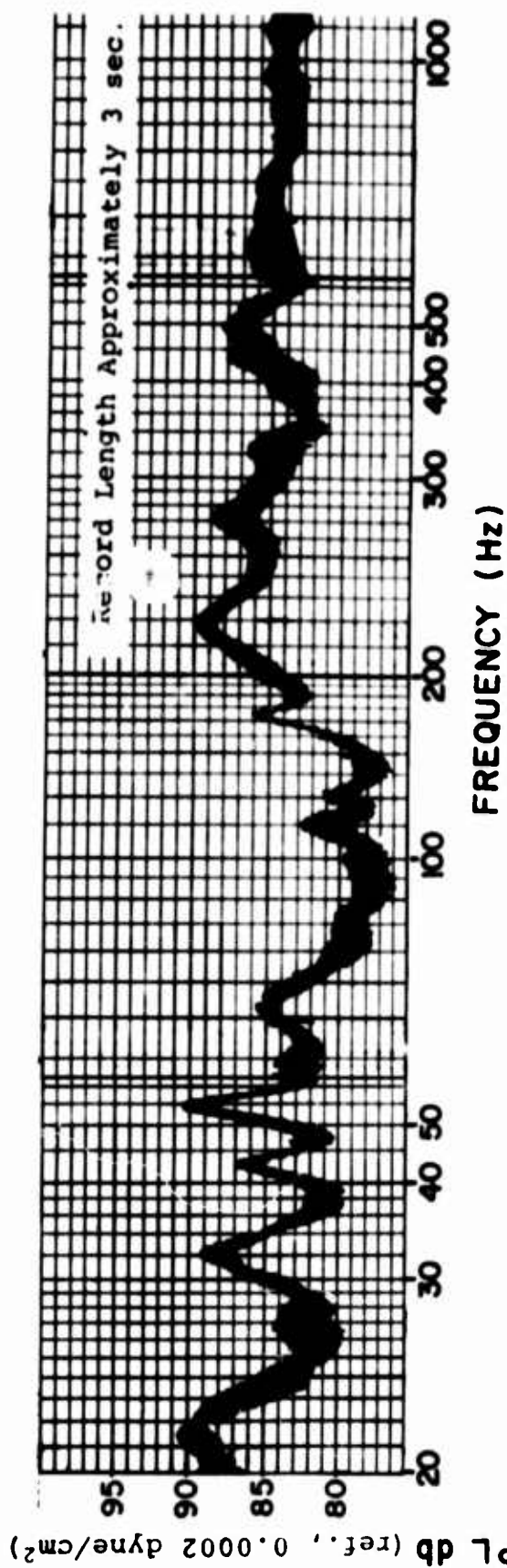


Figure 2. Noise Spectrum by B & K Constant-Percent Analyzer for UH-1B Helicopter in 100-ft Hover; Recorded at 200 ft to the Right.

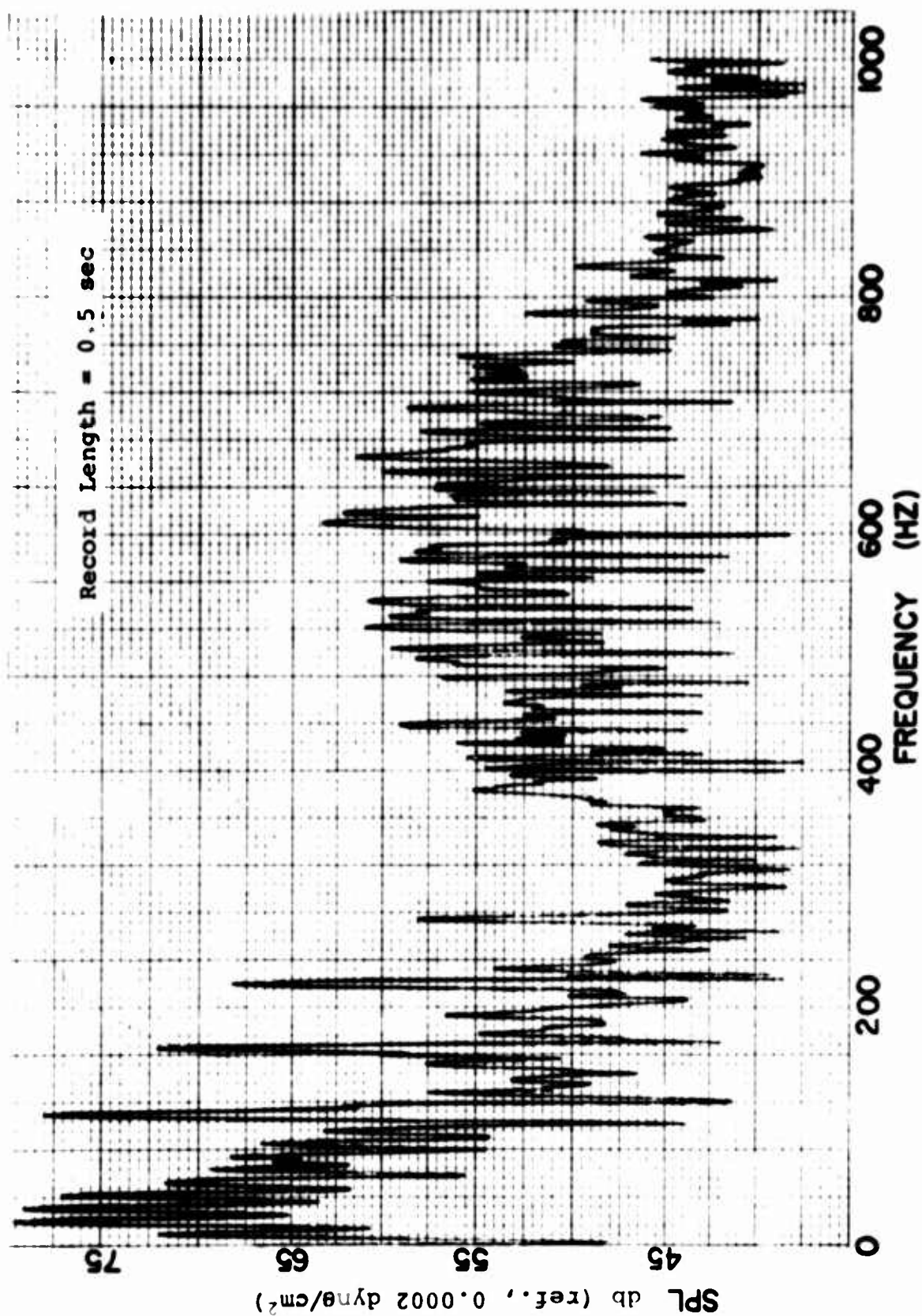
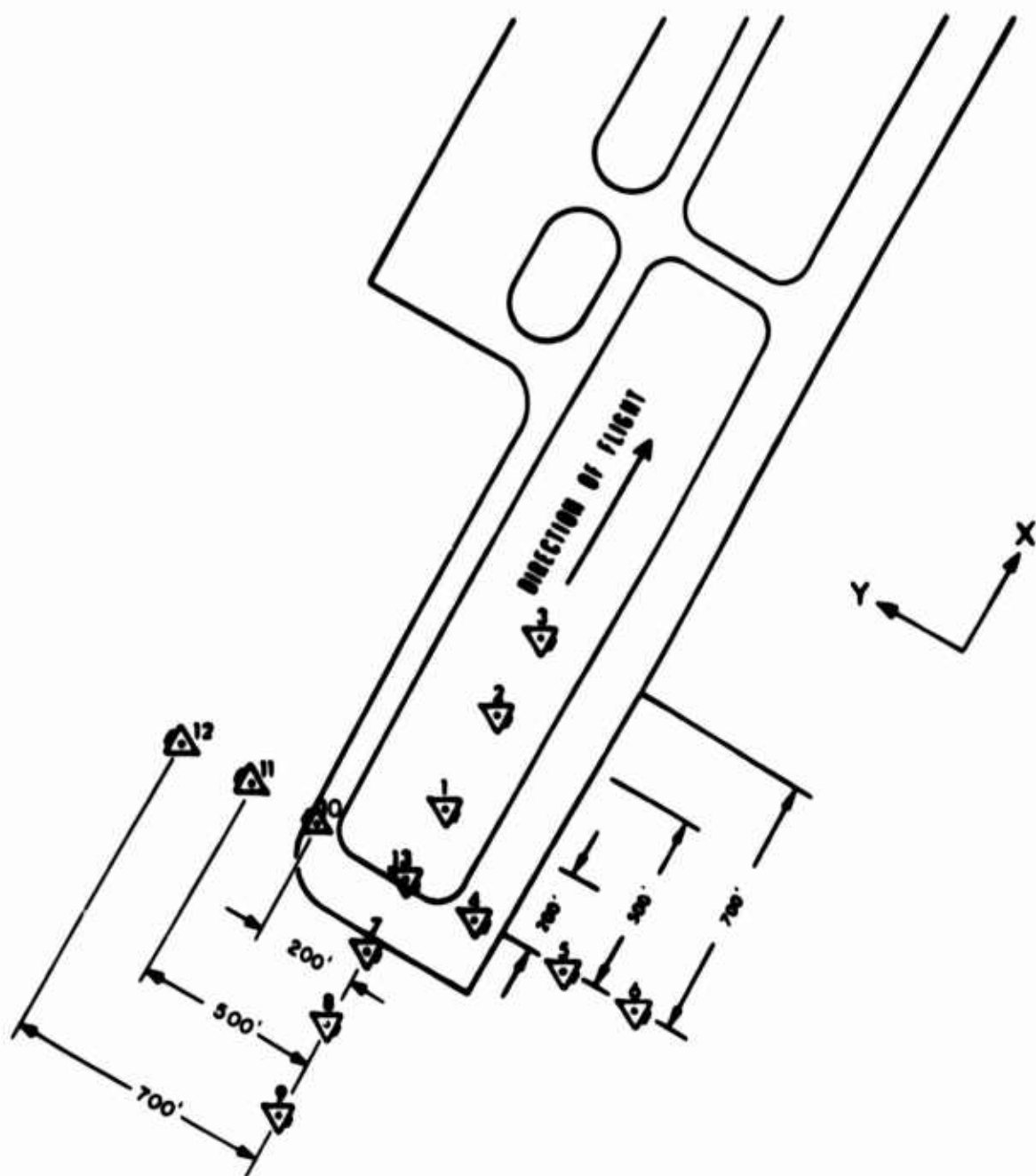


Figure 3. Noise Spectrum by Ubiquitous Analyzer for UH-1B Helicopter in 100-ft Hover; Recorded at 700 ft to the Right.



**△ MICROPHONE LOCATION AND DIRECTION DURING FLYBY**

**Figure 4. Relative Positions of Microphones at Wallops Island Air Station.**

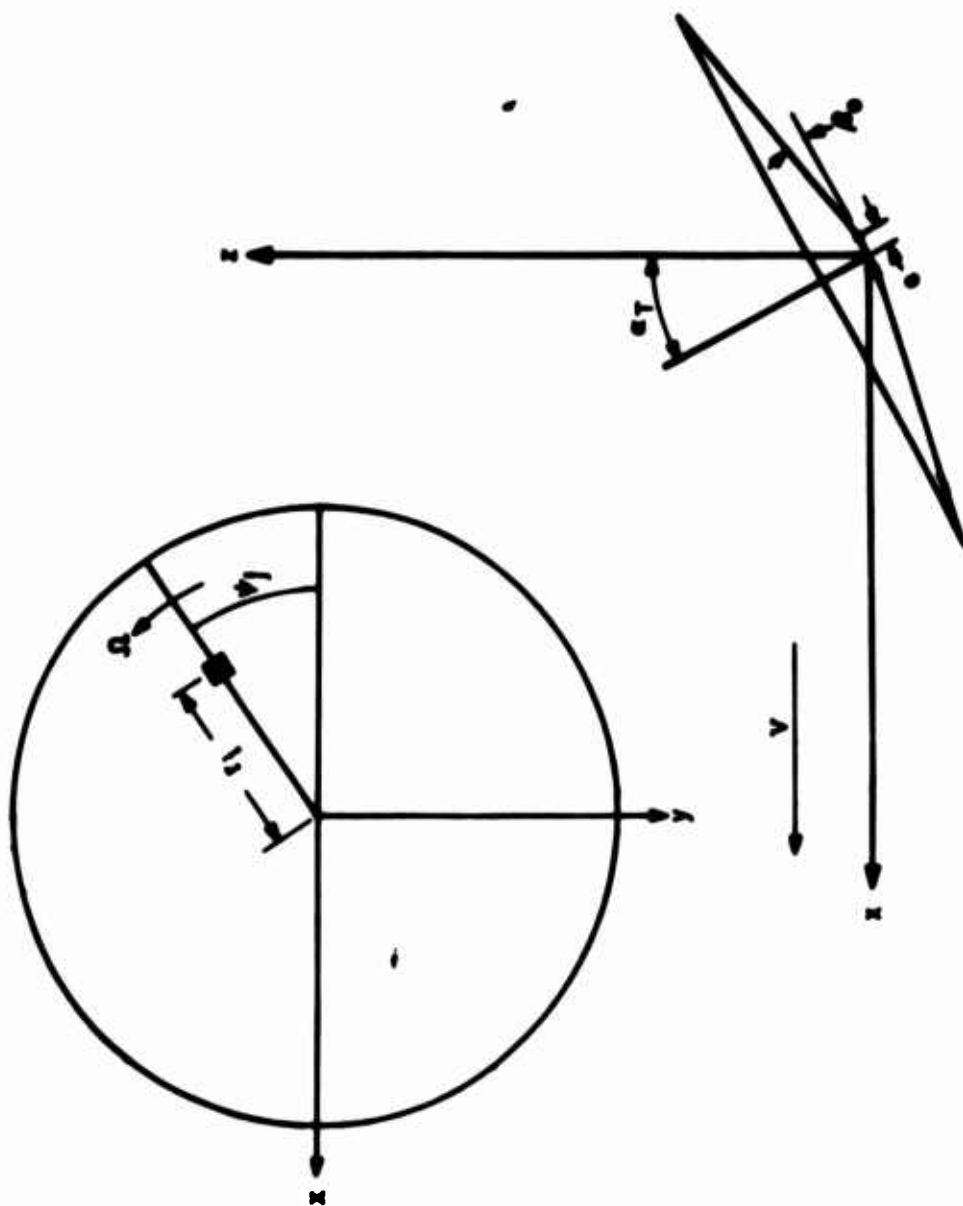
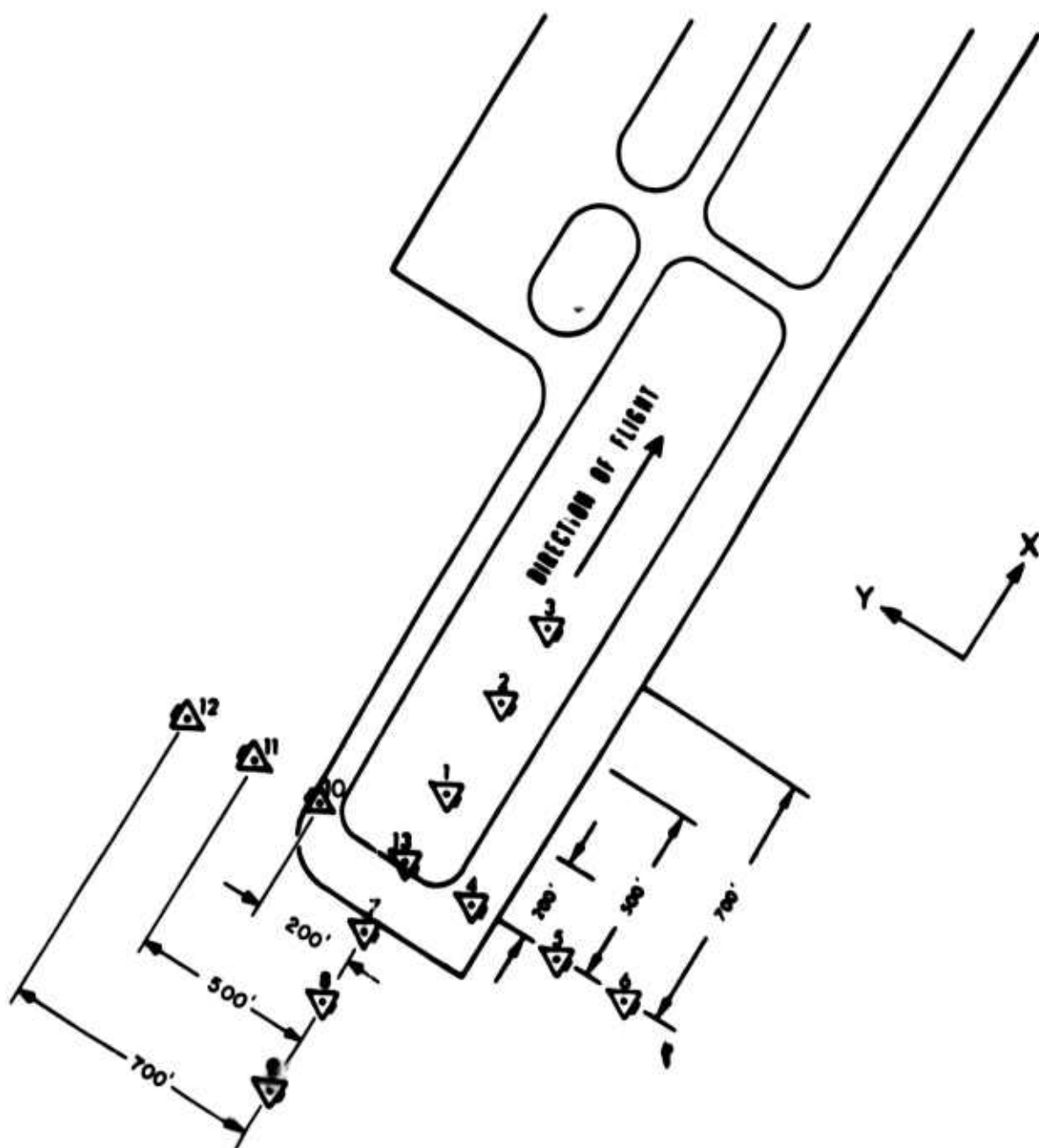


Figure 5. Tip-Path Plane Coordinates.



**△ MICROPHONE LOCATION AND DIRECTION DURING FLYBY**

Figure 4. Relative Positions of Microphones at Wallops Island Air Station.

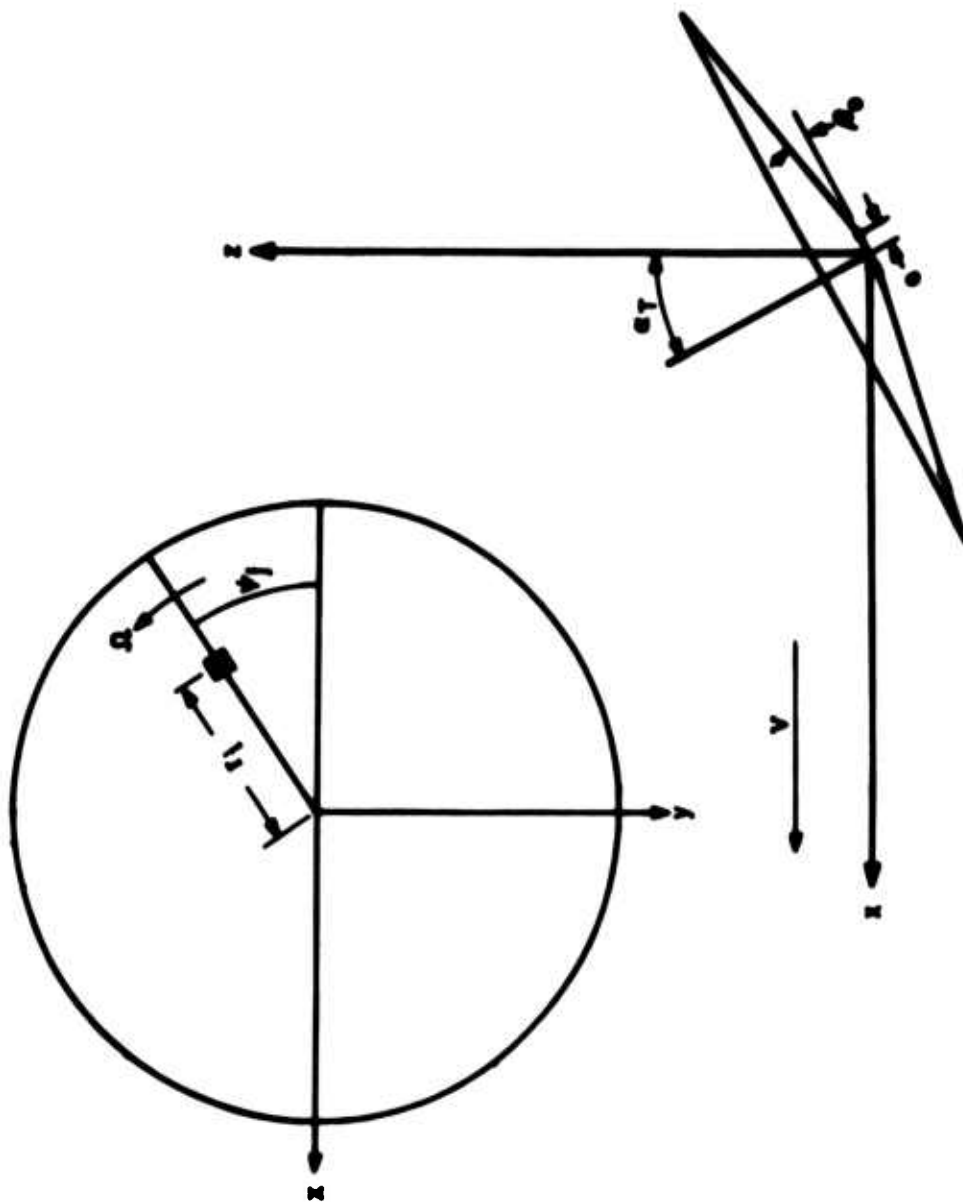


Figure 5. Tip-Path Plane Coordinates.



Figure 6. Oscillograph Recording of Pressure-Time History for UH-1B in 100-ft Hover; Recorded at 200 ft to the Right.

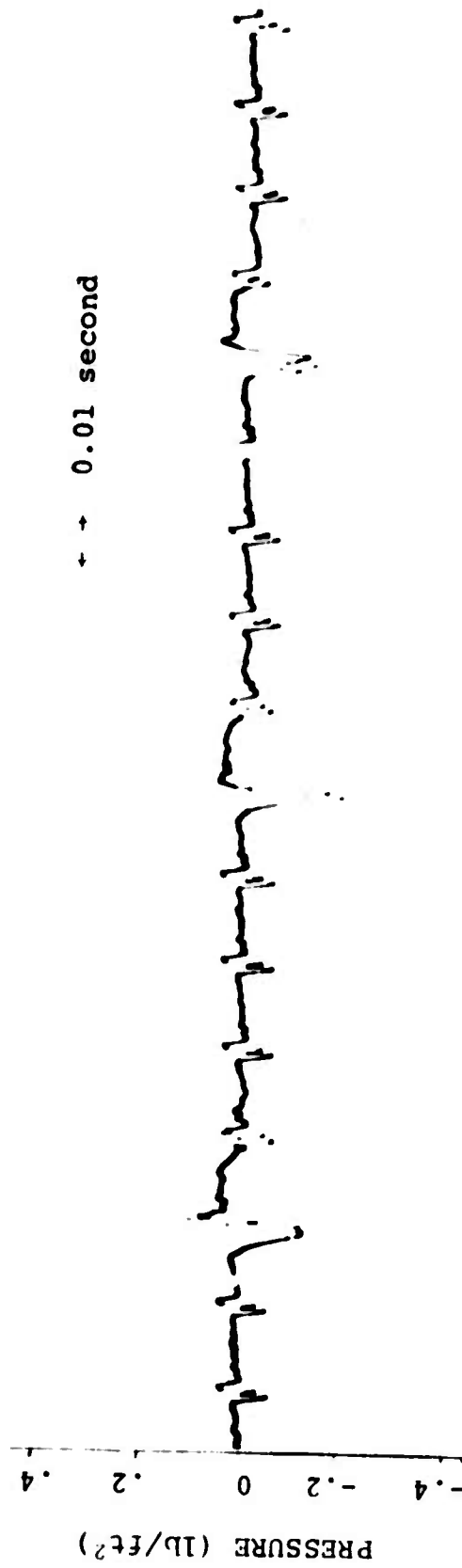


Figure 7. Oscillograph Recording of Pressure-Time History  
for UH-1B Approaching at 115 Knots Level Flight;  
Recorded at 200 ft to the Right.

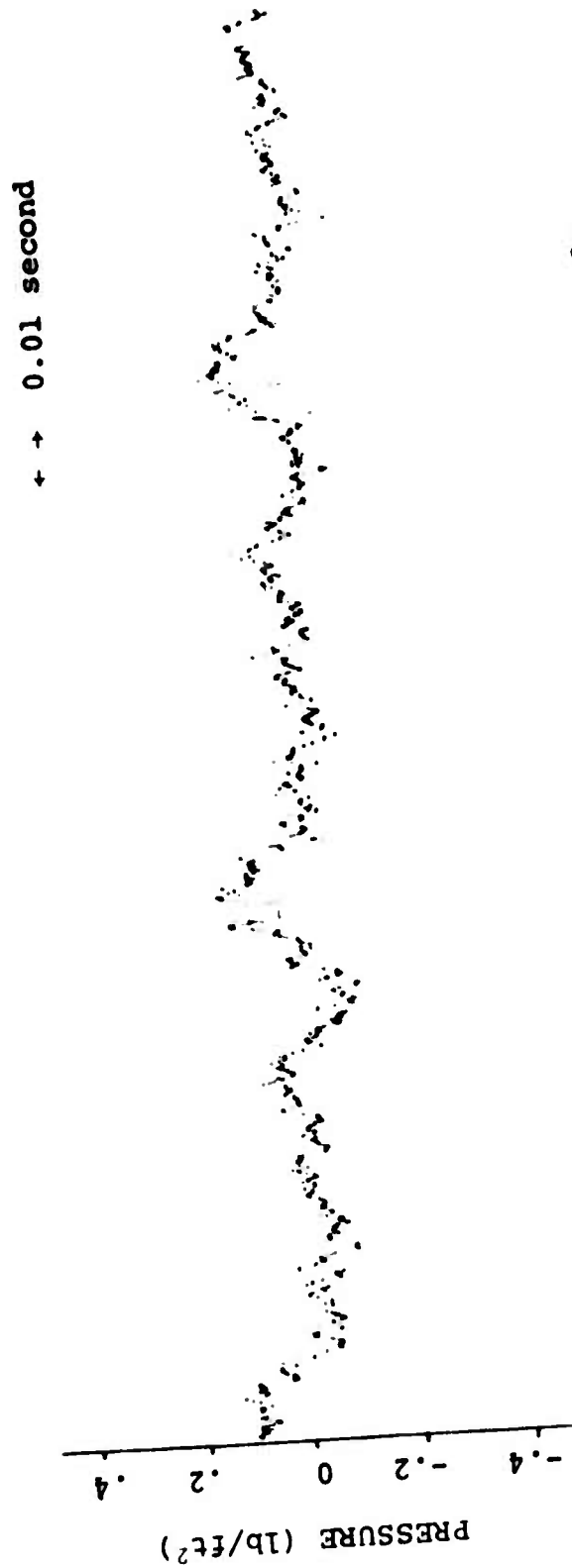


Figure 8. Oscillograph Recording of Pressure-Time History for  
UH-1B Over Ground Zero at 115 Knots Level Flight;  
Recorded at 200 ft to the Right.

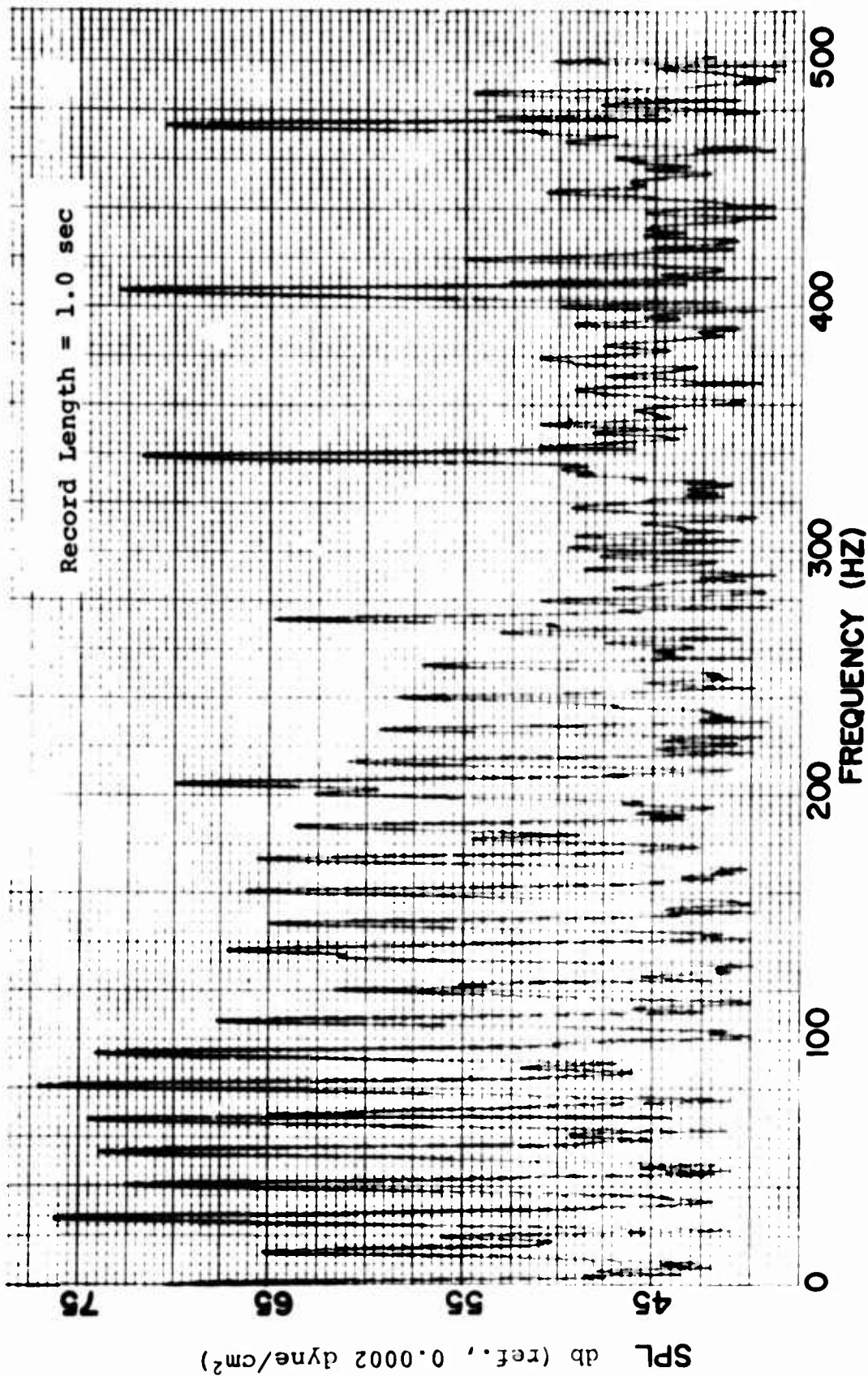


Figure 9. Noise Spectrum by Ubiquitous Analyzer for UH-1B Approaching at 115 Knots Level Flight; Recorded at 200 ft to the Right.

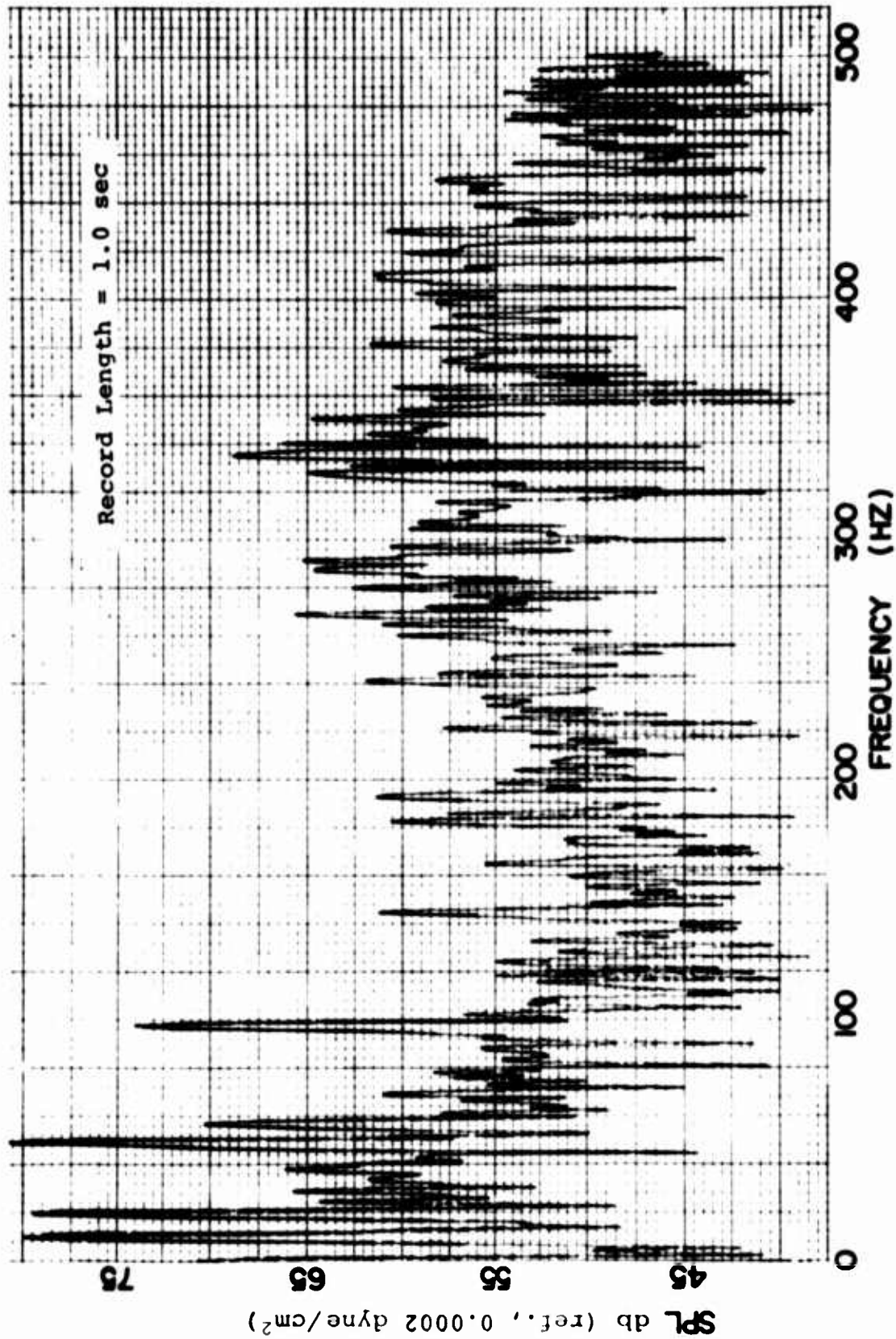


Figure 10. Noise Spectrum by Ubiquitous Analyzer for UH-1B Over Ground Zero at 115 Knots Level Flight; Recorded at 200 ft to the Right.

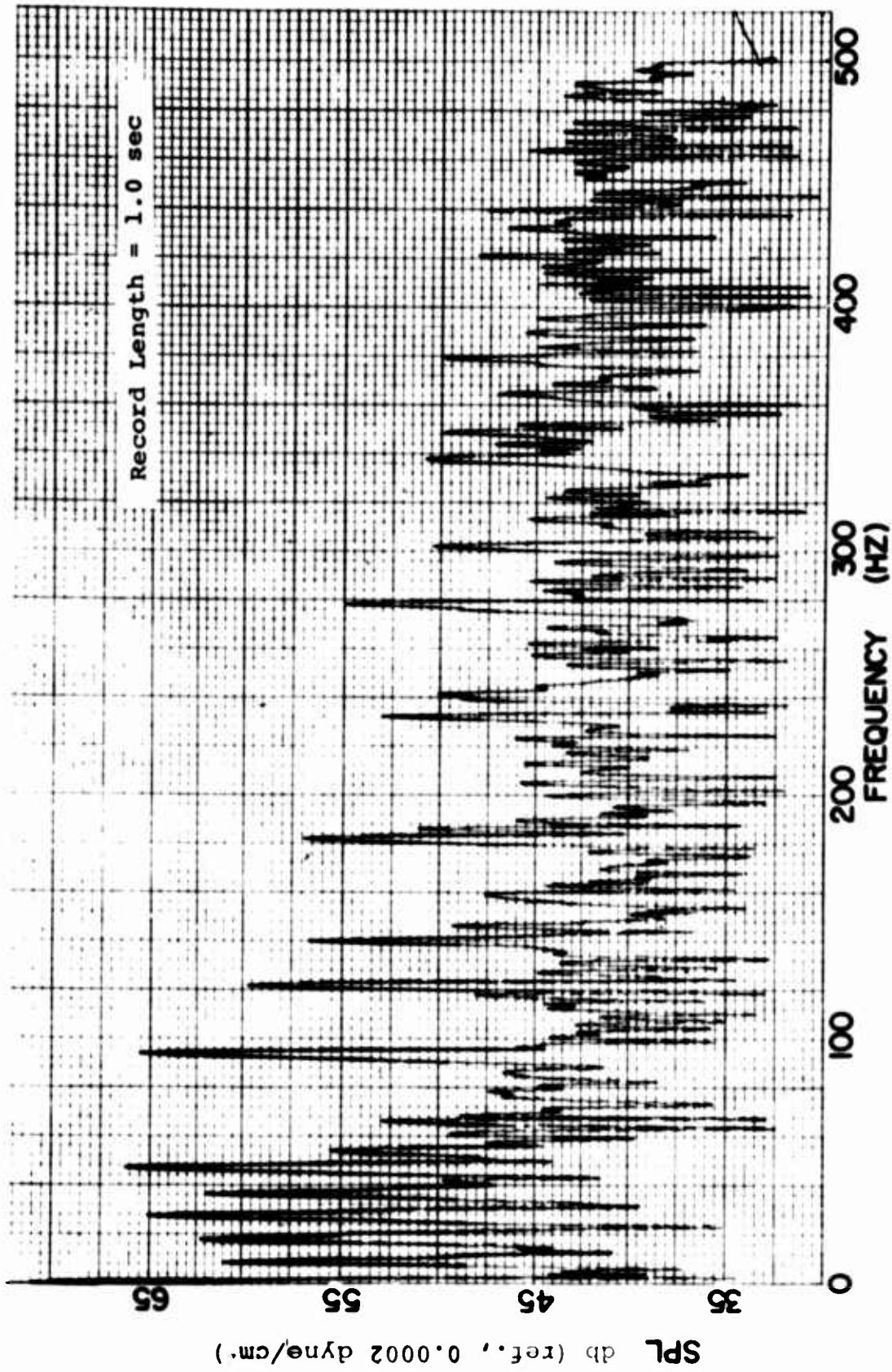


Figure 11. Noise Spectrum by Ubiquitous Analyzer for UH-1B Moving Away at 115 Knots Level Flight; Recorded at 200 ft to the Right.

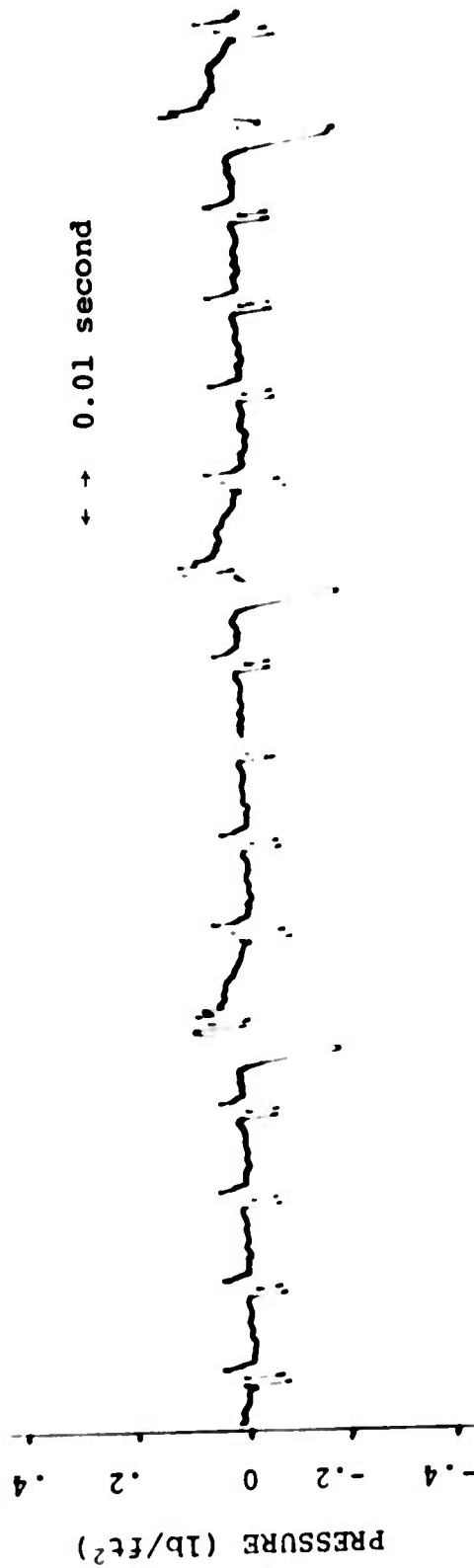


Figure 12. Oscillograph Recording of Pressure-Time History for UH-1B Approaching at 115 Knots Level Flight; Recorded at 200 ft to the Right.

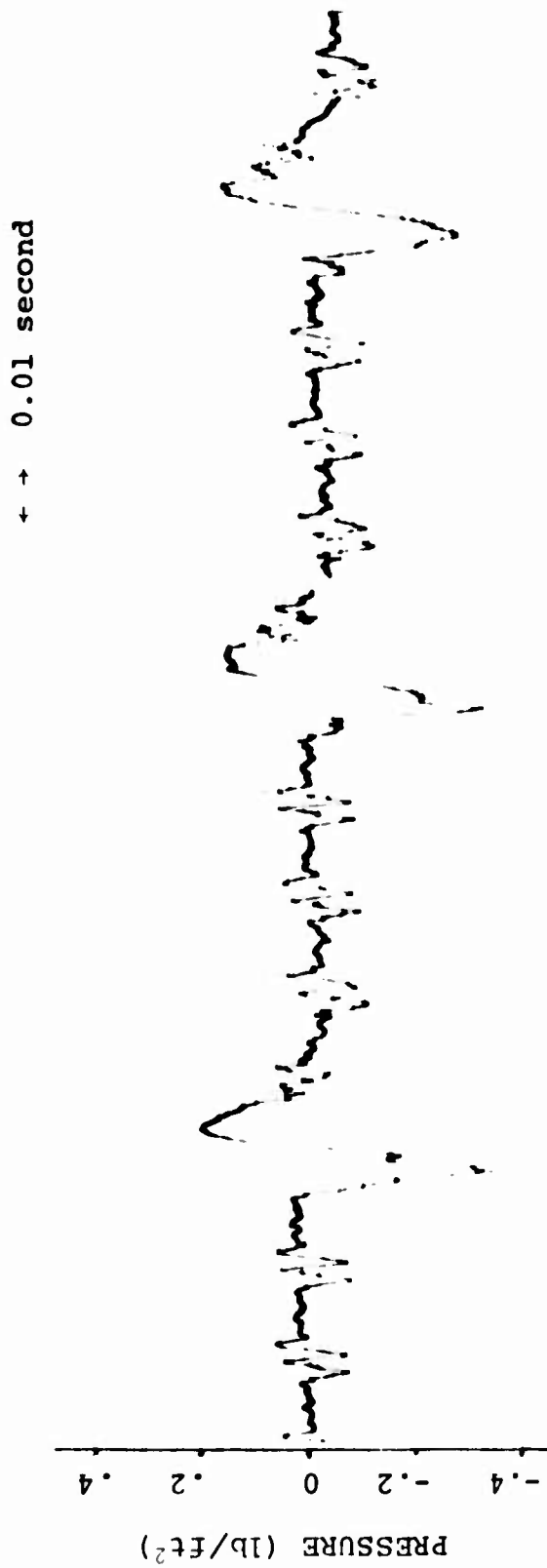


Figure 13. Oscillograph Recording of Pressure-Time History for UH-1B Approaching at 115 Knots Level Flight; Recorded at 200 ft to the Right.

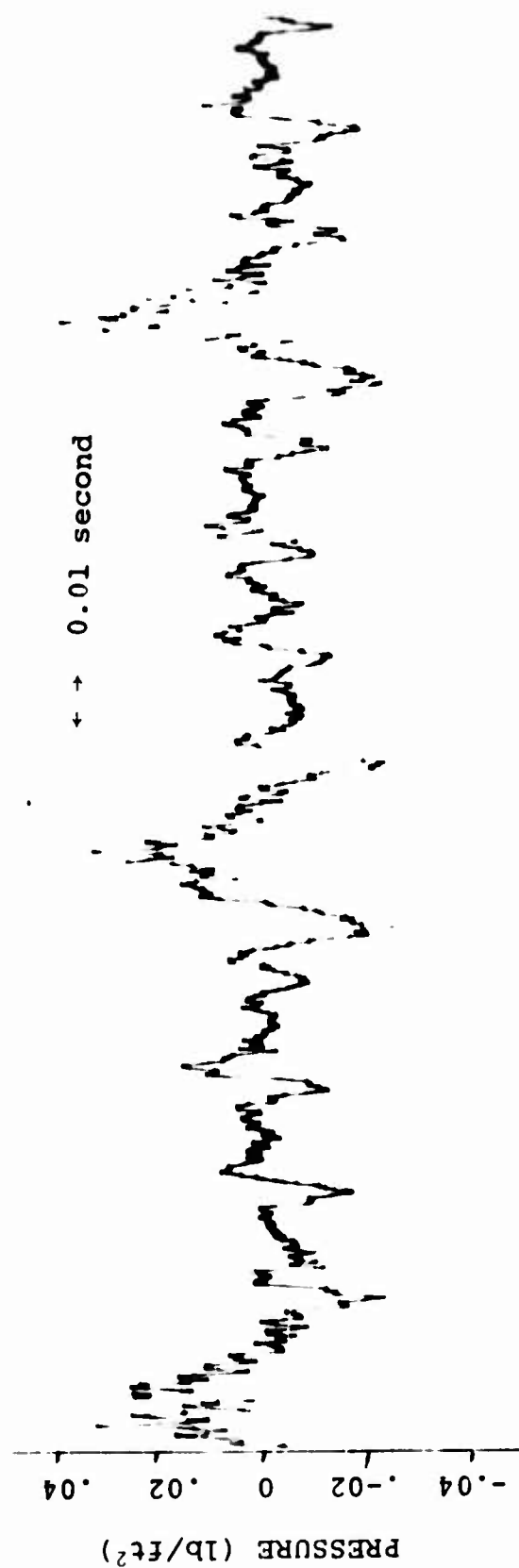


Figure 14. Oscillograph Recording of Pressure-Time History for UH-1B in 100 ft-Hover, Recorded at 700 ft to the Right.

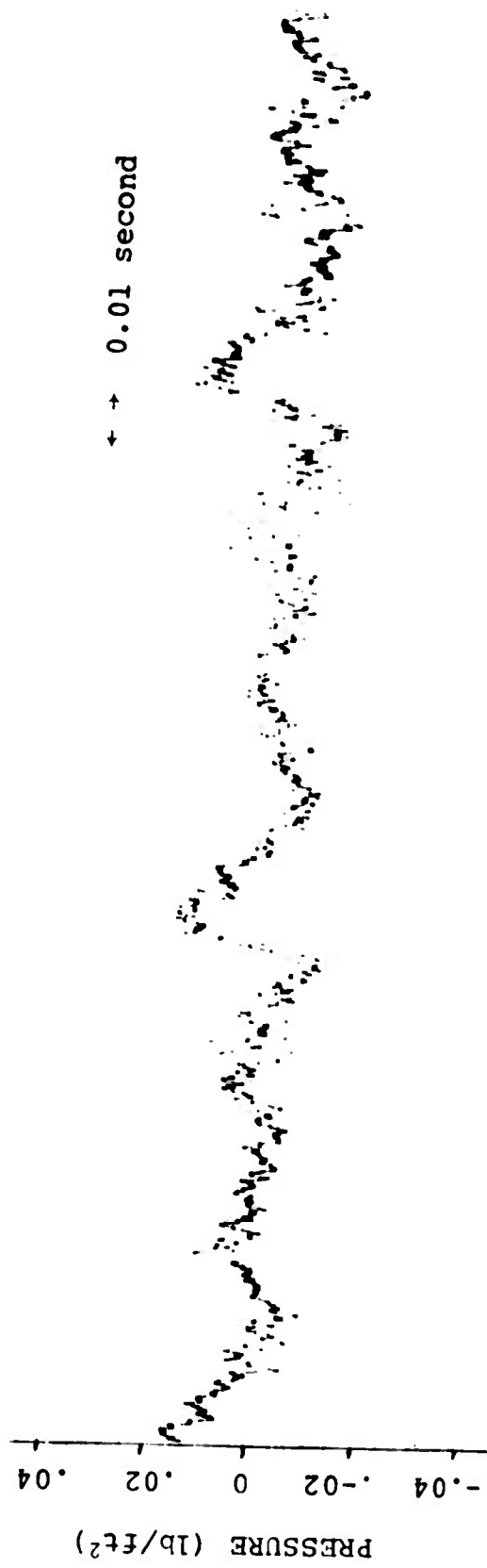


Figure 15. Oscillograph Recording of Pressure-Time History for UH-1B in 100 ft-Hover; Recorded at 700 ft to the Left.



Figure 16. Change in Character of Tail Rotor Noise During 115-Knot Level Flight Approach.

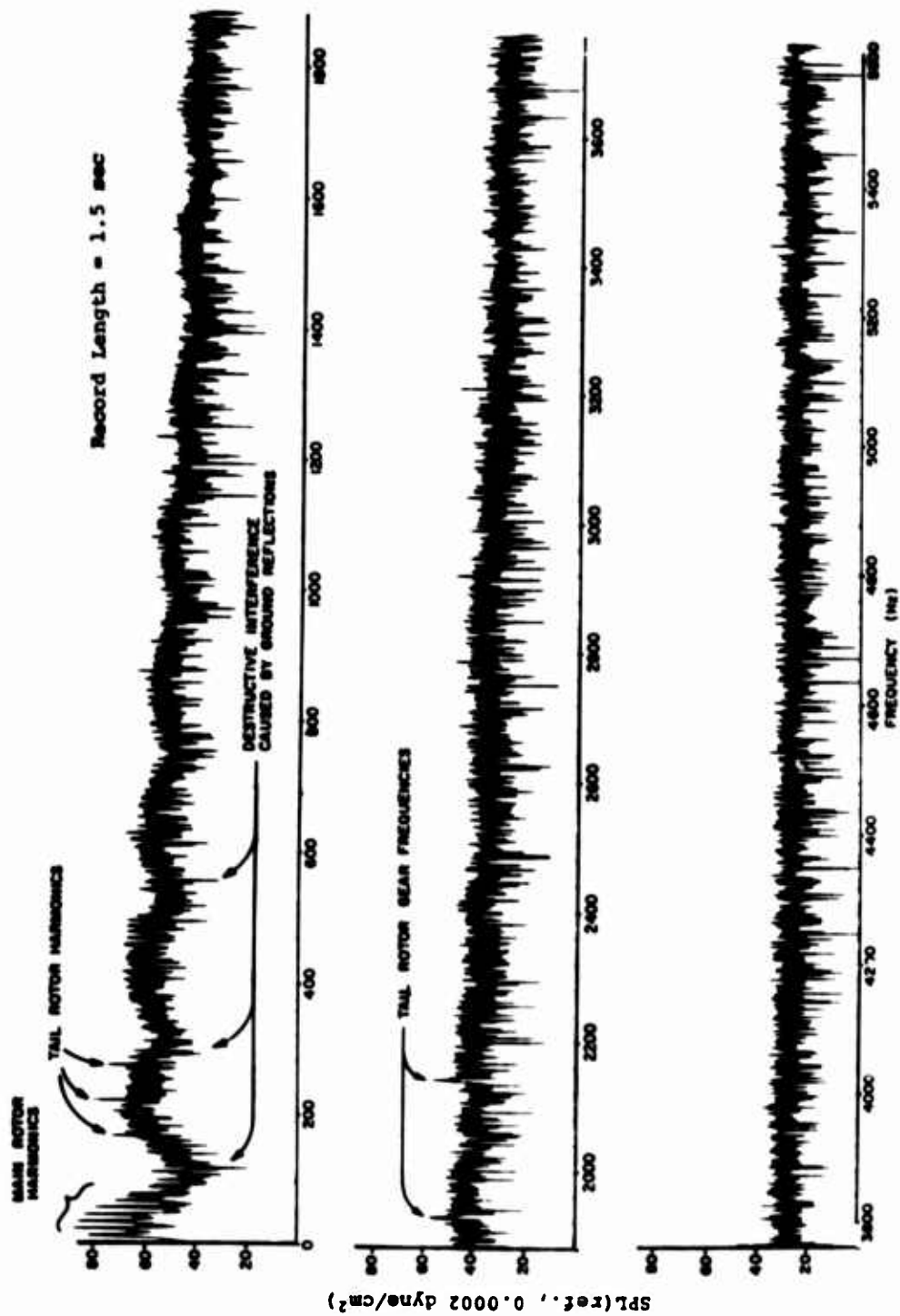


Figure 17. RASA Electronically Digitized Noise Spectrum for UH-1B in Hover; Recorded at 200 ft to the Right; Data Taken 26 Seconds Into Record.

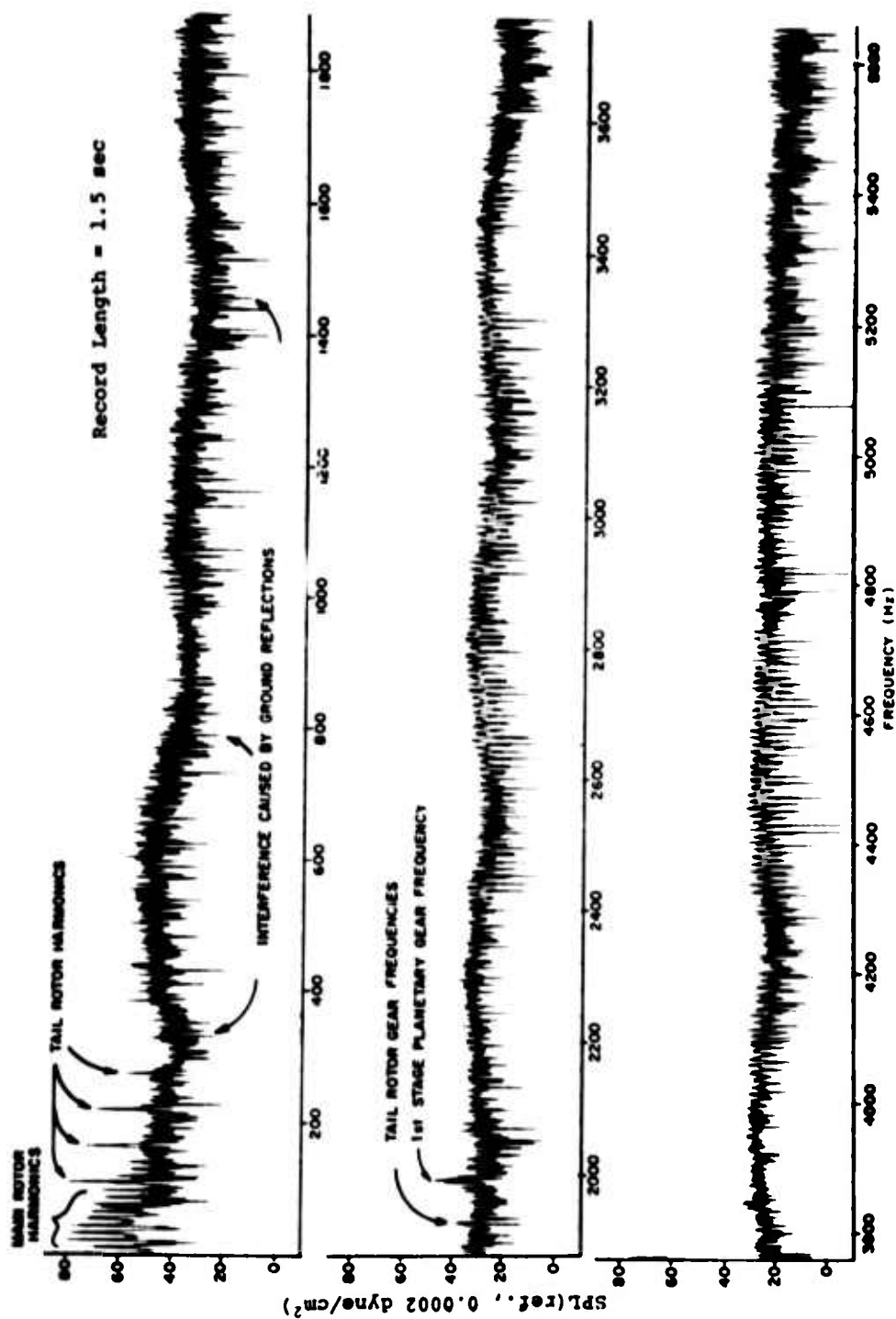


Figure 18. RASA Electronically Digitized Spectrum for UH-1B in 100 ft Hover; Recorded at 700 ft to the Right; Data Taken 26 Seconds Into Record.



Figure 19. Comparison of Oscillograph and Manually Digitized Pressure-Time Histories for UH-1B in 100-ft Hover; Recorded at 200 ft to the Right.

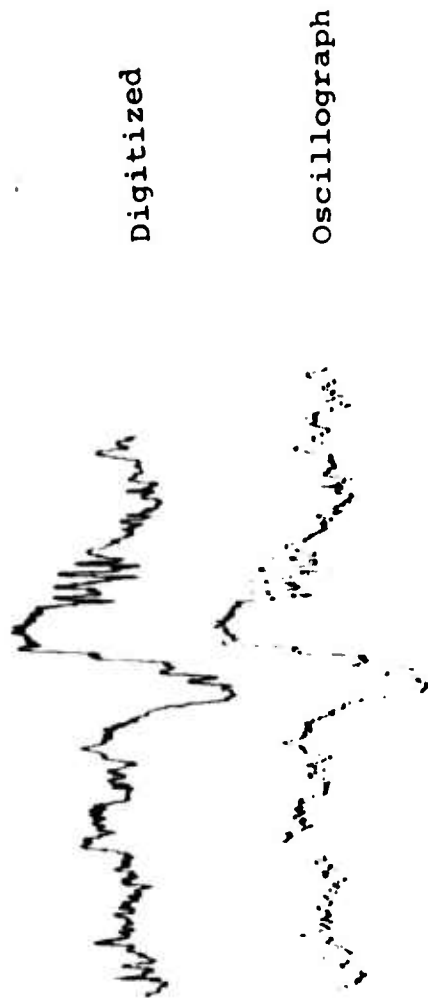


Figure 20. Comparison of Oscillograph and Electronically Digitized Pressure-Time Histories for UH-1B in 115-Knot Flyby; Recorded at 200 ft to the Right.

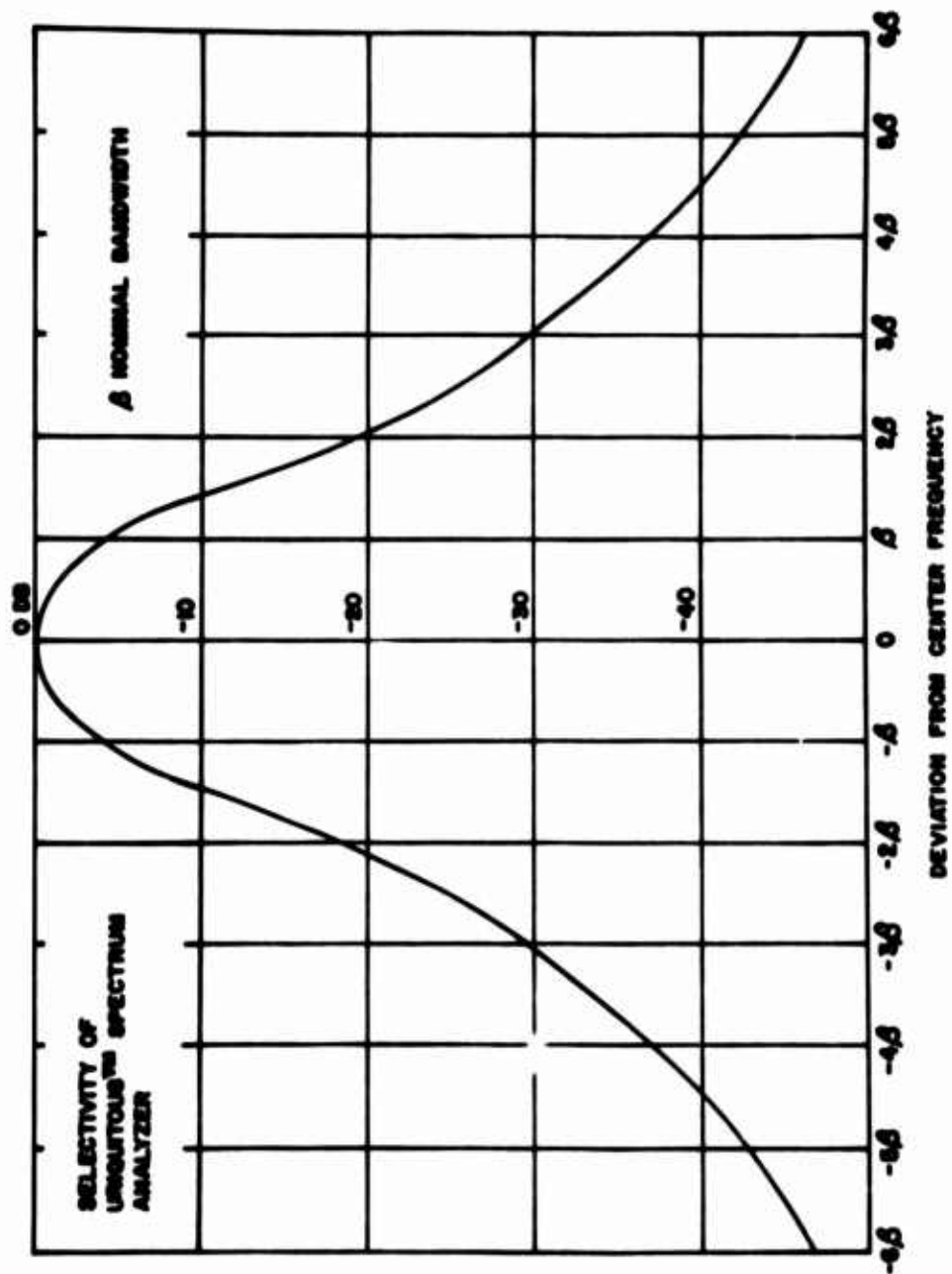


Figure 21. Filter Characteristics for Ubiquitous Analyzer.

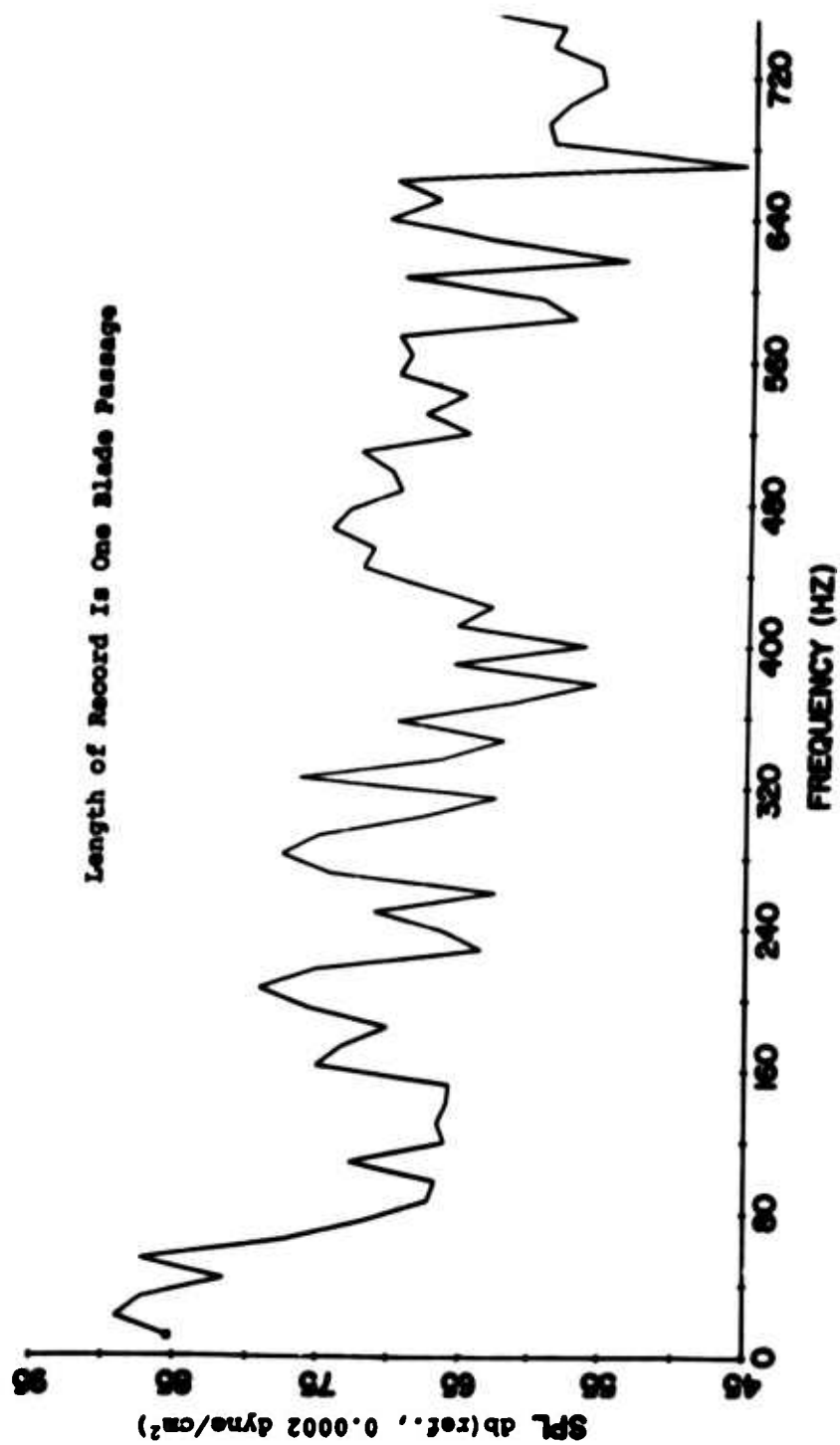


Figure 22. Analytically Determined Noise Spectrum at Position 4 for UH-1B in Hover; Filter Bandwidth Is Unfiltered.

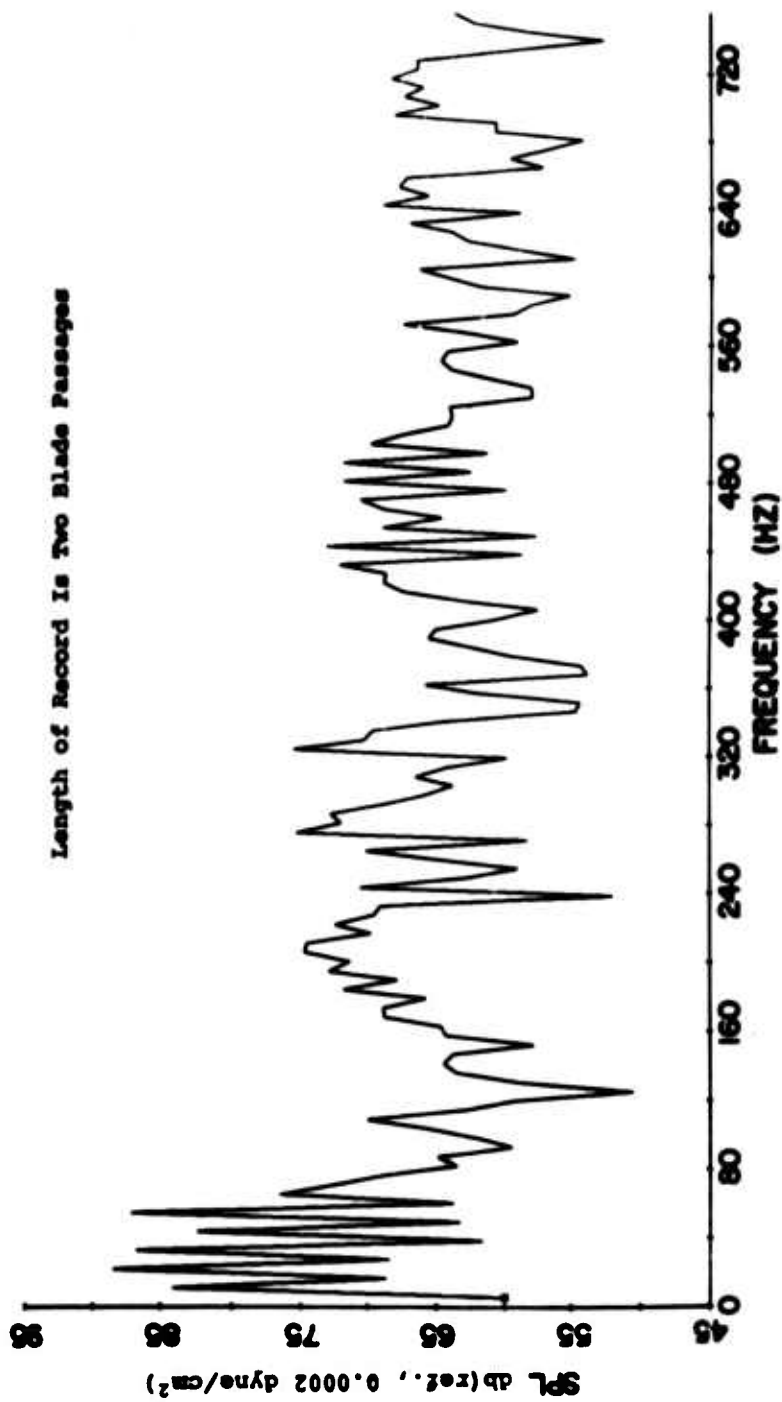


Figure 23. Analytically Determined Noise Spectrum at Position 4 for UH-1B in Hover; Filter Bandwidth Is Unfiltered.

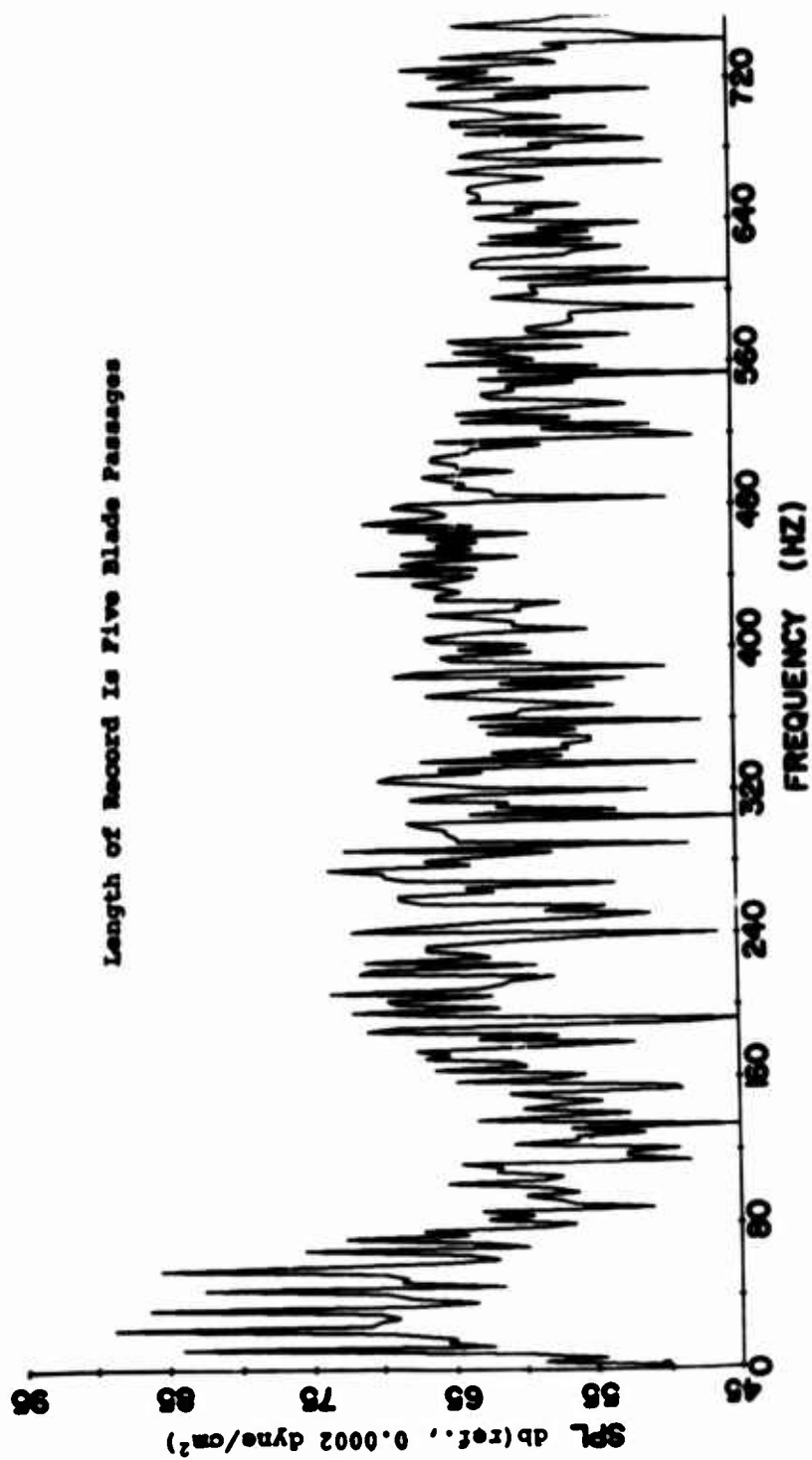


Figure 24. Analytically Determined Noise Spectrum at Position 4 for UH-1B in Hover; Filter Bandwidth Is Unfiltered.

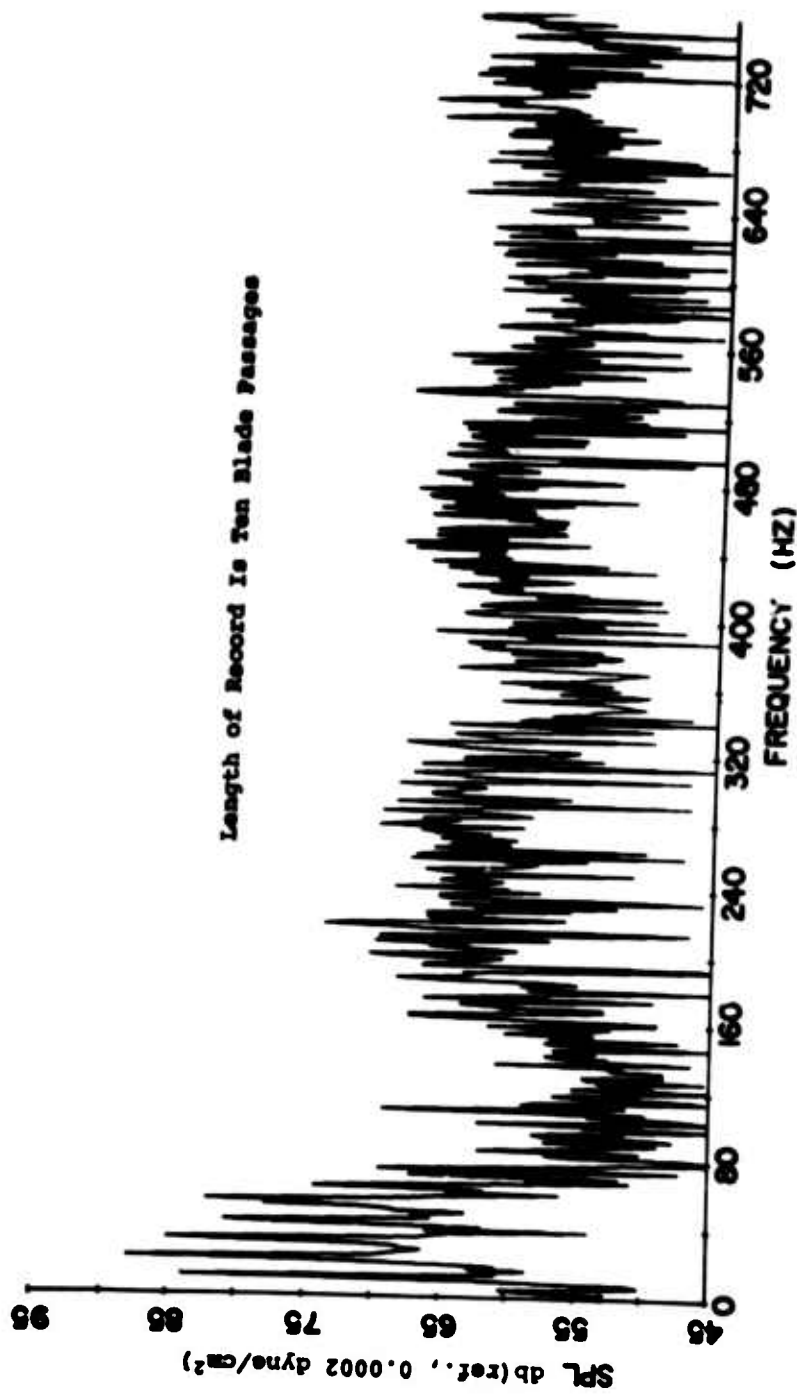


Figure 25. Analytically Determined Noise Spectrum at Position 4 for UH-1B in Hover; Filter Bandwidth Is Unfiltered.

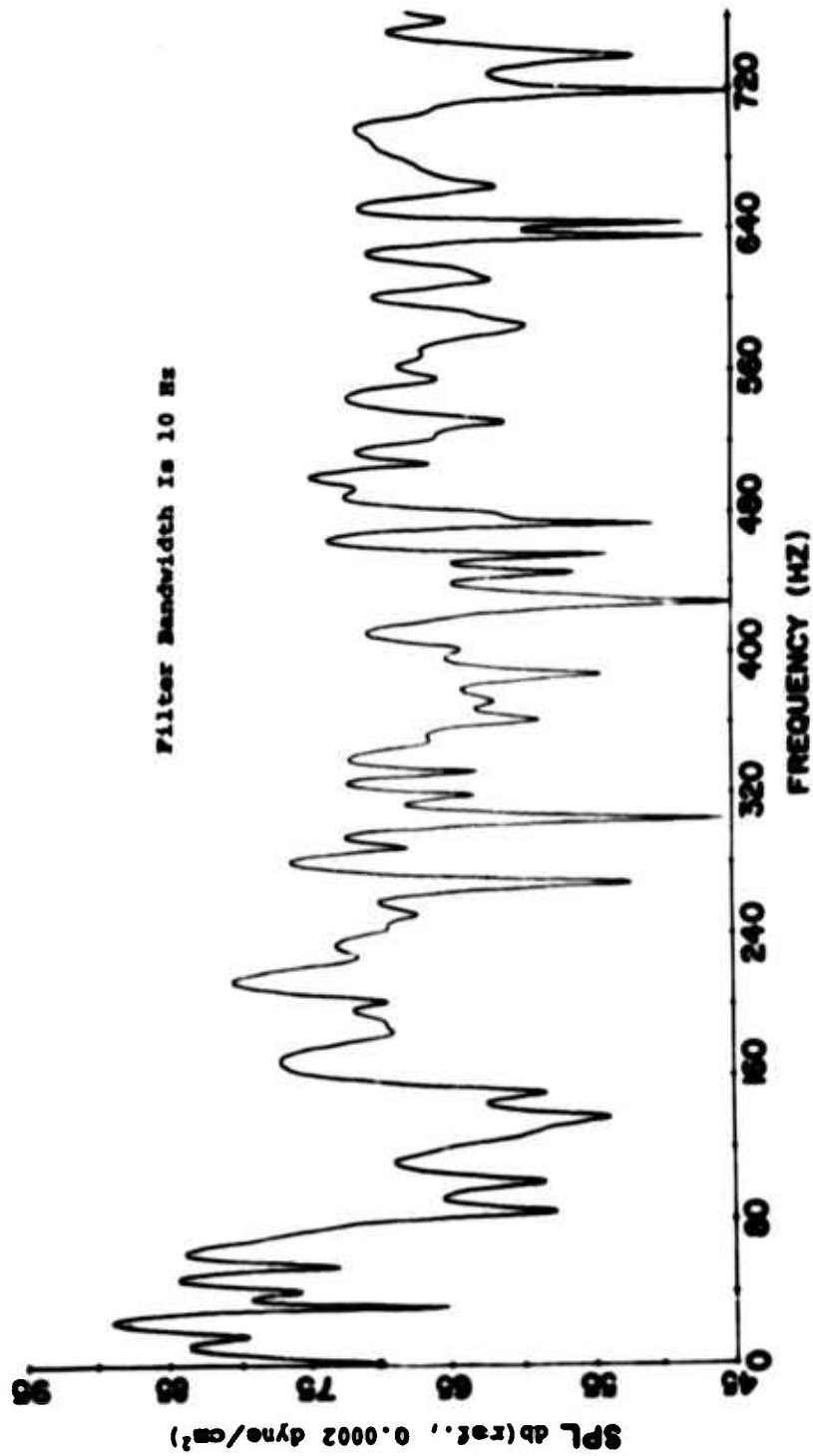


Figure 26. Analytically Determined Noise Spectrum at Position 4 for UH-1B in Hover; Length of Record Is Ten Blade Passages.

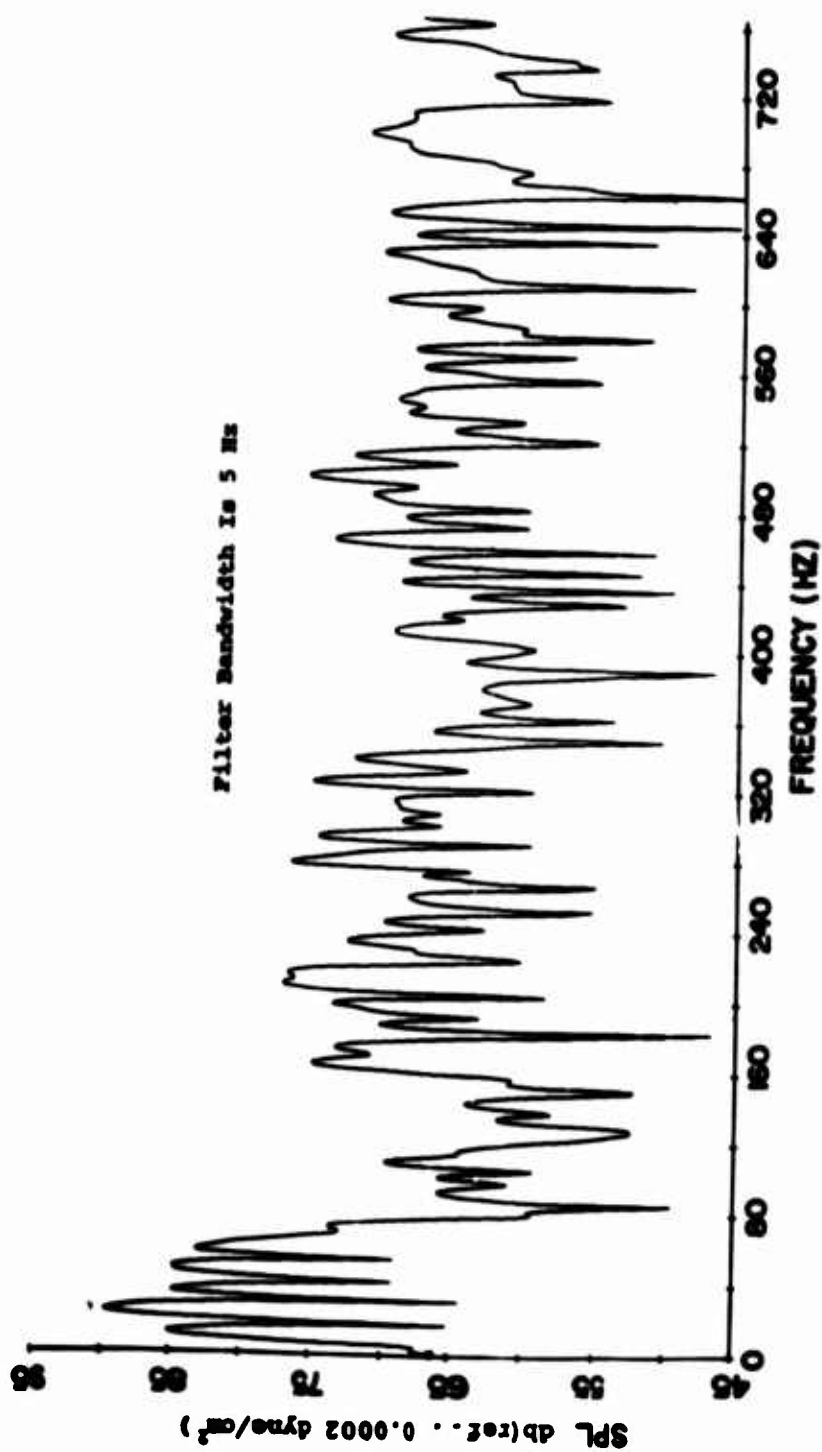


Figure 27. Analytically Determined Noise Spectrum at Position 4 for UH-1B in Hover; Length of Record Is Ten Blade Passages.

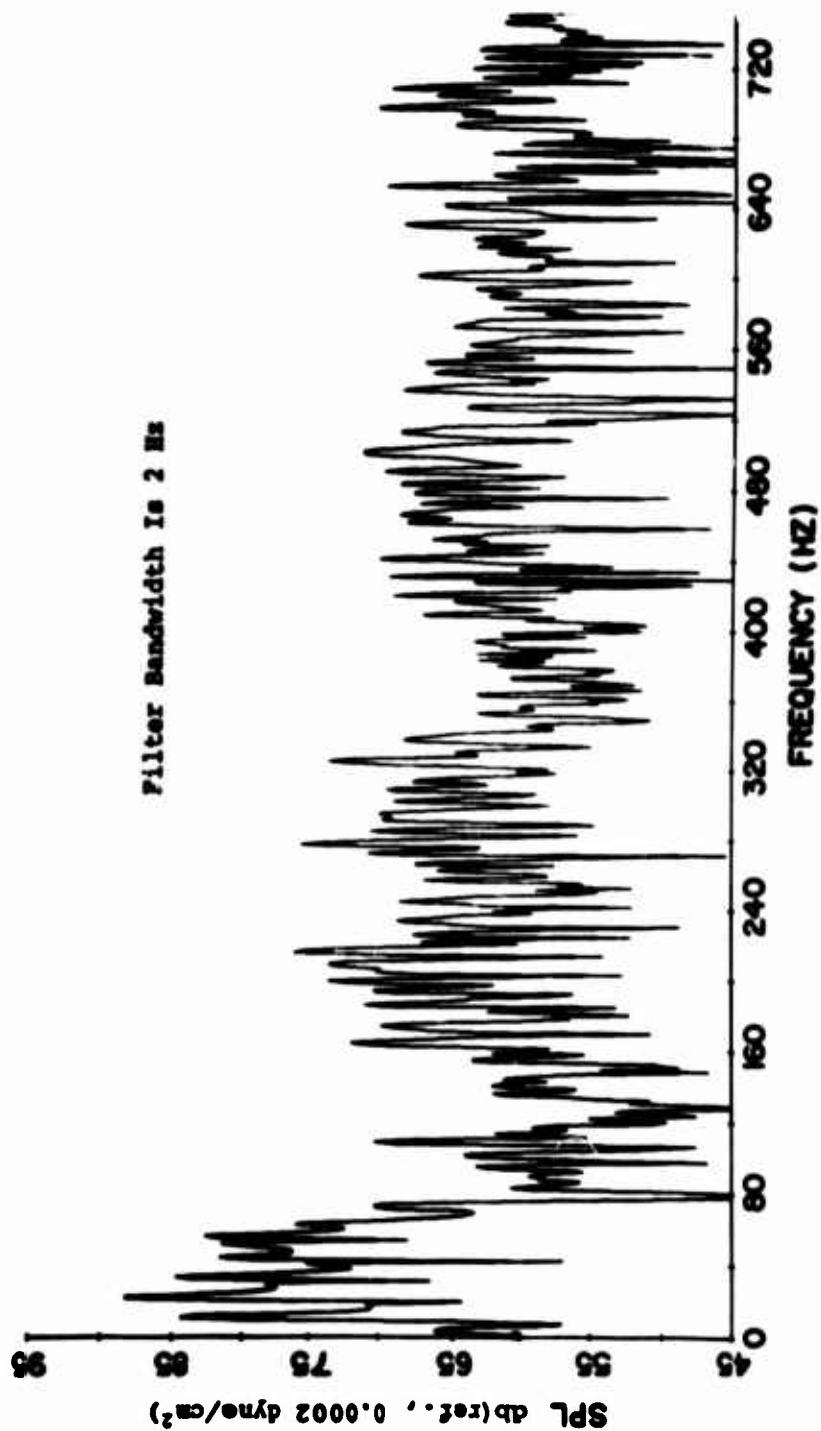


Figure 28. Analytically Determined Noise Spectrum at Position 4 for UH-1B in Hover; Length of Record Is Ten Blade Passages.

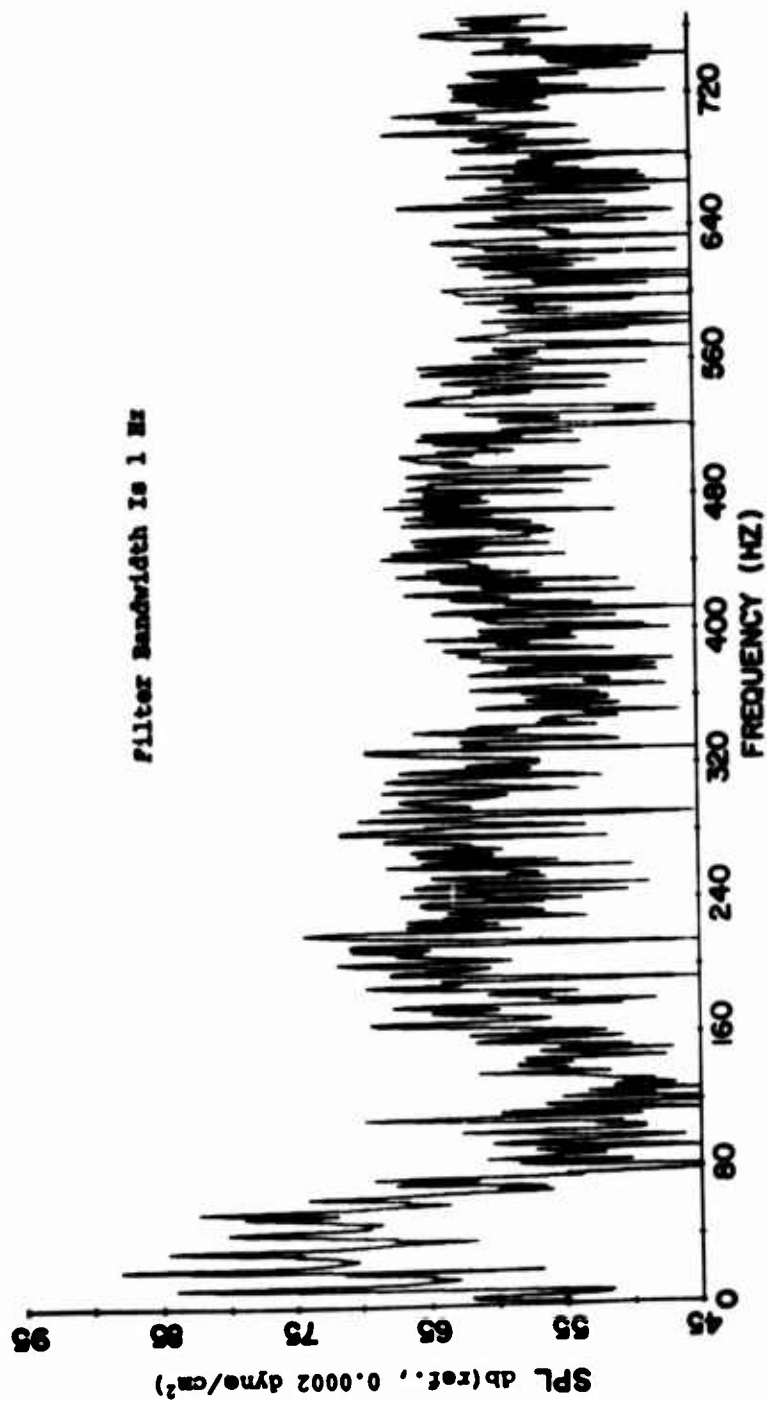


Figure 29. Analytically Determined Noise Spectrum at Position 4 for UH-1B in Hover; Length of Record Is Ten Blade Passages.

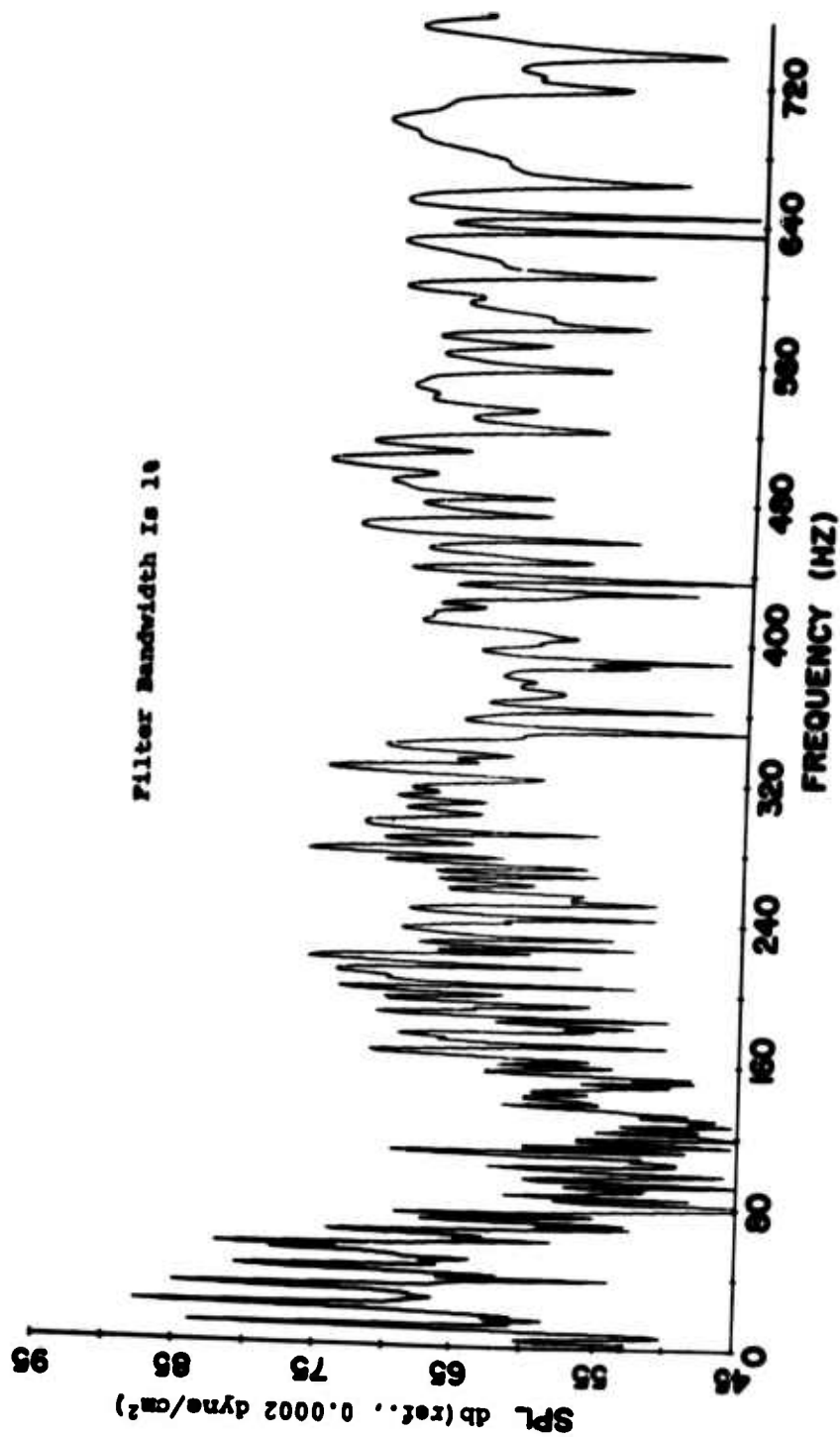


Figure 30. Analytically Determined Noise Spectrum at Position 4 for UH-1B in Hover; Length of Record Is Ten Blade Passages.

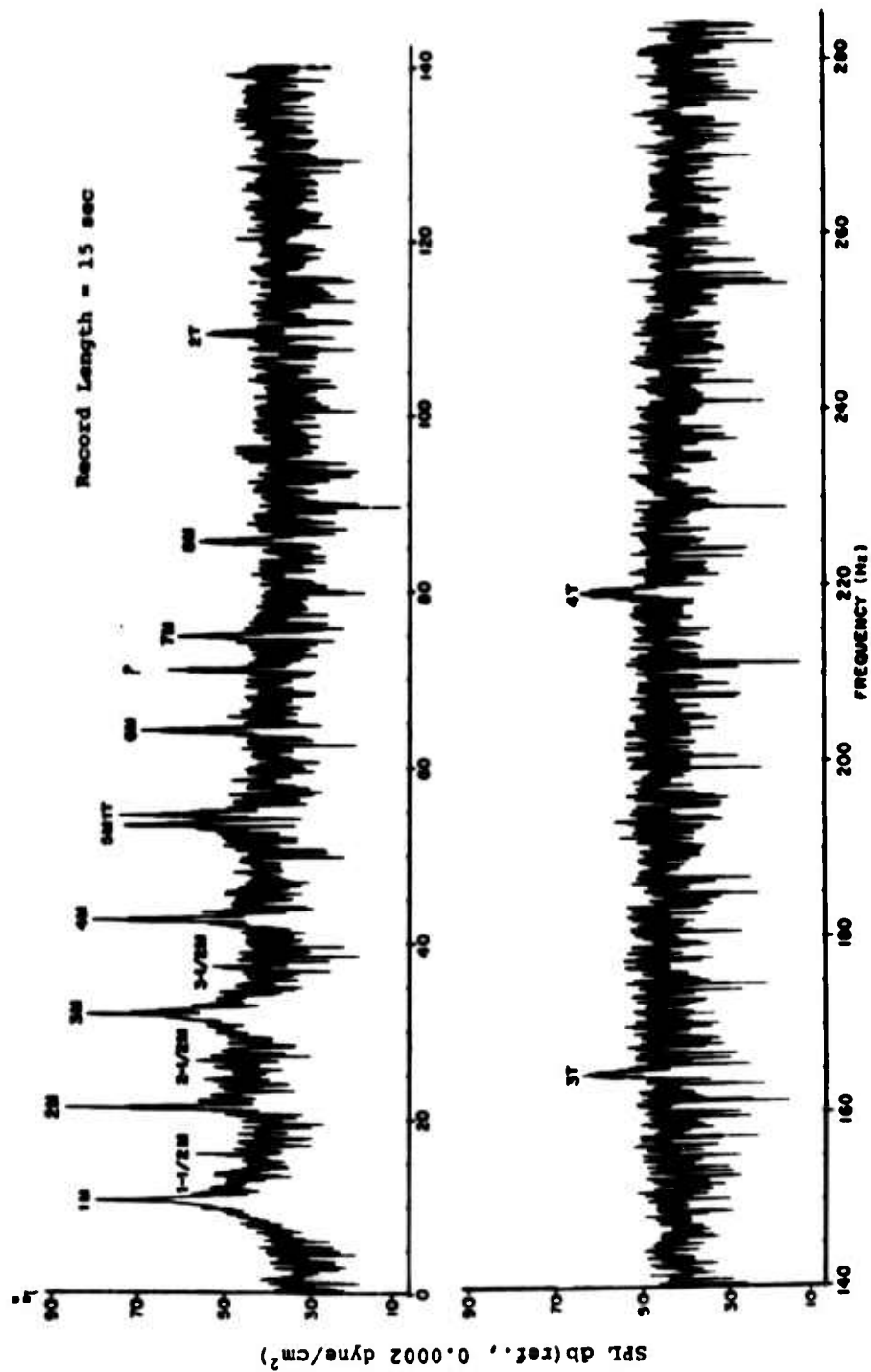


Figure 31. RASA Electronically Digitized Noise Spectrum at Position 4 for UH-1B in Hover.

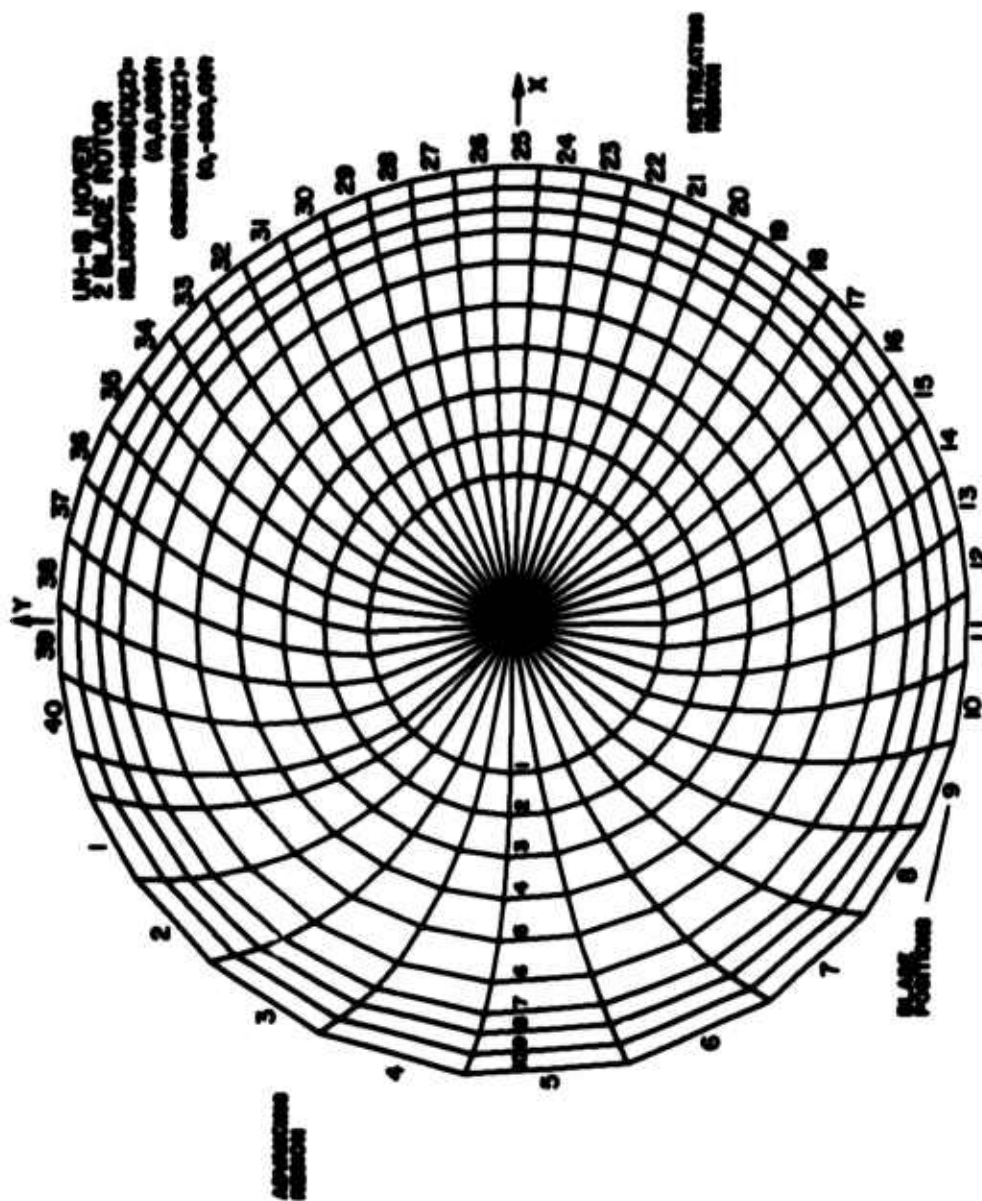


Figure 32. Retarded Time Diagram for Hover Showing Locations of Blade Radial and Azimuthal Stations.

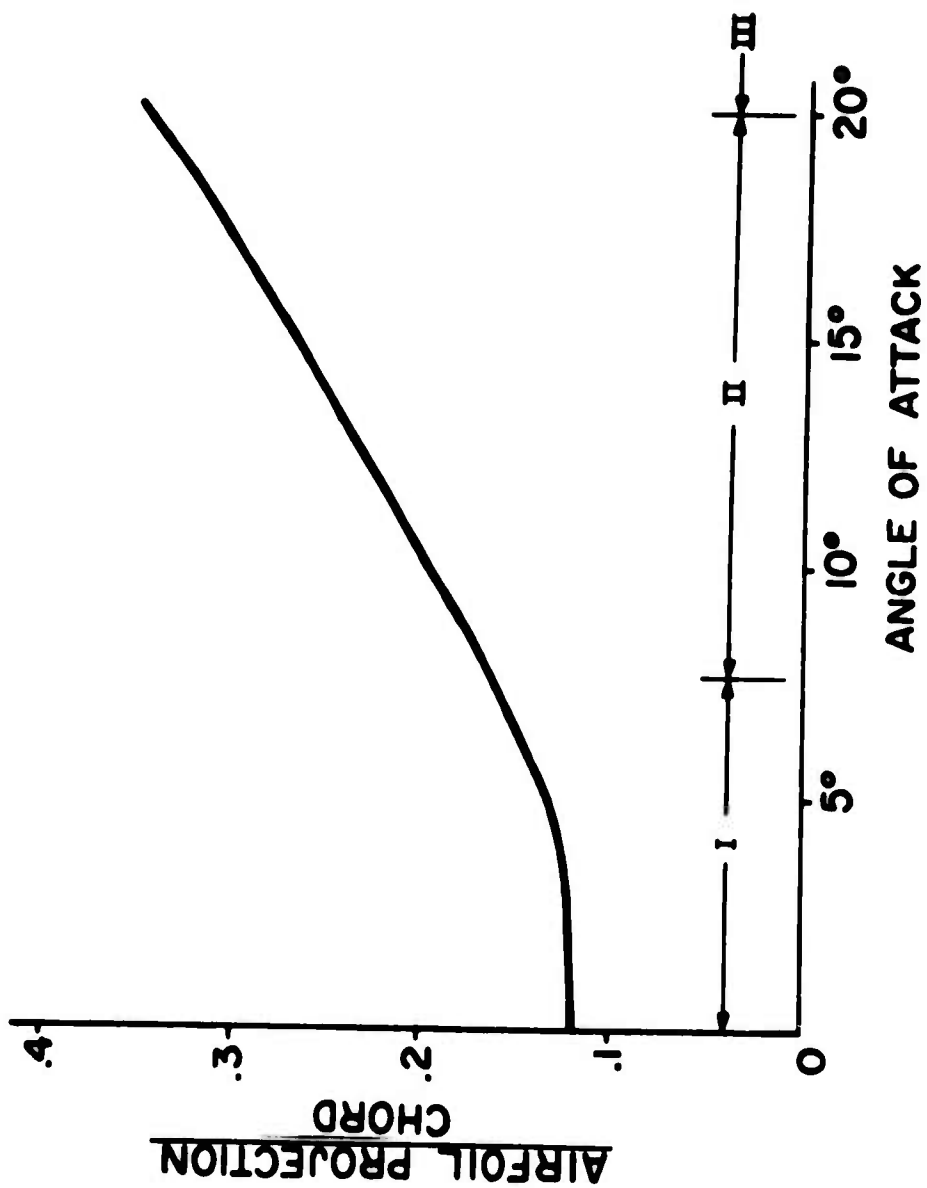


Figure 33. Projected Airfoil Dimension as a Function of Angle of Attack.

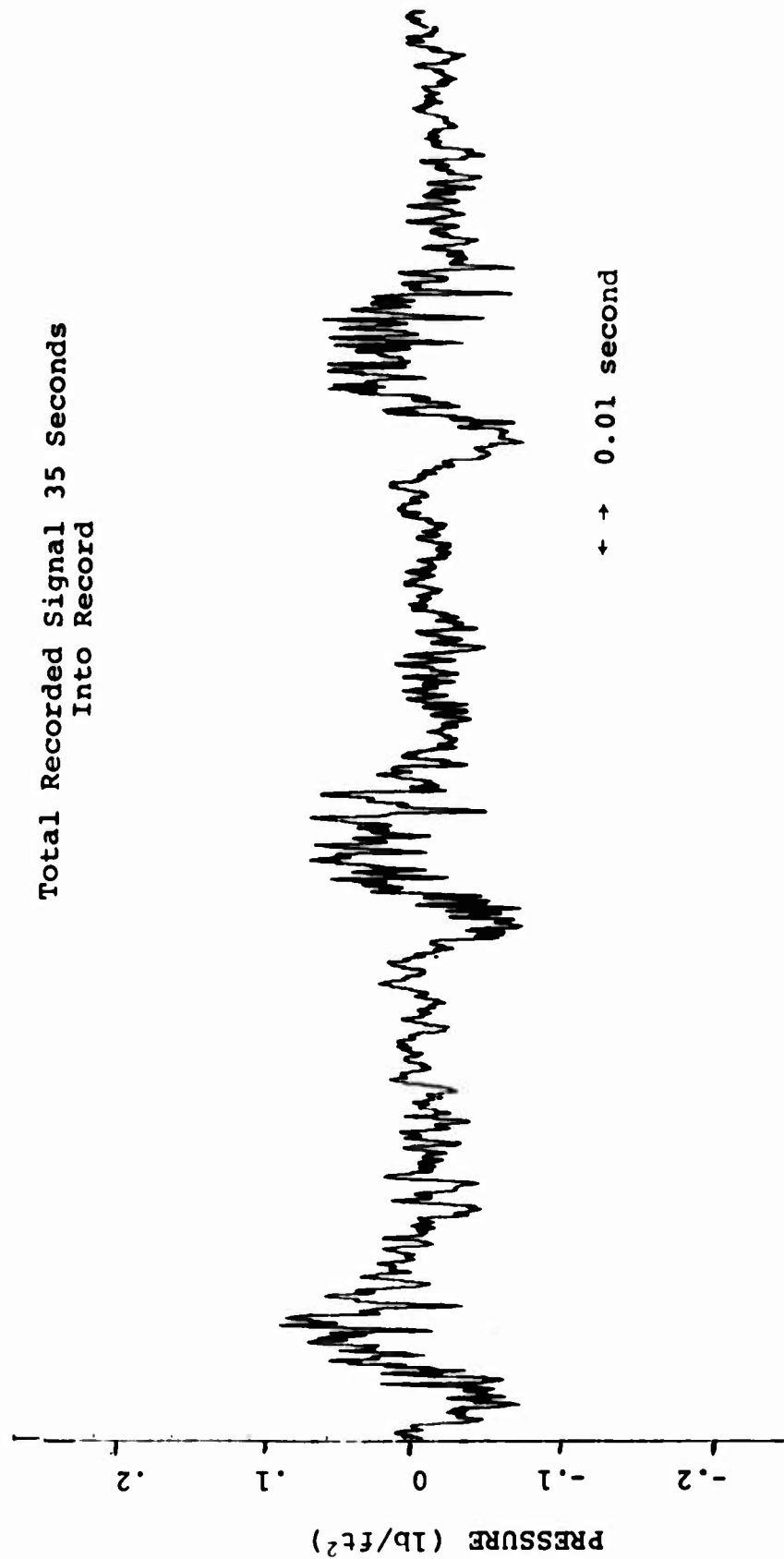


Figure 34. RASA Electronically Digitized Pressure-Time History  
at Position 4 for UH-1B in Hover.

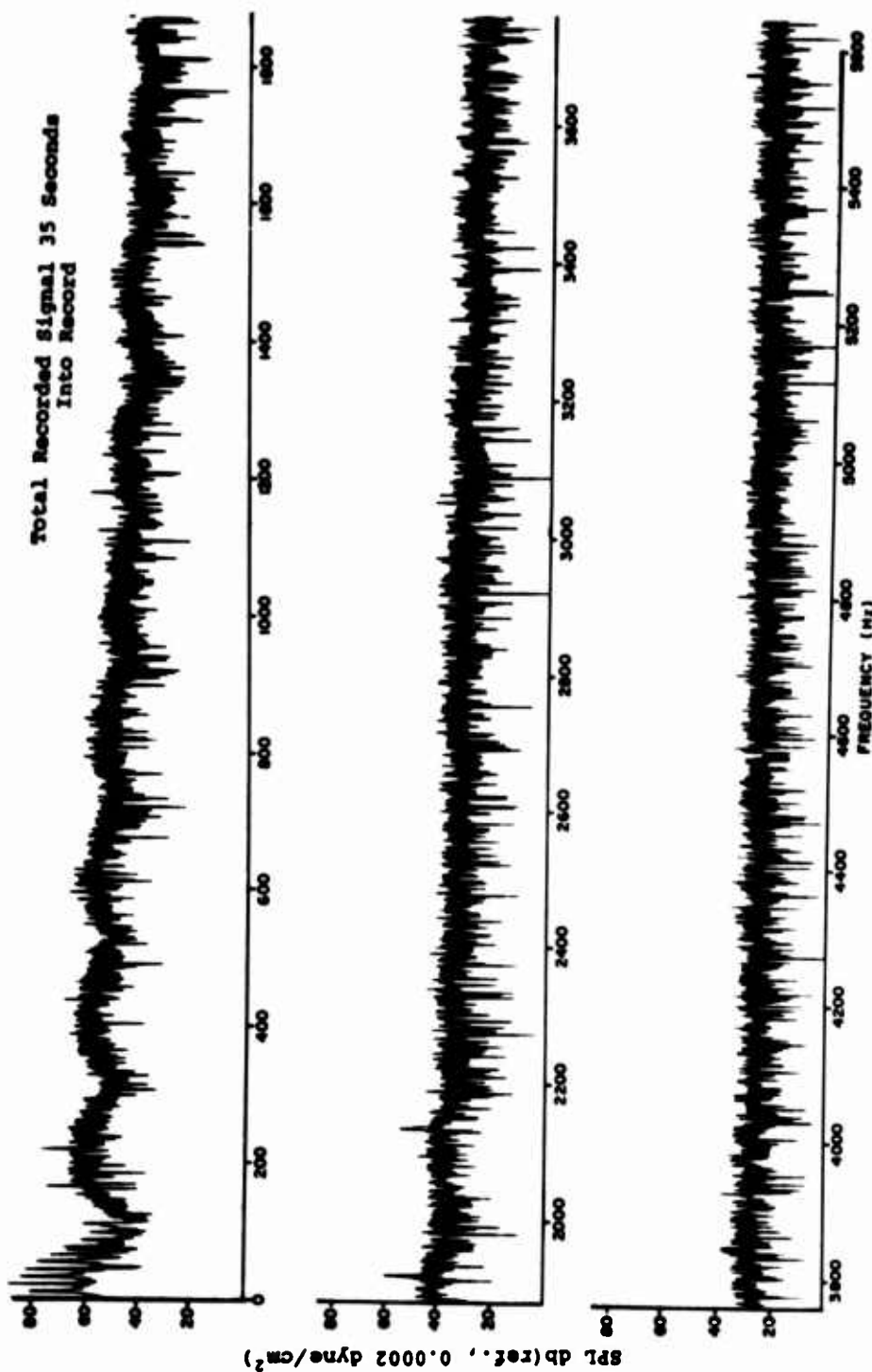


Figure 35. RASA Electronically Digitized Noise Spectrum at Position 4 for UH-1B in Hover.

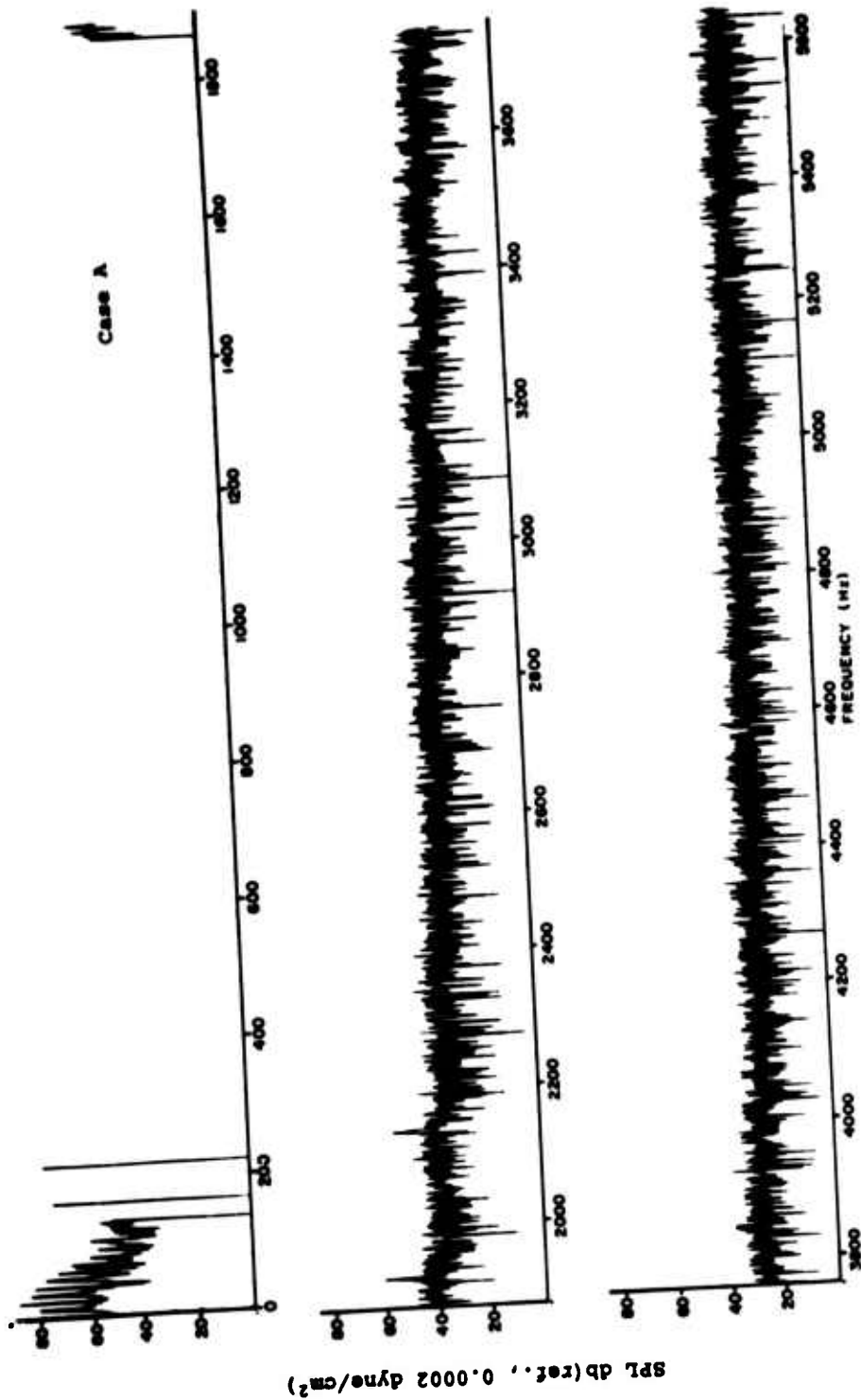


Figure 36. RASA Electronically Digitized Noise Spectrum at Position 4 for UH-1B in Hover (Vortex Noise Removed).

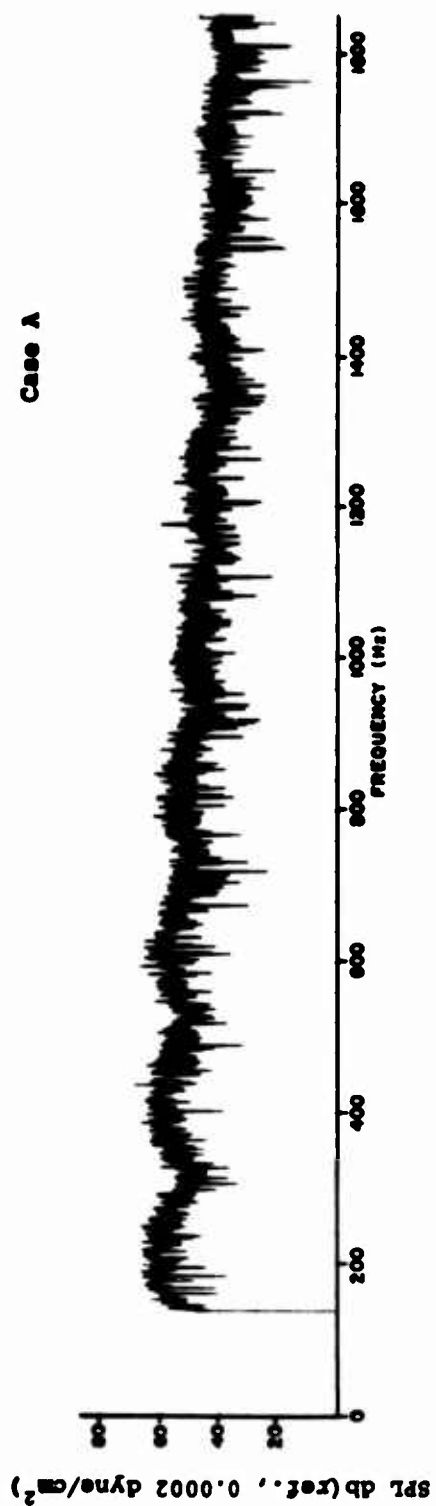


Figure 37. RASA Electronically Digitized Spectrum of Vortex Noise for UH-1B in Hover.

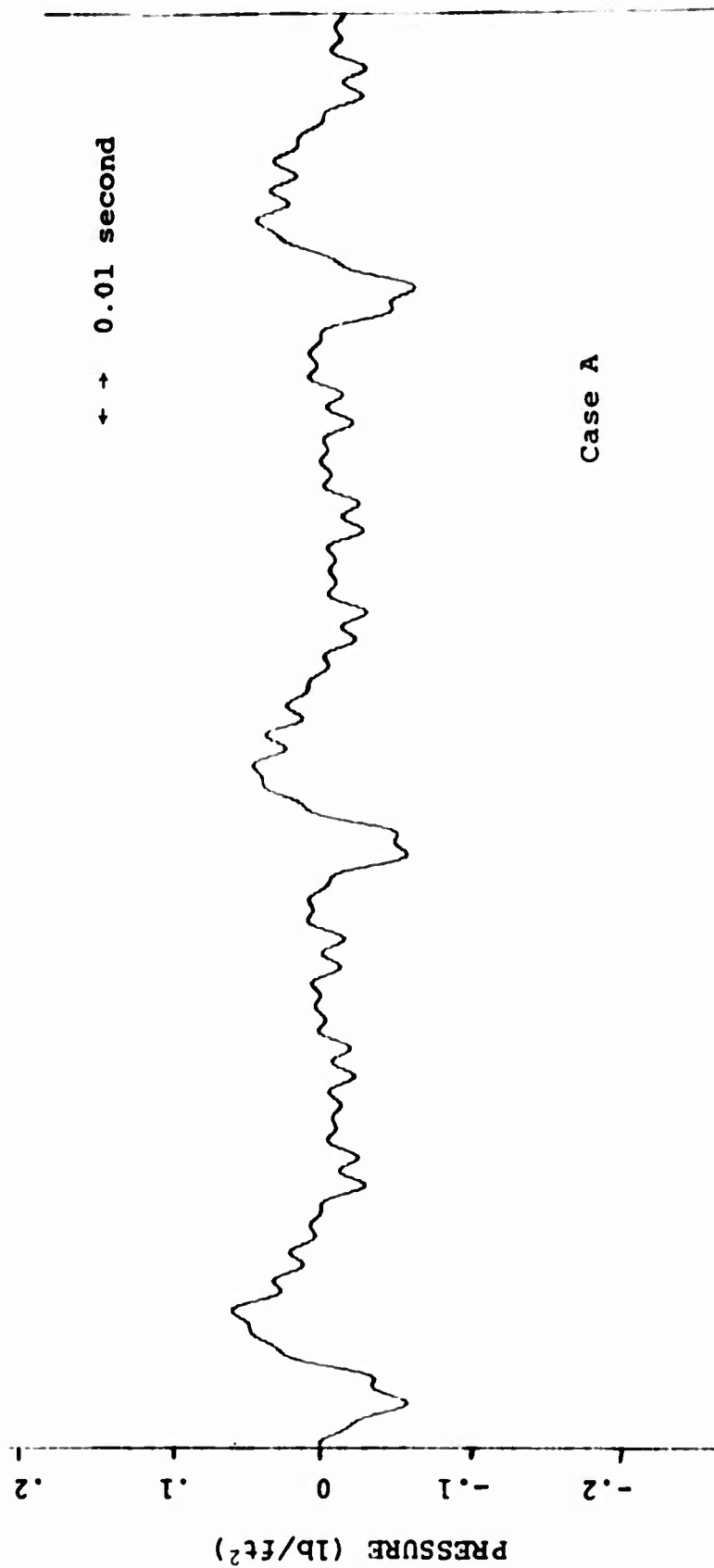


Figure 38. RASA Electronically Digitized Pressure-Time History of Rotational and Gear-Clash Noise for UH-1B in Hover.

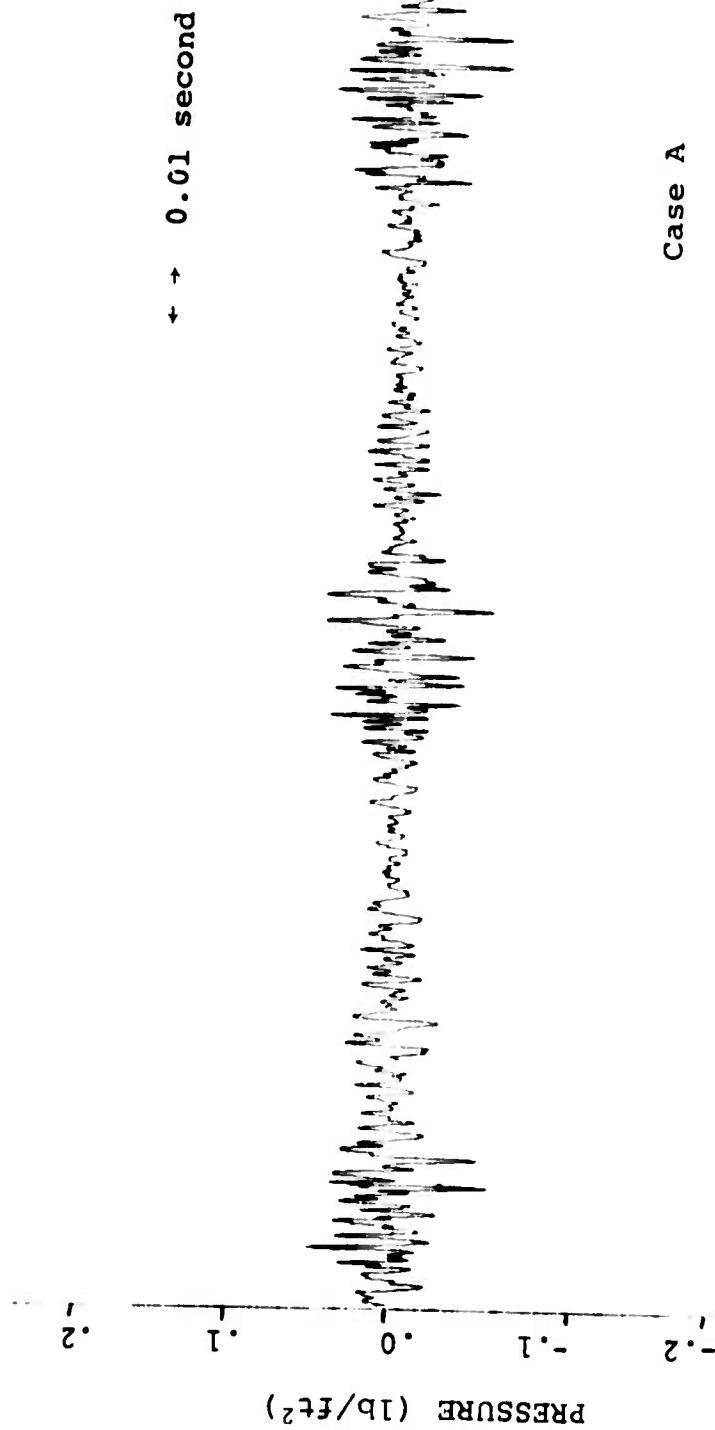


Figure 39. RASA Electronically Digitized Pressure-Time History of Vortex Noise for UH-1B in Hover.

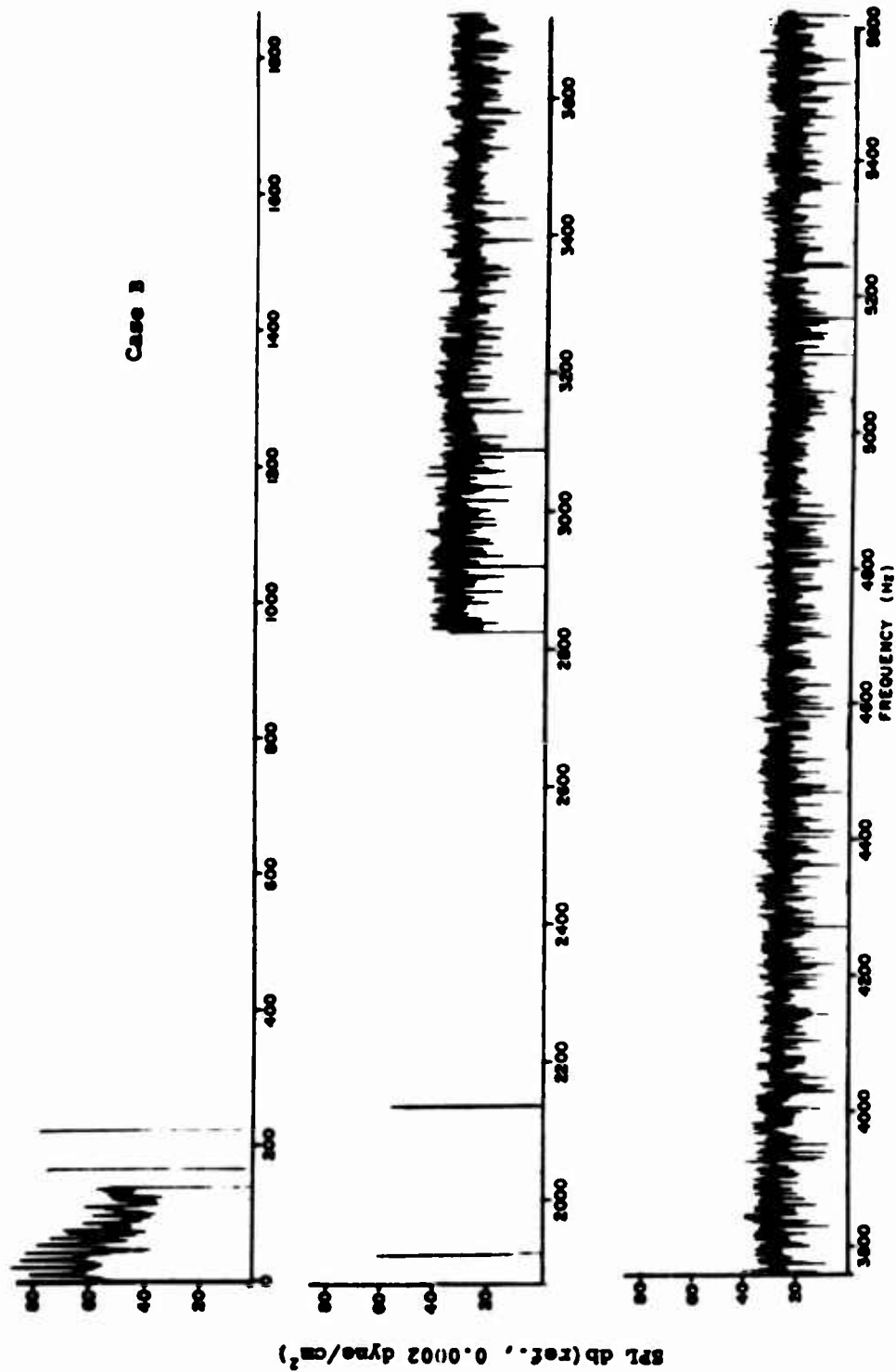


Figure 40. RASA Electronically Digitized Noise Spectrum at Position 4 for UH-1B in Hover (Vortex Noise Removed).

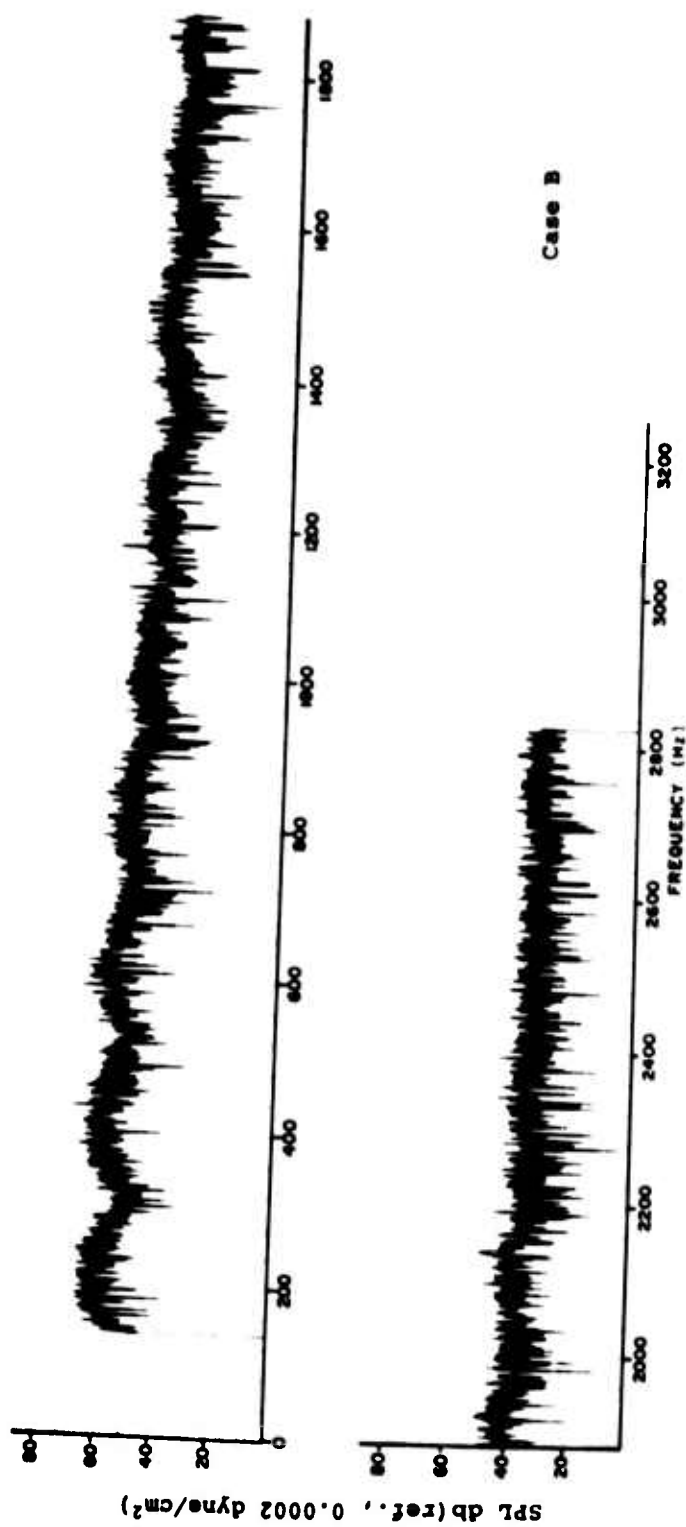


Figure 41. PASA Electronically Digitized Noise Spectrum of Vortex Noise at Position 4 for UH-1B in Hover.

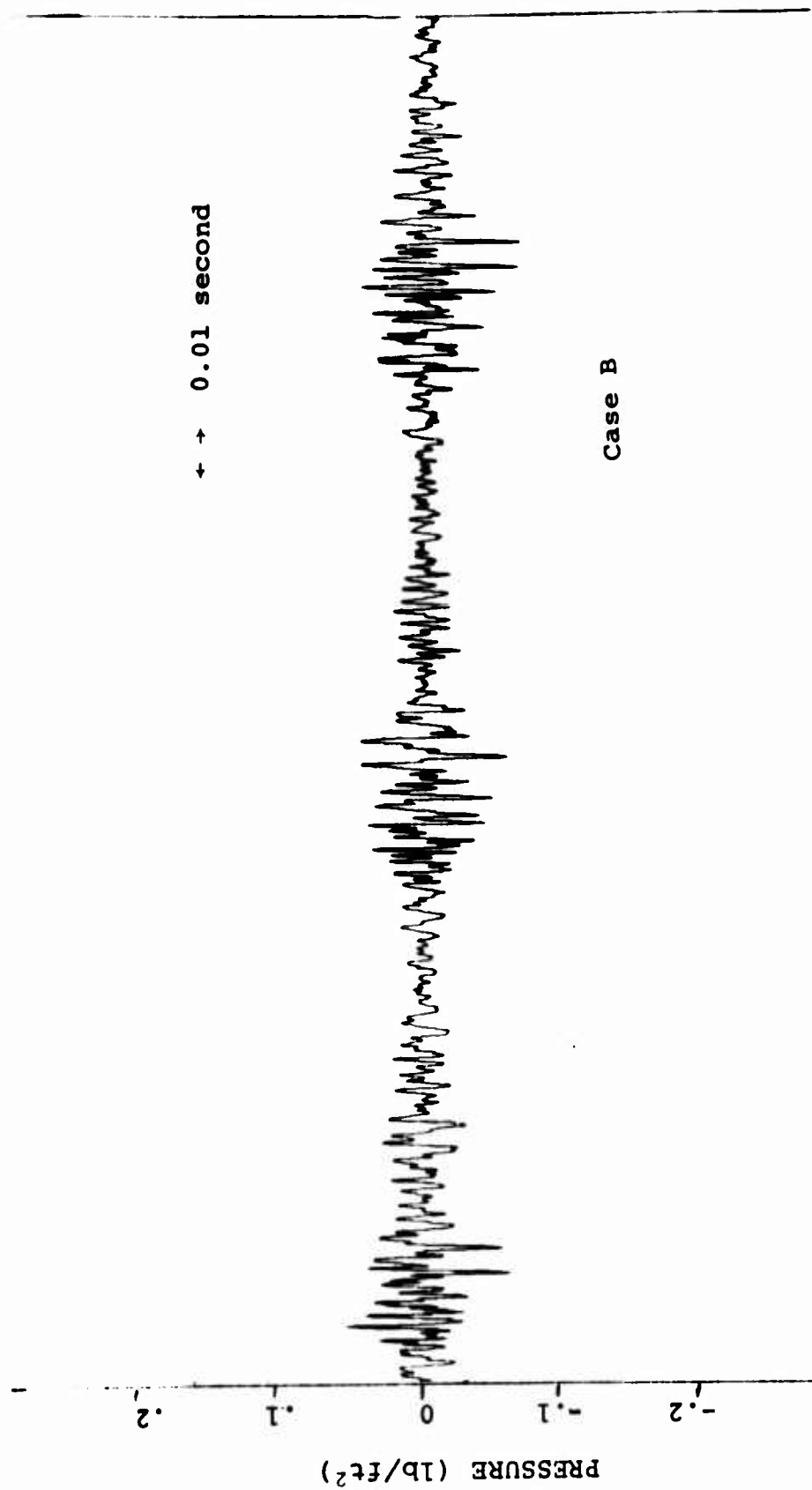


Figure 42. RASA Electronically Digitized Pressure-Time History of Vortex Noise at Position 4 for UH-1B in Hover.

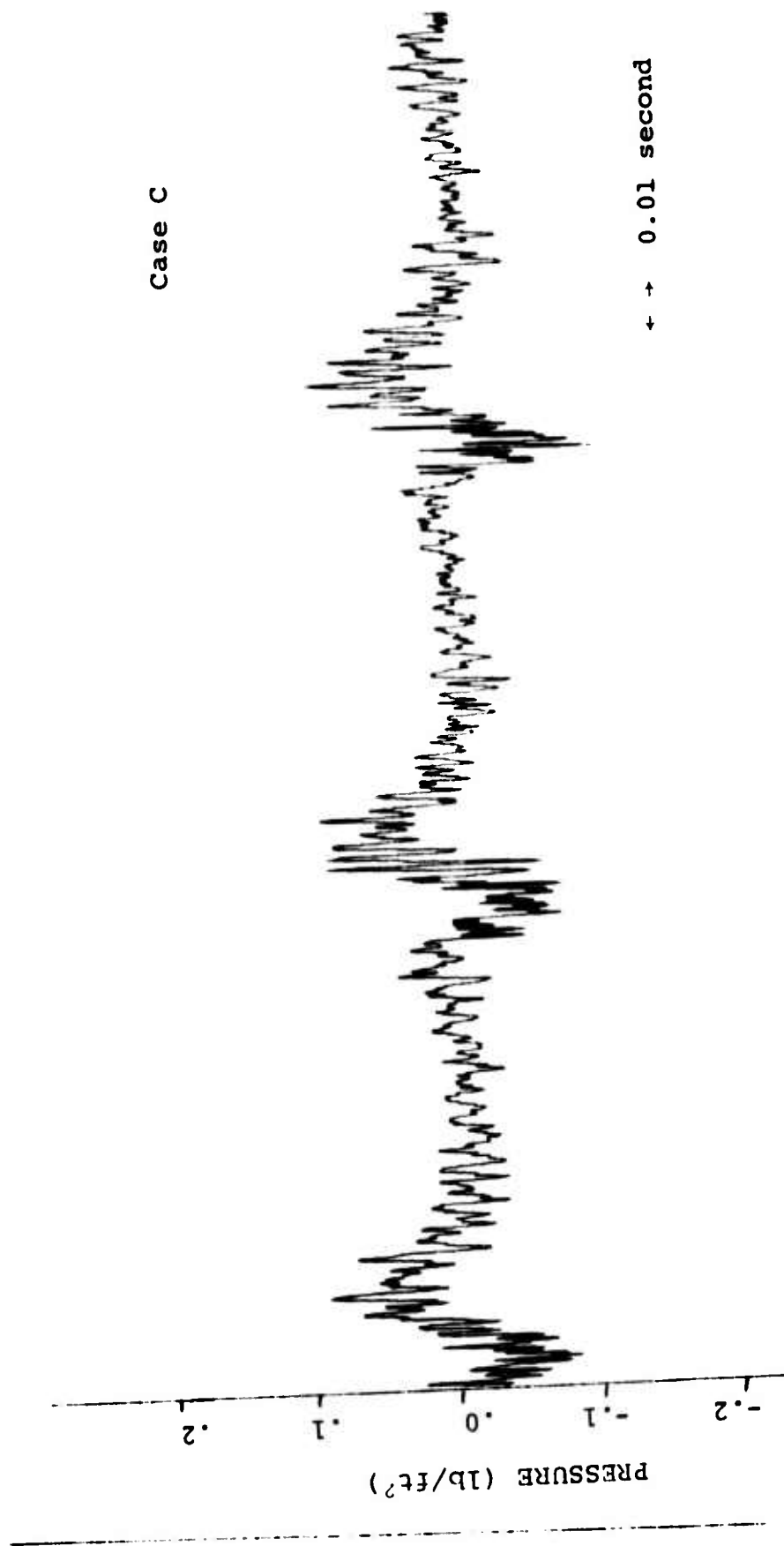


Figure 43. RASA Electronically Digitized Pressure-Time History of Total Recorded Signal at Position 4 for UH-1B in Hover.

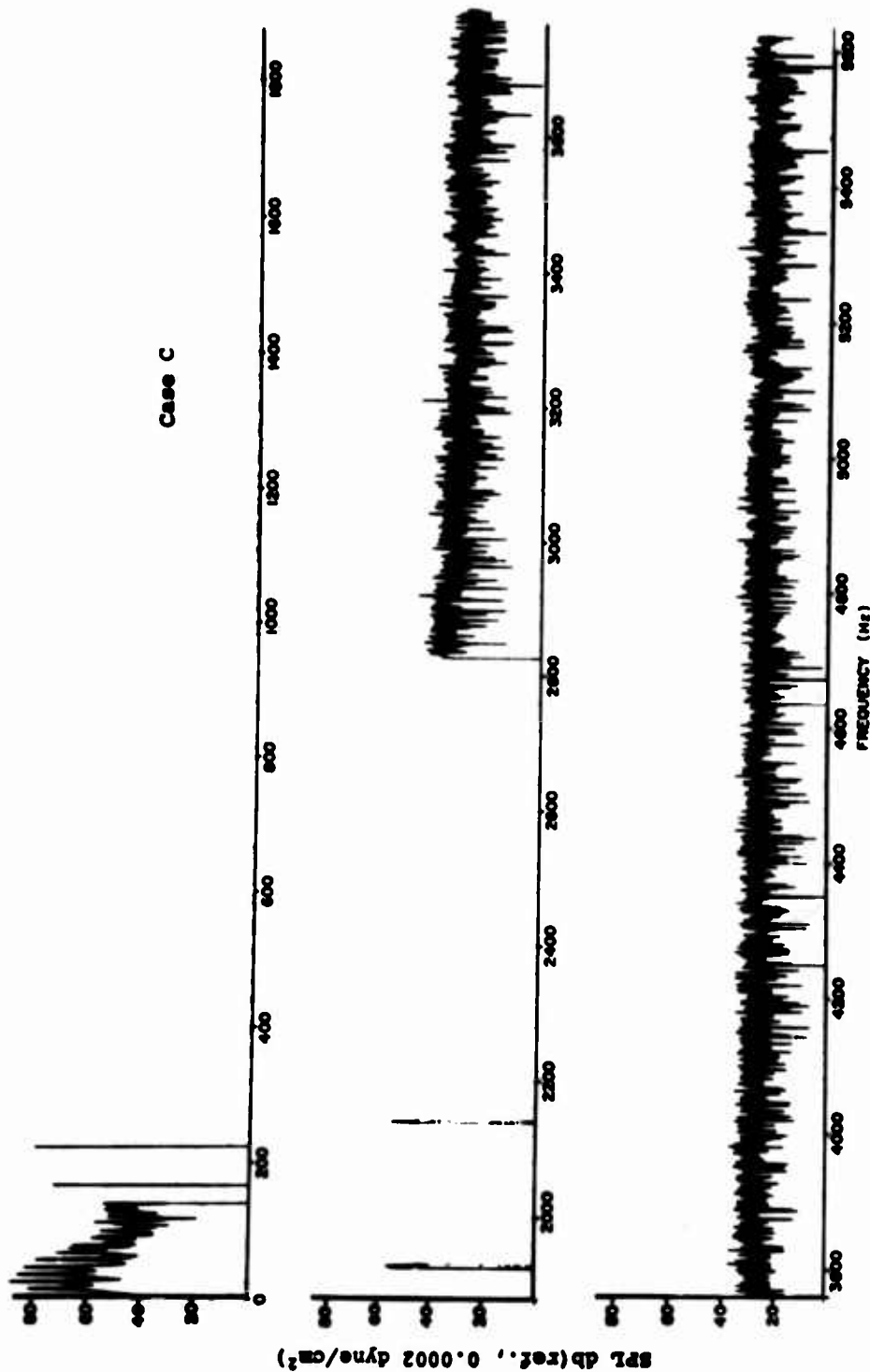


Figure 44. RASA Electronically Digitized Noise Spectrum of Rotational, Gear-Clash, and High Frequency Broadband Noise at Position 4 for UH-1B in Hover.

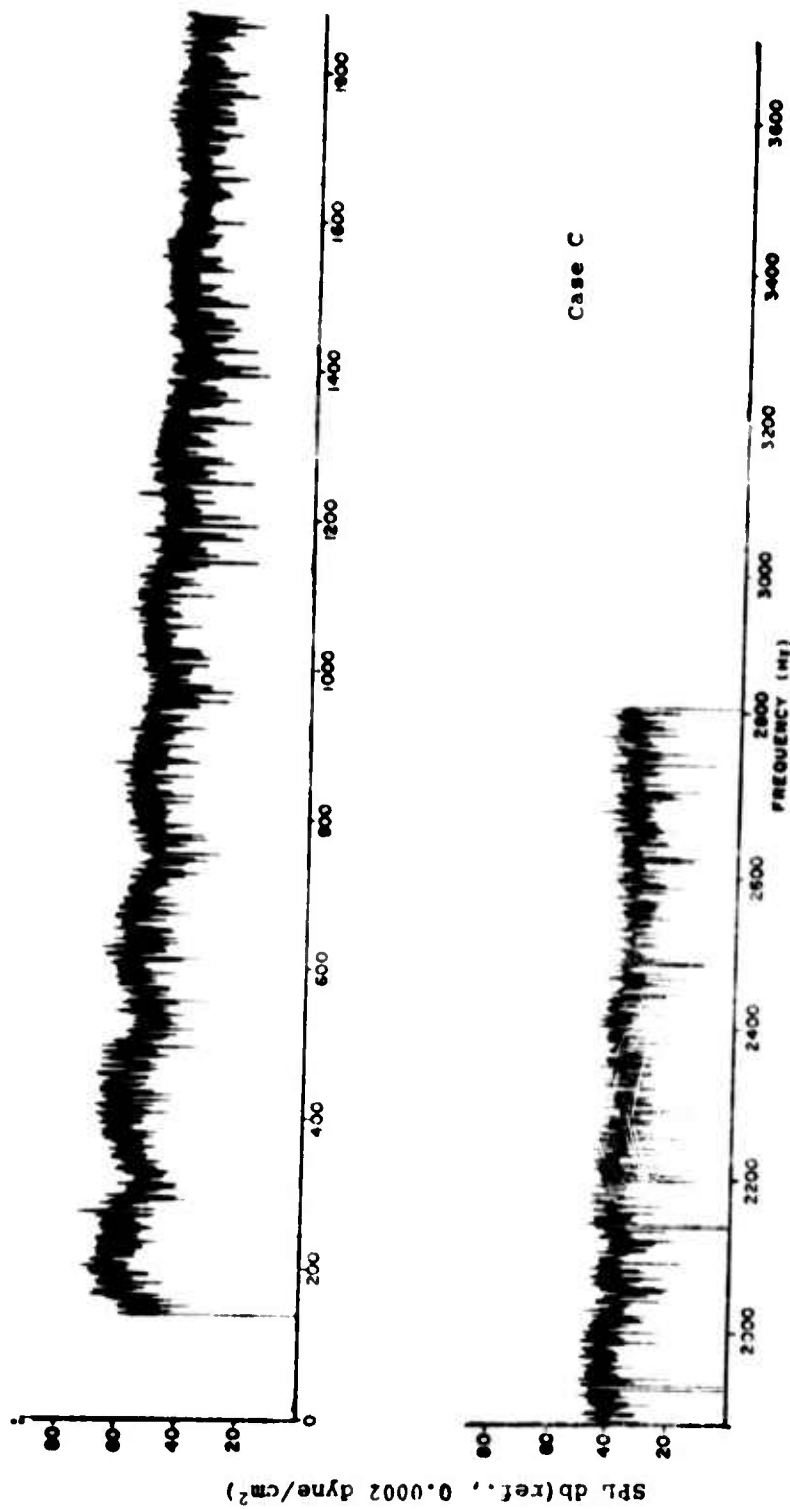


Figure 45. RASA Electronically Digitized Noise Spectrum of "vortex" Noise at Position 4 for UH-1B in Hover.

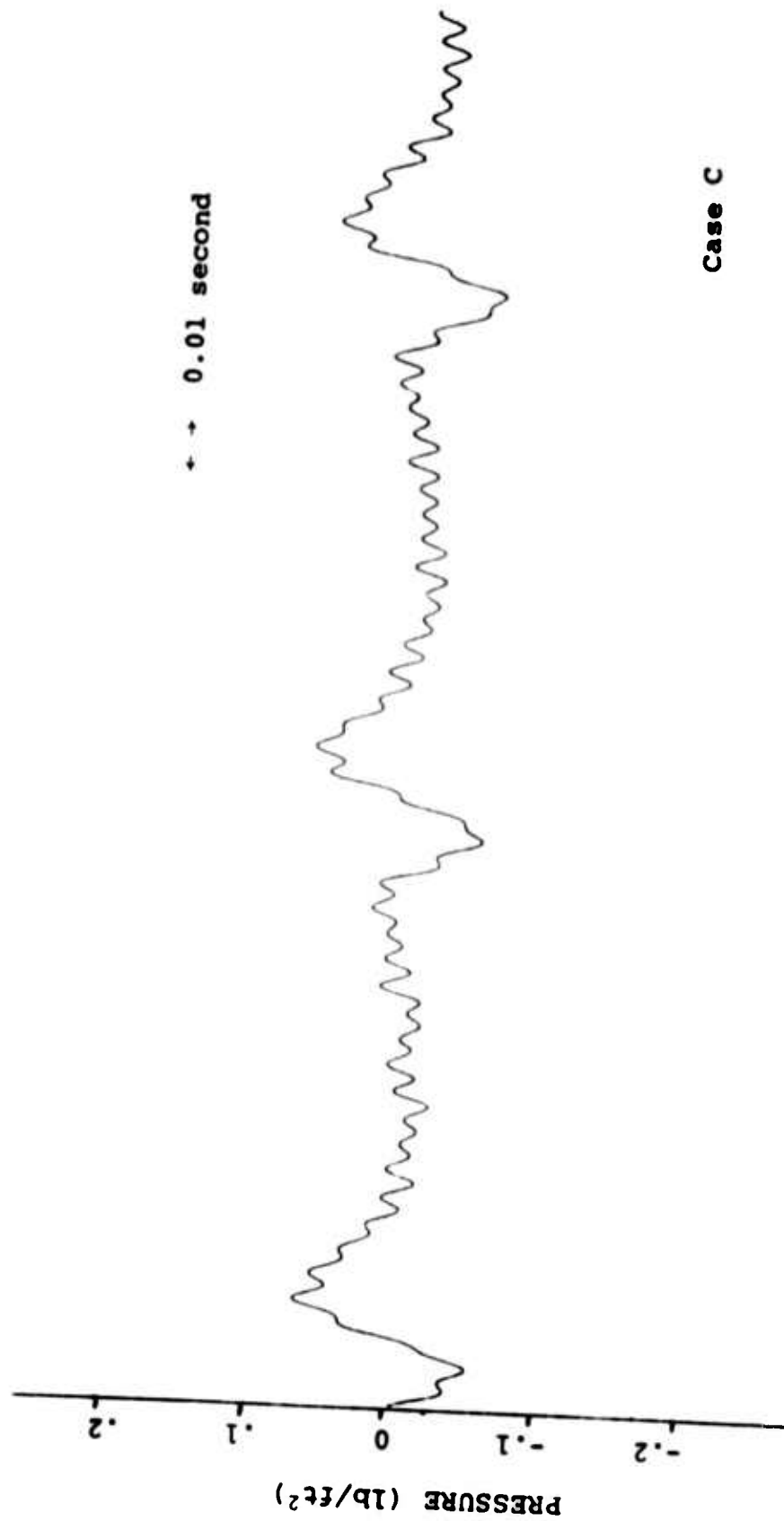


Figure 46. RASA Electronically Digitized Pressure-Time History of Rotational and Discrete Noise at Position 4 for UH-1B in Hover.

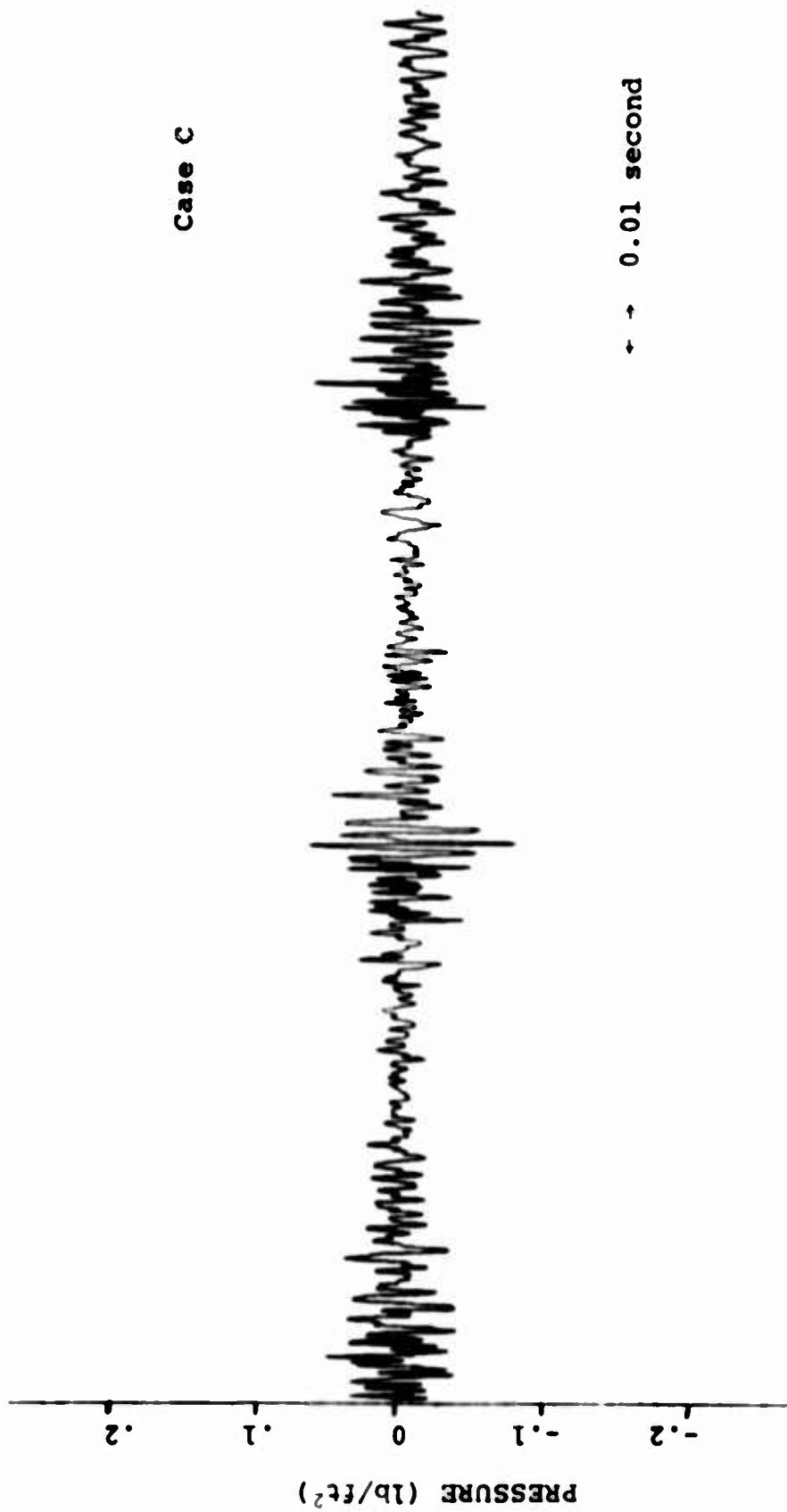


Figure 47. RASA Electronically Digitized Pressure-Time History of Vortex Noise at Position 4 for UH-1B in Hover.

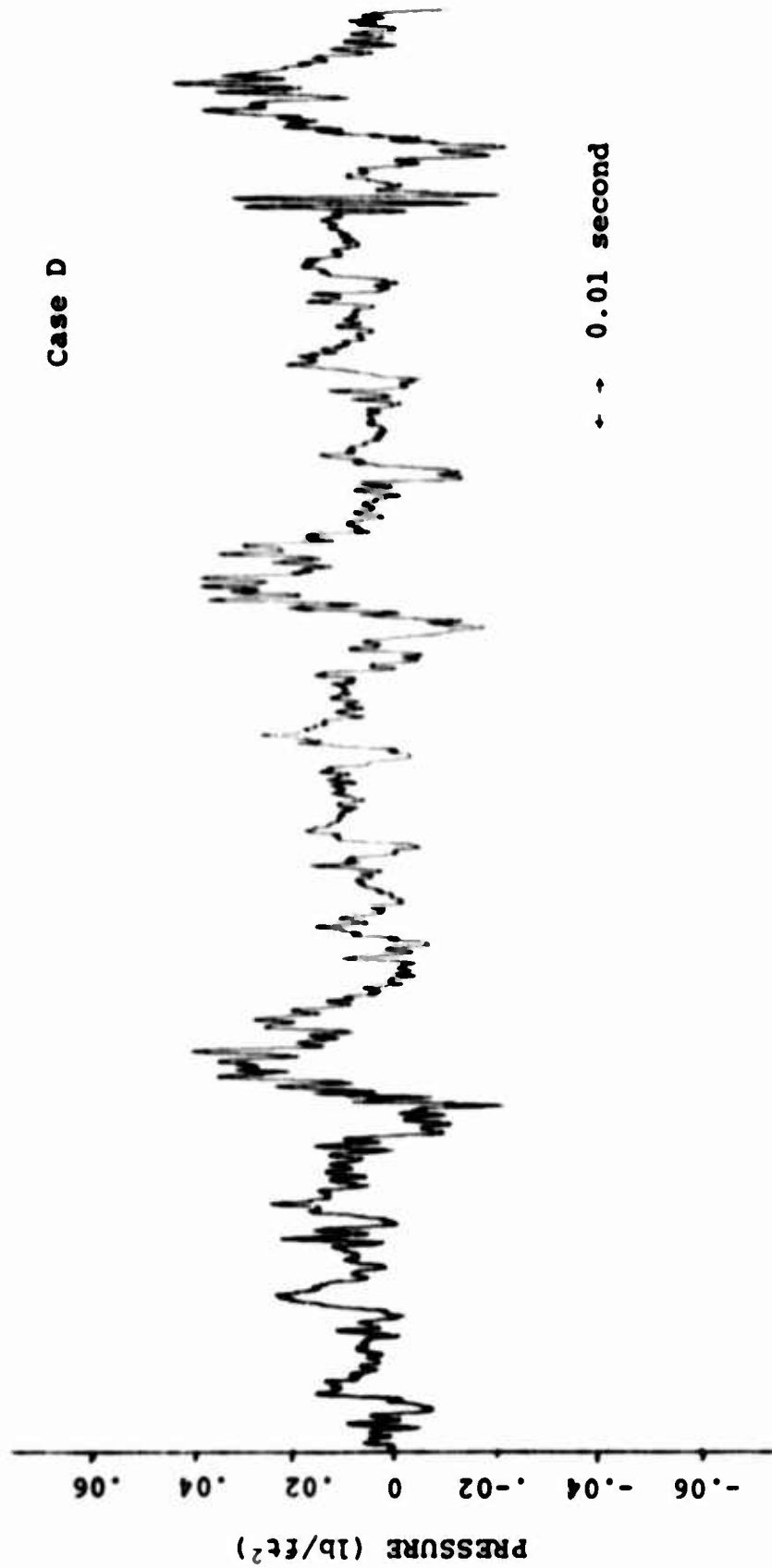


Figure 48. RASA Electronically Digitized Pressure-Time History of Total Recorded Signal at Position 6 for UH-1B in Hover.

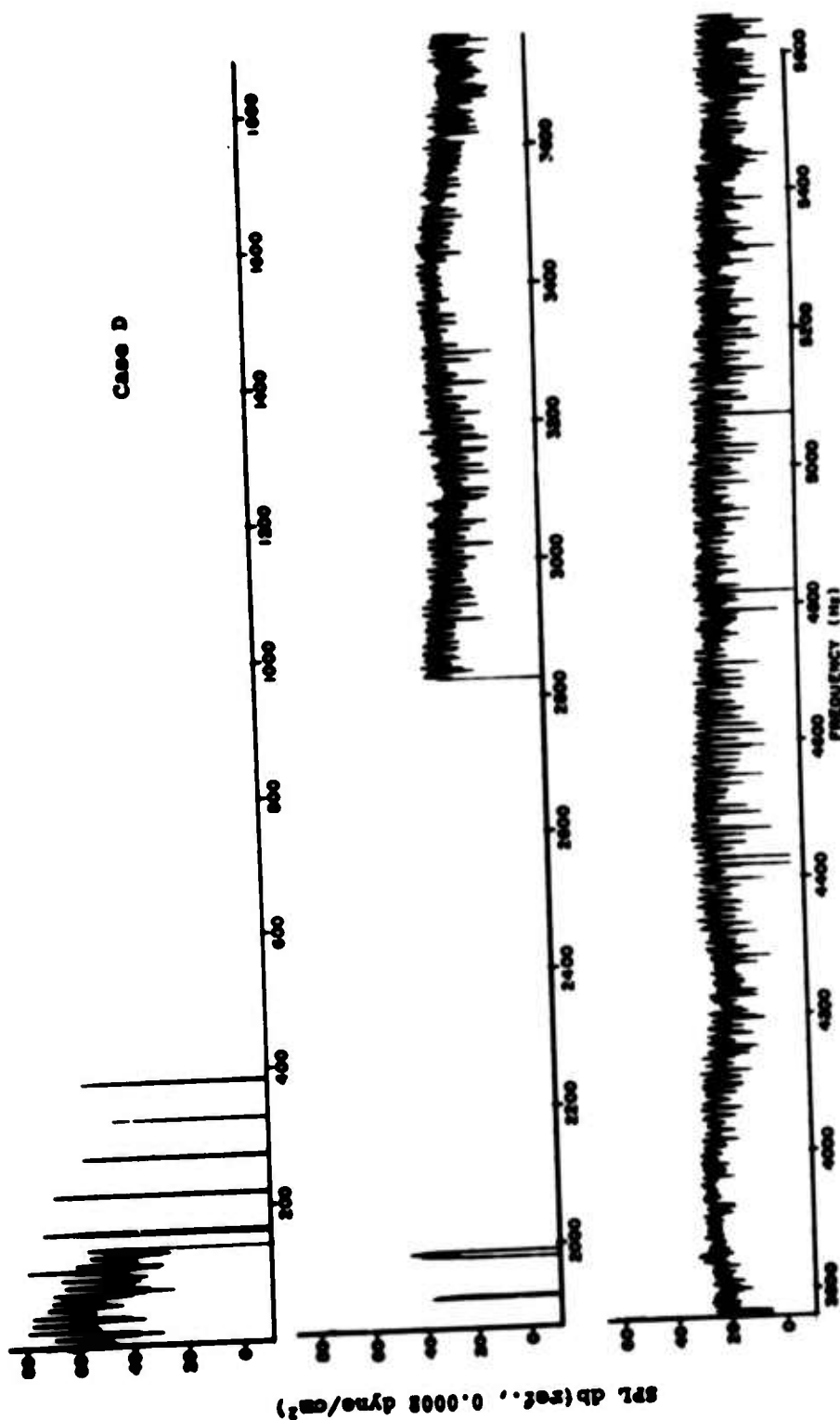


Figure 49. RASA Electronically Digitized Noise Spectrum of Rotational, Gear-Clash, and High Frequency Broadband Noise at Position 6 for UH-1B in Hover.

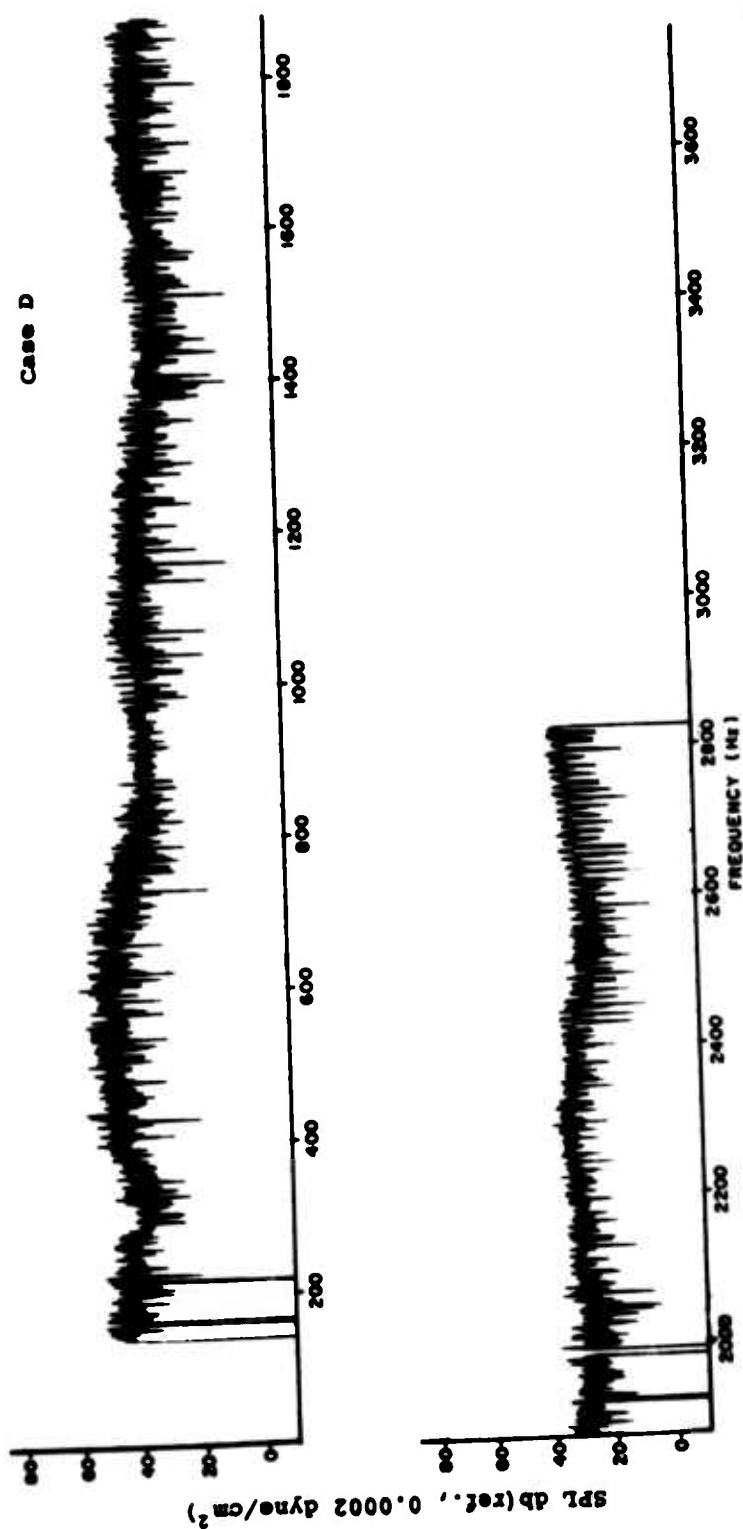


Figure 50. RASA Electronically Digitized Noise Spectrum of "Vortex" Noise at Position 6 for UH-1B in Hover.

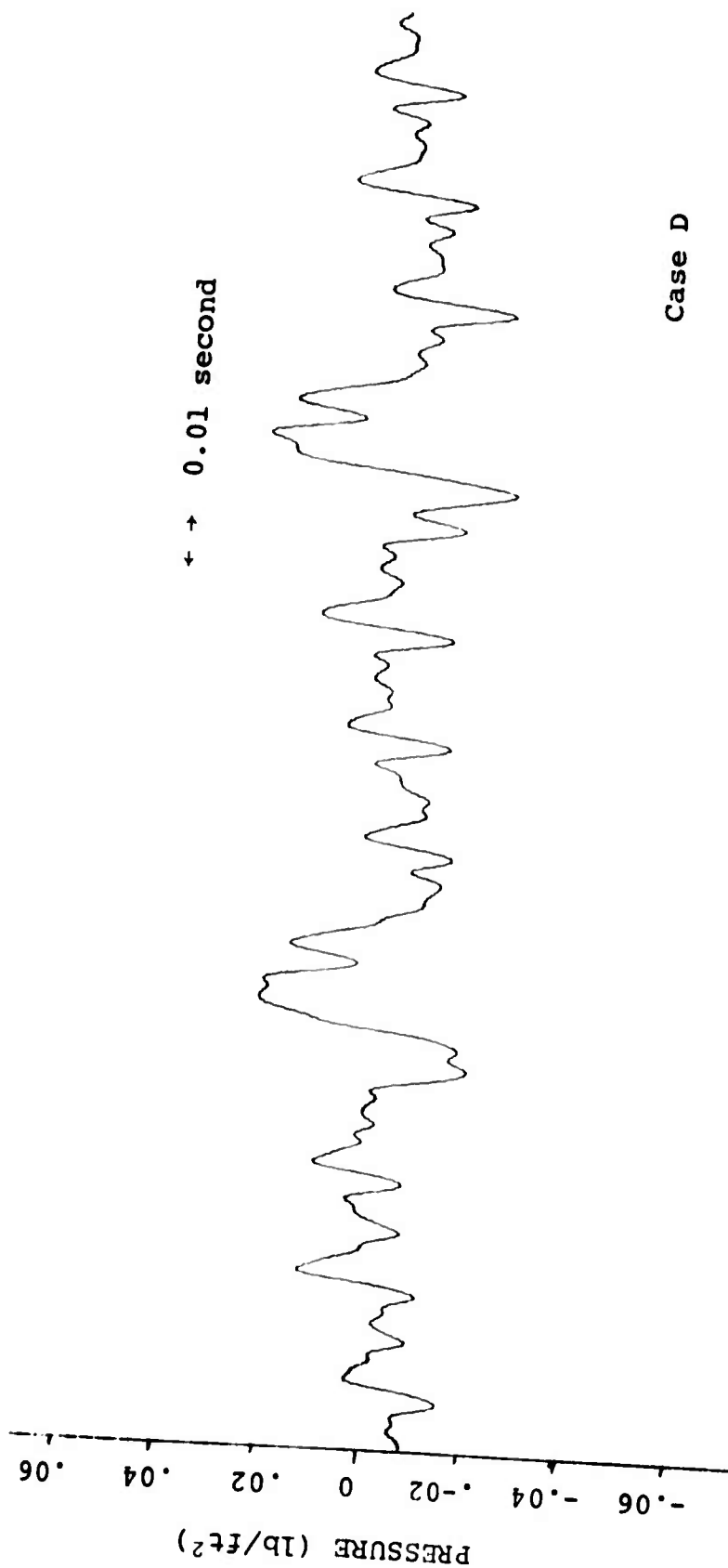


Figure 51. RASA Electronically Digitized Pressure-Time History of Rotational and Gear-Clash Noise at Position 6 for UH-1B in Hover.

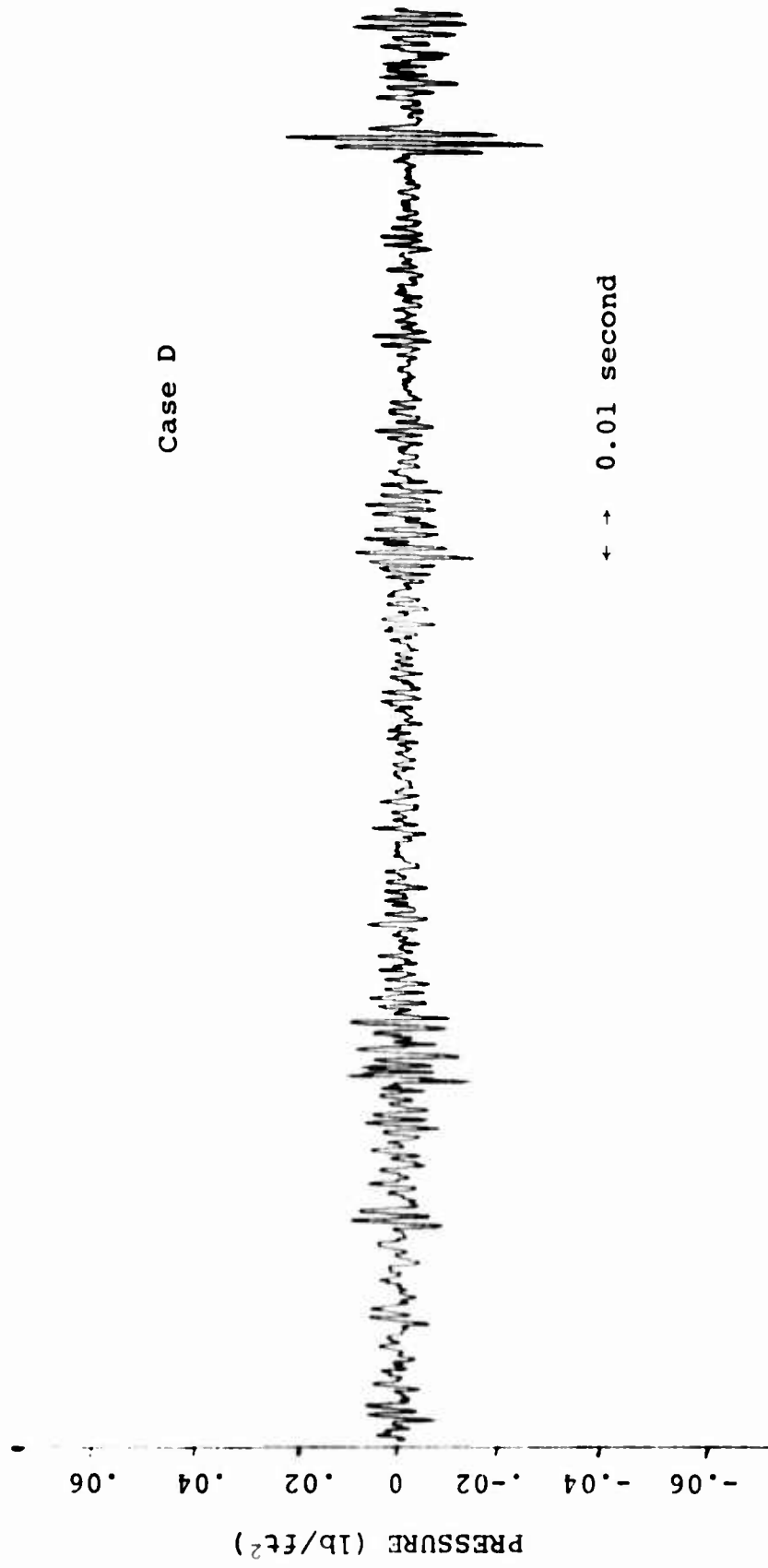


Figure 52. RASA Electronically Digitized Pressure-Time History of "Vortex" Noise at Position 6 for UH-1B in Hover.

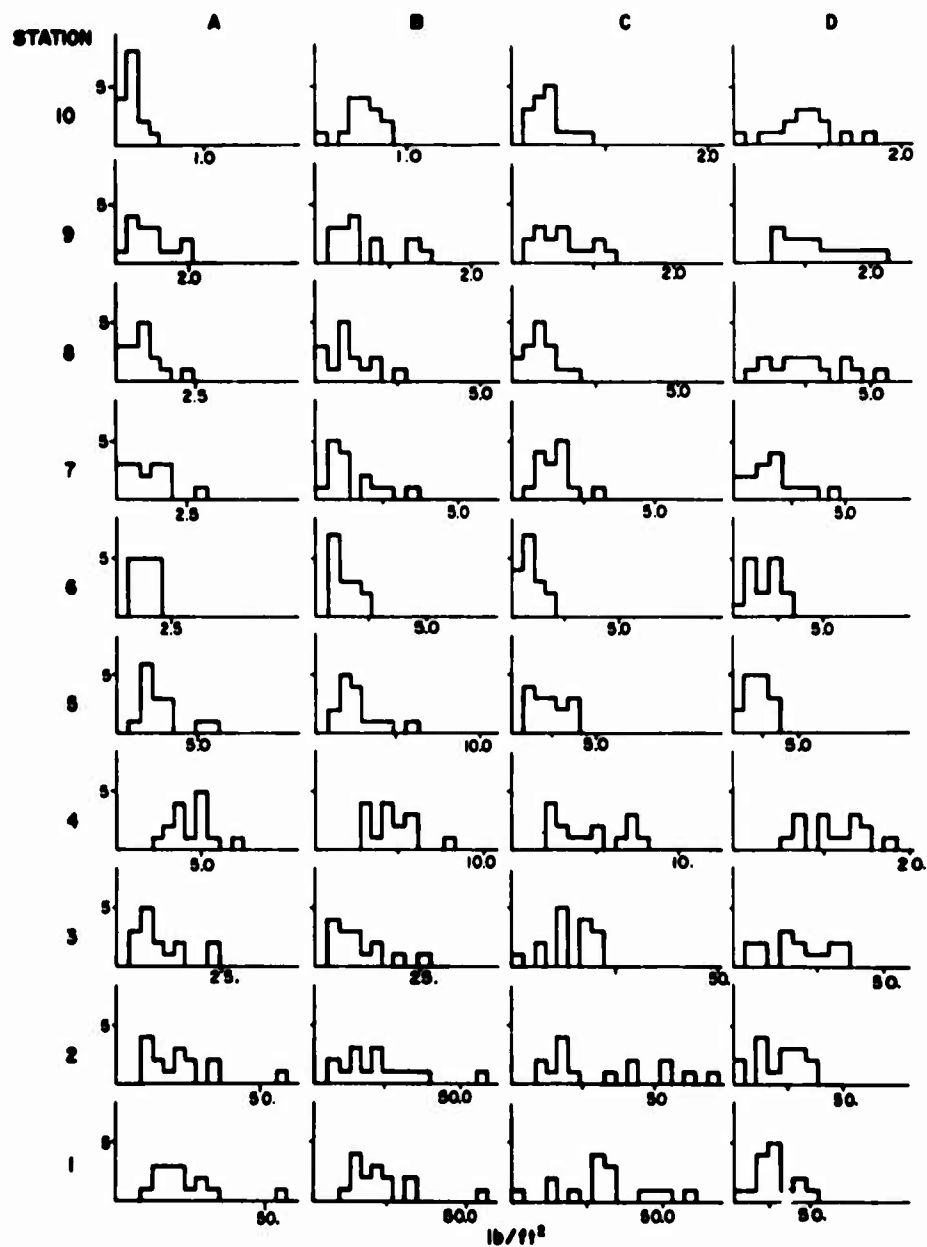


Figure 53. Distribution of the Magnitude of Oscillatory Lift Over Ten Radial Stations for Four Cases.

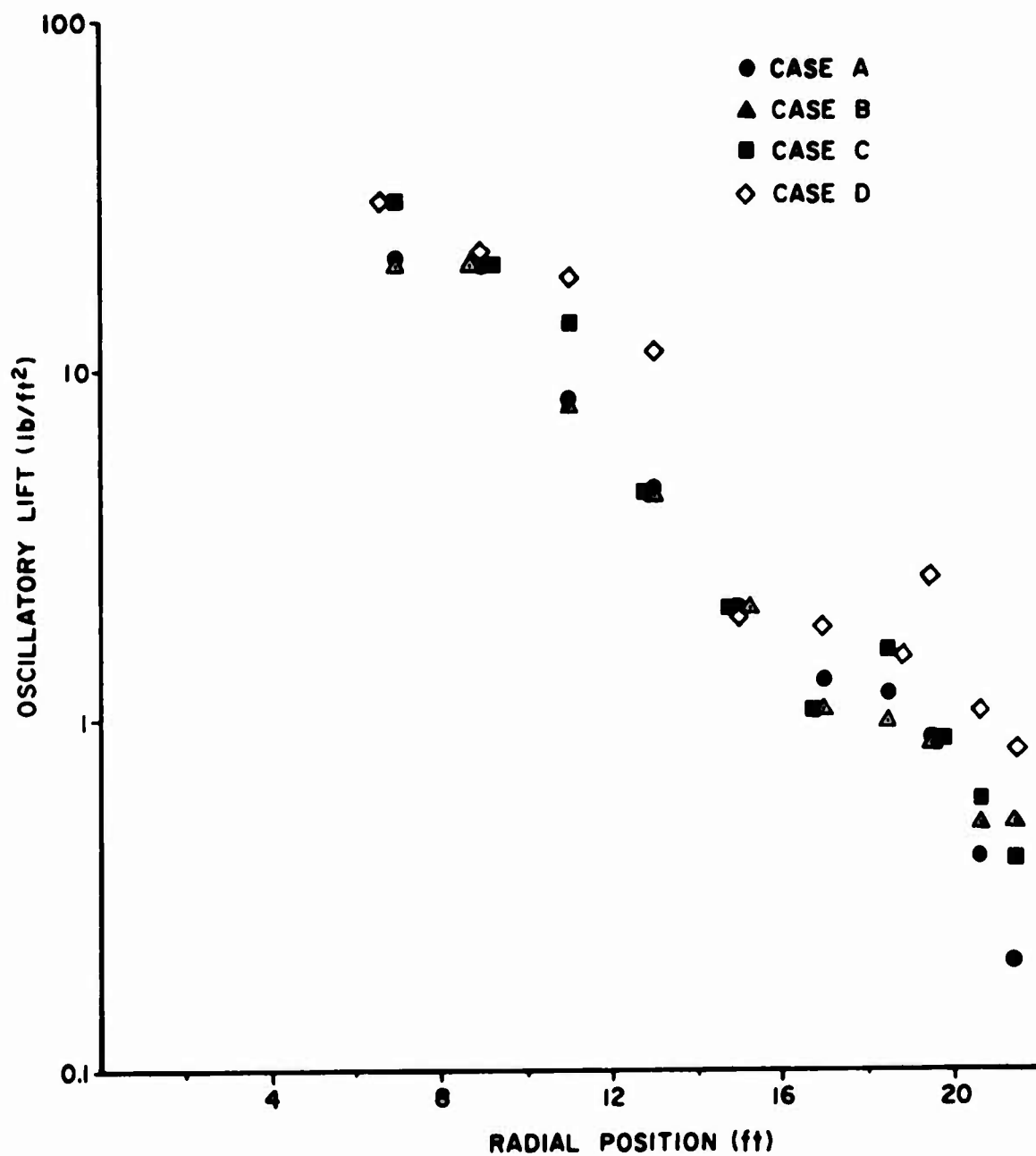


Figure 54. Magnitudes of the Oscillatory Lift Forces as a Function of Radial Position for Each of the Four Cases.

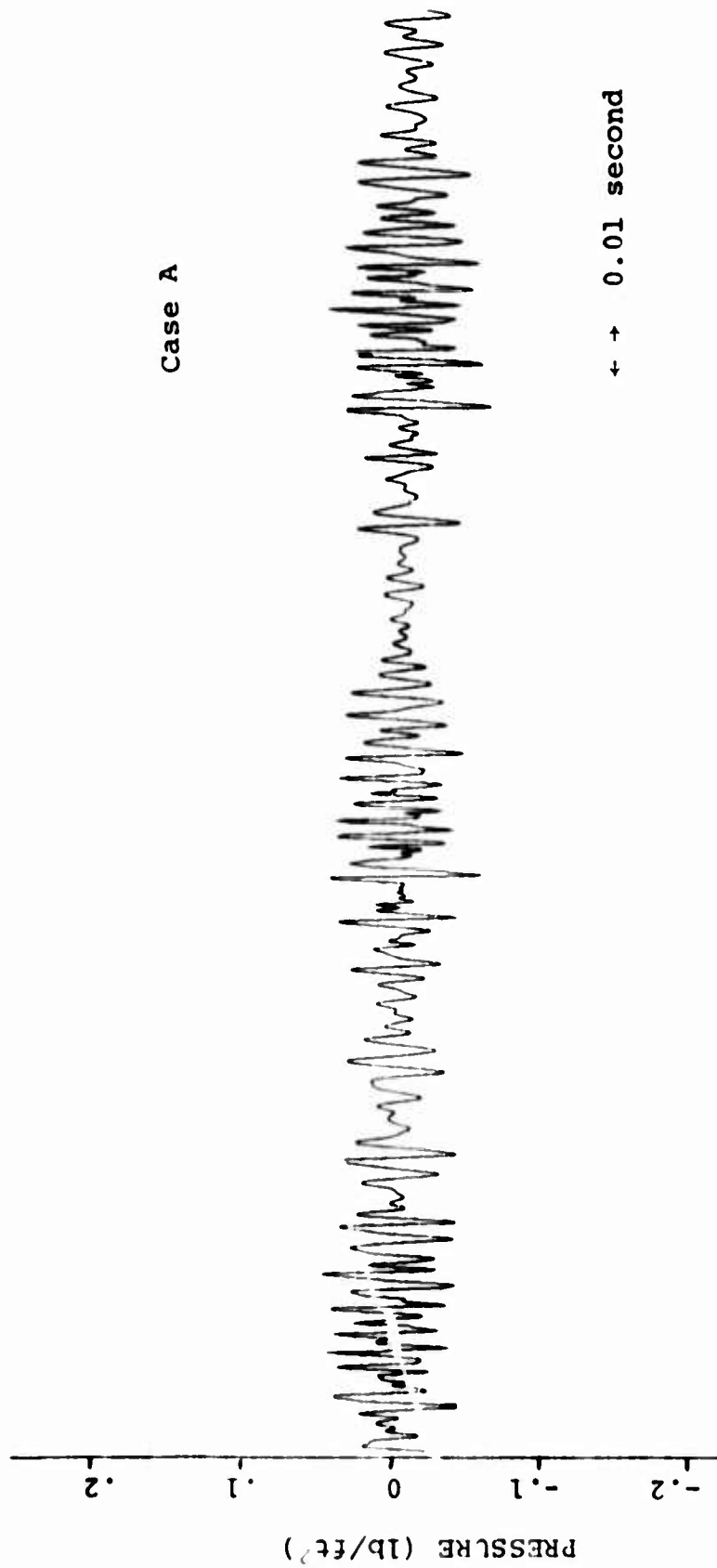


Figure 55. Predicted Vortex Pressure-Time History at Position 4 for UH-1B in Hover.

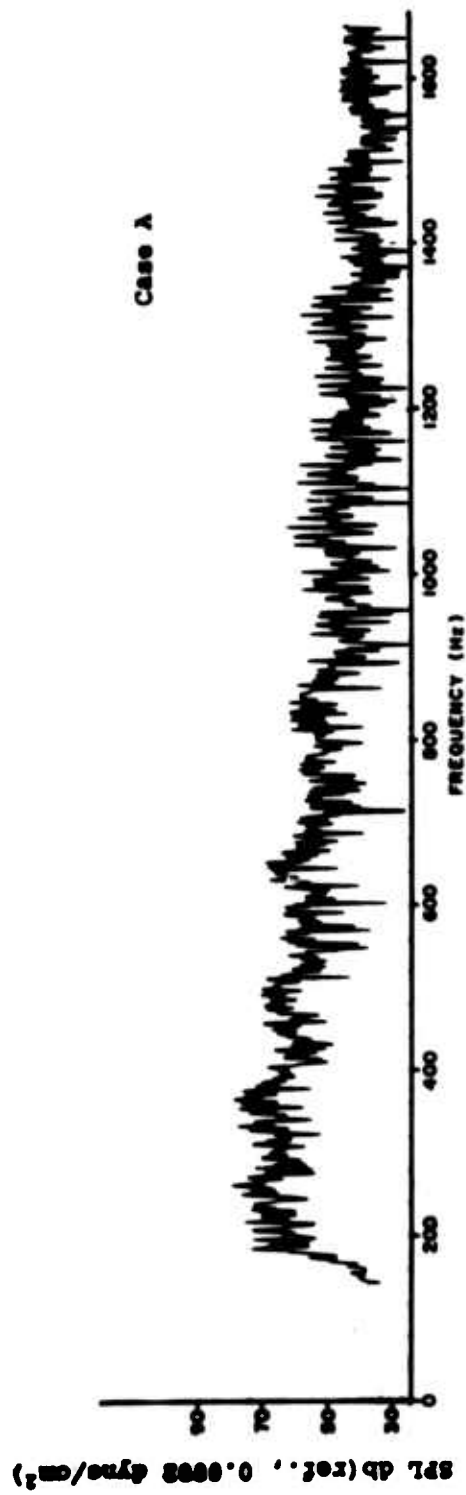


Figure 56. Noise Spectrum of Predicted Vortex Pressure-Time History at Position 4 for UH-1B in Hover.

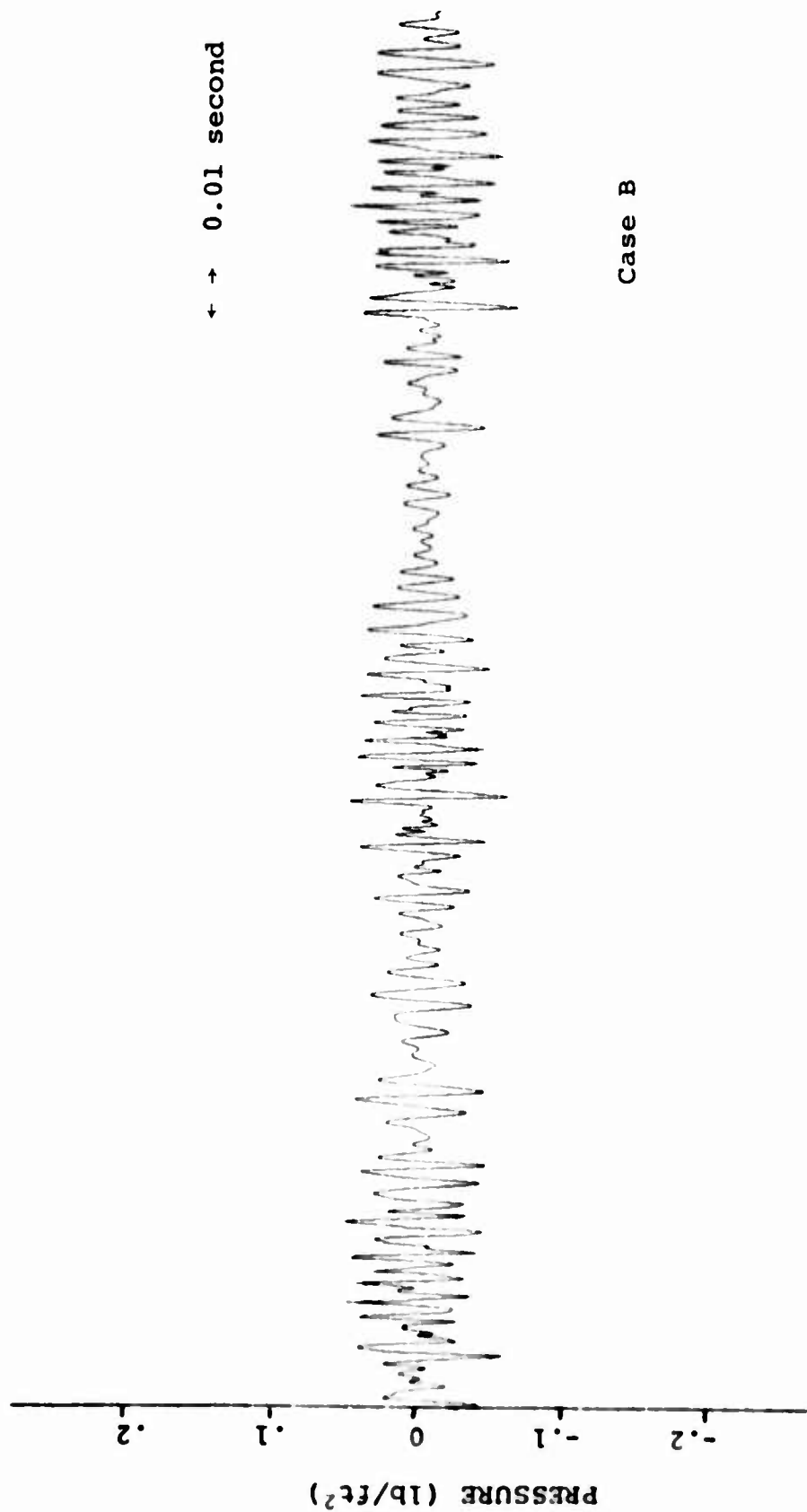


Figure 57. Predicted Vortex Pressure-Time History at Position 4 for UH-1B in Hover.

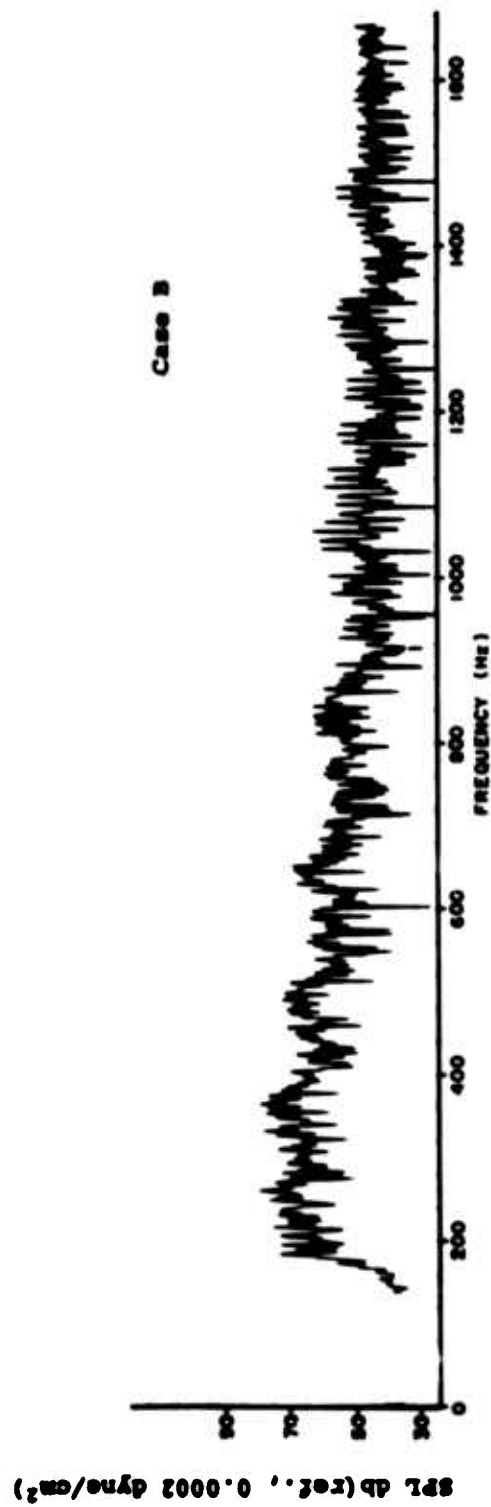


Figure 58. Noise Spectrum of Predicted Vortex Pressure-Time History at Position 4 for UH-1B in Hover.

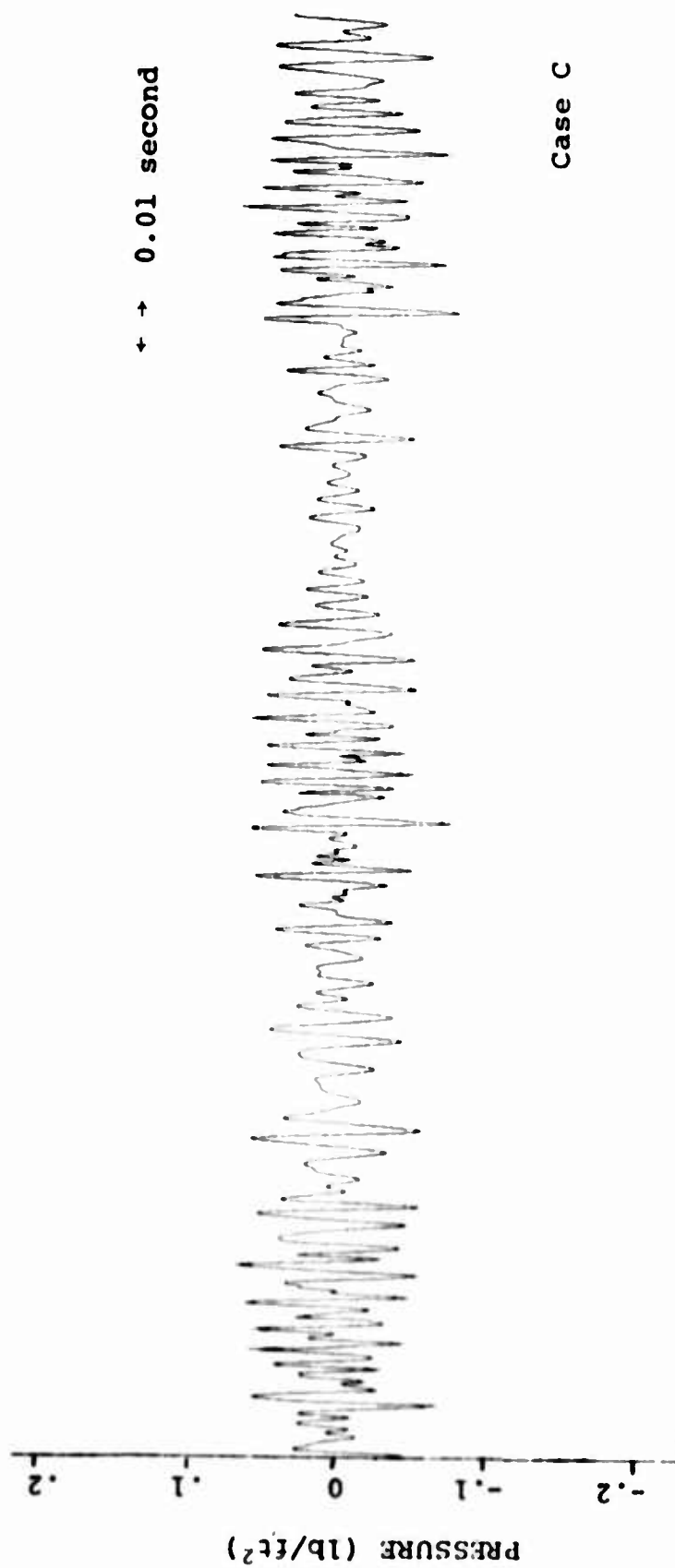


Figure 59. Predicted Vortex Pressure-Time History at Position 4 for UH-1B in Hover.

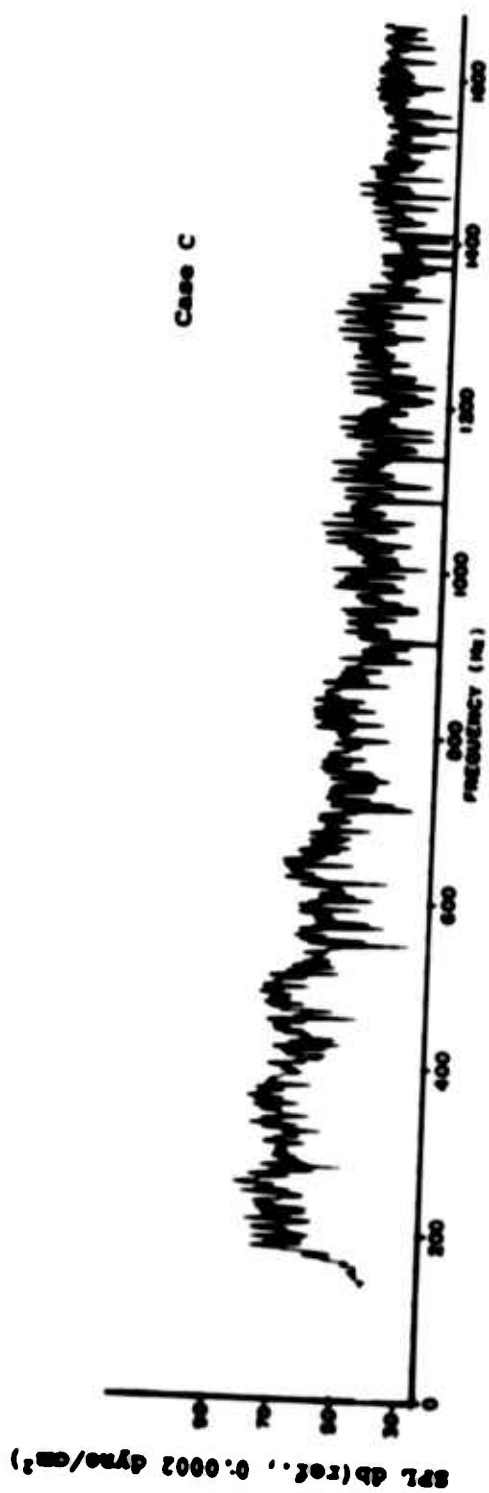


Figure 60. Noise Spectrum of Predicted Vortex Pressure-Time History at Position 4 for UH-1B in Hover.

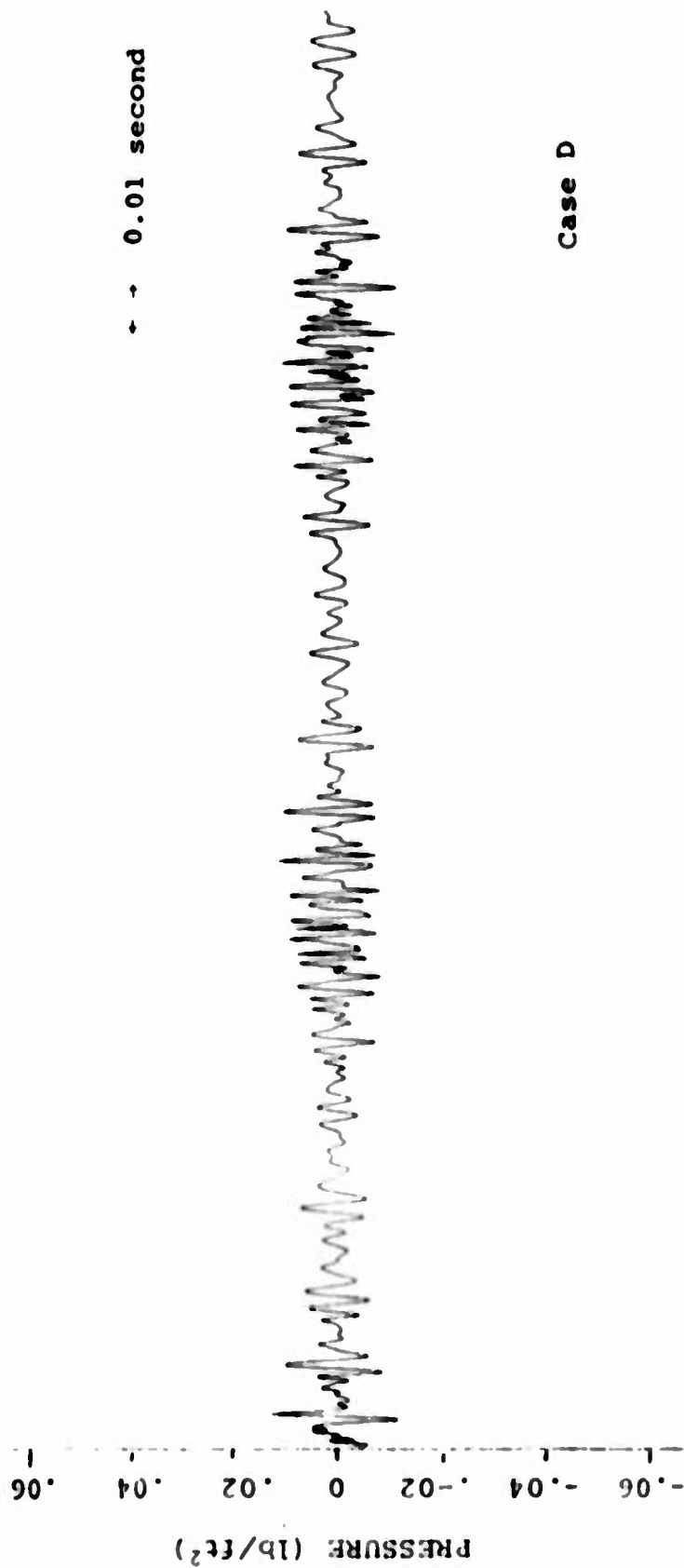


Figure 61. Predicted Vortex Pressure-Time History at Position 6 for UH-1B in Hover.

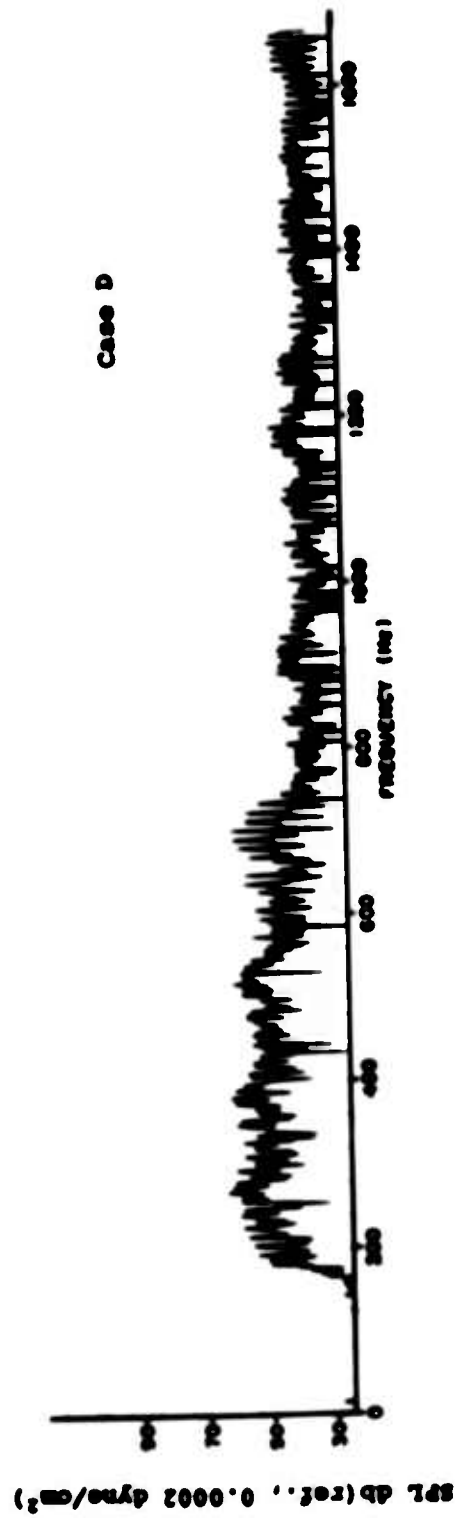


Figure 62. Noise Spectrum of Predicted Vortex Pressure-Time History  
at Position 6 for UH-1B in Hover.

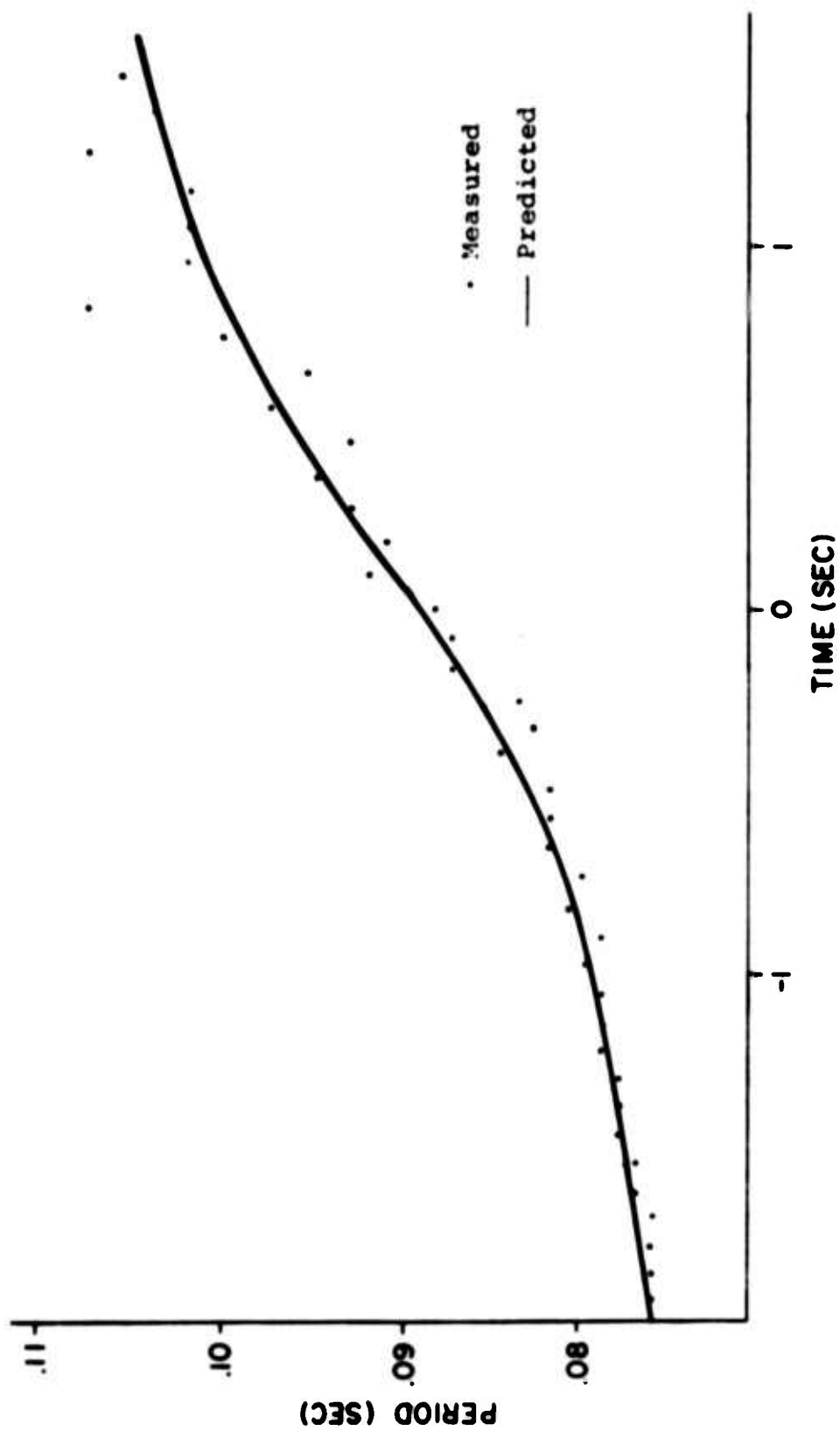


Figure 63. Period of Rotational Noise as a Function of Time at 115 Knots.

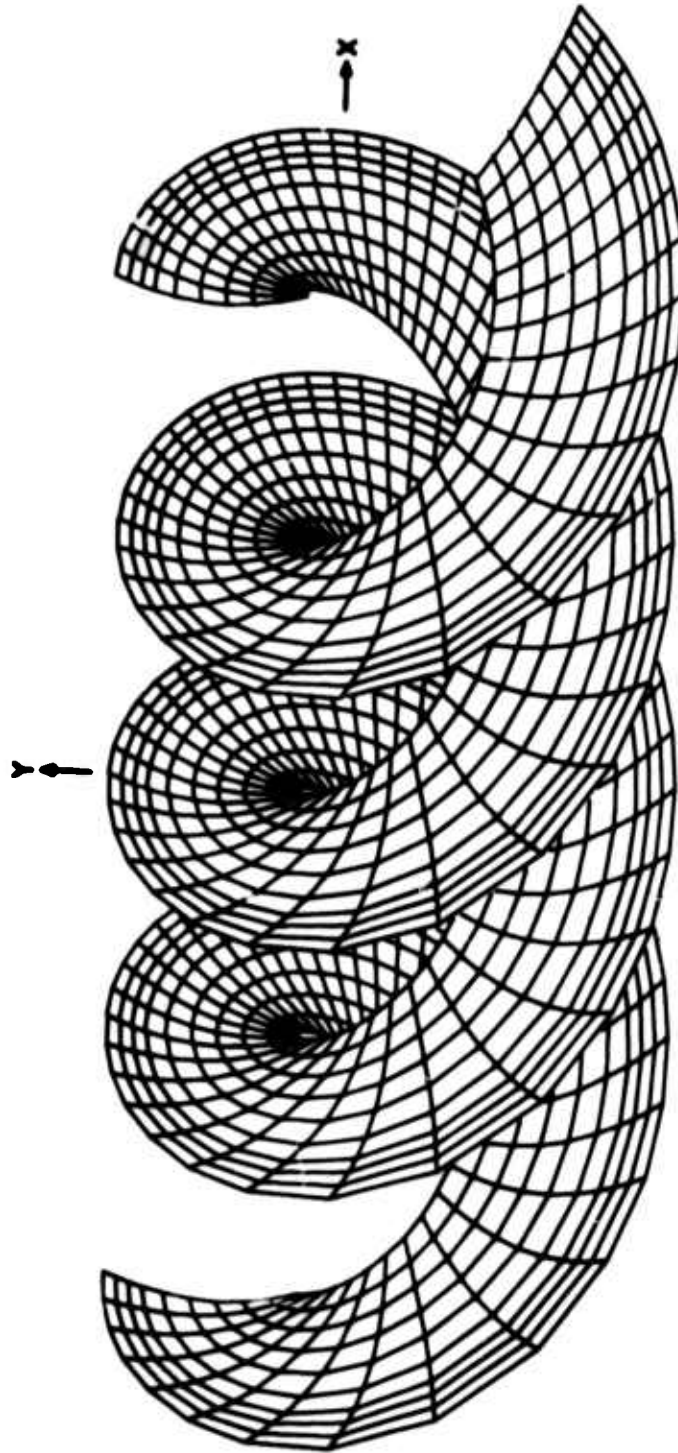


Figure 64. Retarded-Time Diagram of UH-1B at 115 Knots (Observer 200 ft to the Right of the Helicopter).

#### LITERATURE CITED

1. Loewy, R.G., Sutton, L.R., A THEORY FOR PREDICTING THE ROTATIONAL NOISE OF LIFTING ROTORS IN FORWARD FLIGHT, INCLUDING A COMPARISON WITH EXPERIMENT, USAAVLABS Technical Report 65-82, U. S. Army Aviation Materiel Laboratories, Fort Eustis, Virginia, January 1966, AD 629377.
2. Loewy, R.G., Sadler, S.G., A THEORY FOR PREDICTING THE ROTATIONAL AND VORTEX NOISE OF LIFTING ROTORS IN HOVER AND FORWARD FLIGHT, NASA CR-1333, May 1969.
3. Schlegel, R., King, R., Mull, H., HELICOPTER ROTOR NOISE GENERATION AND PROPAGATION, USAAVLABS Technical Report 66-4, U. S. Army Aviation Materiel Laboratories, Fort Eustis, Virginia, October 1966, AD 645884.
4. Lowson, M.V., THE SOUND FIELD FOR SINGULARITIES IN MOTION, Proceedings of the Royal Society, A, Vol. 286, pp. 559-572, 1965.
5. Lowson, M.V., Ollerhead, J.B., STUDIES OF HELICOPTER ROTOR NOISE, USAAVLABS Technical Report 68-60, U. S. Army Aviation Materiel Laboratories, Fort Eustis, Virginia, January 1969, AD 684394.
6. Stowell, E.Z., Deming, A.F., VORTEX NOISE FROM ROTATING CYLINDRICAL RODS, NACA TN 519, 1935.
7. Yudin, E.Y., ON THE VORTEX SOUNDS FROM ROTATING RODS, NACA TN 1136, 1947.
8. Blokhintsev, D., ACOUSTICS OF A NONHOMOGENEOUS MOVING MEDIUM, NACA TN 1399, 1959.
9. Hubbard, H.H., PROPELLER-NOISE CHARTS FOR TRANSPORT AIRPLANES, NACA TN 2968, 1953.
10. Krzywoblocki, M.Z., INVESTIGATION OF THE WING-WAKE FREQUENCY WITH APPLICATION OF THE STROUHAL NUMBER, J. Aeron. Sci., Vol. 12, No. 1, Jan. 1945, pp. 51-62.
11. Roshko, A., EXPERIMENTS ON THE FLOW PAST A CIRCULAR CYLINDER AT VERY HIGH REYNOLDS NUMBER, J. Fluid Mech., Vol. 10, Part 3, May 1961.
12. Evans, T.D., Nettles, W.E., FLIGHT TEST NOISE MEASUREMENTS OF A UH-1B HELICOPTER, paper presented at the AHS/UTA Joint Symposium on Environmental Effects on VTOL Designs at Arlington, Texas, November 1970.

13. Roshko, A, ON THE DRAG AND SHEDDING FREQUENCIES OF TWO-DIMENSIONAL BLUFF BODIES, NACA TN 3169, 1954.
14. von Doenhoff, A.E., Tetervin, N., DETERMINATION OF GENERAL RELATIONS FOR THE BEHAVIOR OF TURBULENT BOUNDARY LAYERS, NACA Rept. 772, 1943.
15. Gessow, A., Myers, G.C., Jr., AERODYNAMICS OF THE HELICOPTER, The MacMillan Company, New York, 1952.
16. Lighthill, M.J., SOUND GENERATED AERODYNAMICALLY, Royal Aircraft Establishment (Farnborough) Technical Memorandum No.: Dir. 8, November, 1961, AD 275075.
17. Sadler, S.G., A METHOD FOR PREDICTING HELICOPTER WAKE GEOMETRY, WAKE-INDUCED FLOW AND WAKE EFFECTS ON BLADE AIRLOADS, Paper presented at the 27th Annual National V/STOL Forum of the AHS, Washington, D.C., May 1971.
18. Cox, C.R., Lynn, R.R., A STUDY OF THE ORIGIN AND MEANS OF REDUCING HELICOPTER NOISE, TCREC Technical Report 62-73, U. S. Army Transportation and Research Command, Fort Eustis, Virginia, November 1962.